DISS. ETH NO. <u>20611</u>

SUBCRITICAL CRACK GROWTH IN HARDENED CEMENT PASTE

A dissertation submitted to

ETH ZURICH

for the degree of

Doctor of Sciences

presented by

WEI CAI

Master of Science, Tampere University of Technology

born 20.10.1982

citizen of China

accepted on the recommendation of

Prof. Dr. Robert J. Flatt   examiner
Prof. Dr. Eugen Brühwiler   co-examiner
Dr. Jan Bisschop   co-examiner

2012

ABSTRACT

Subcritical crack growth (SCG) is an environmentally-assisted slow cracking phenomenon that occurs in (quasi-)brittle materials under static load. Subcritical cracks grow at stress levels much lower than the one required for fast dynamical cracking. This type of cracking is facilitated by some time-dependent effect at the crack tip that weakens the material. SCG can be characterized by the relationship between the stress intensity factor at crack tip and the subcritical crack velocity. The double-torsion (DT) test is commonly used to extract these as well as other SCG parameters from the measured force relaxation of DT-specimens. Understanding SCG is essential for making reliable predictions of the durability of concrete under sustained load.

In this thesis, a novel method has been developed to optically measure SCG in hardened cement paste (with w/c-ratio of 0.3, 0.4, 0.5, 0.6 and 0.7) by carrying out DT tests inside an Environmental Scanning Electron Microscope or under an optical microscope. Crack tip detection is facilitated by digital image correlation on the time-lapse microscope images. DT-tests at 10% relative humidity (RH) in hardened cement paste showed that optically measured crack velocities were much lower than those calculated from the DT-specimen relaxation. In many experiments the SCG rapidly stopped, due to a lack of moisture in the environment and due to discontinuities in the cementitious matrix. At 90% RH, the force-relaxation in the DT-test was much higher than at 10% relative humidity due to the higher moisture content in the environment. Also at these conditions it was found that only part of the measured relaxation was due to actual crack growth.

The observed discrepancies between the optically measured and calculated velocities at 10 and 90% RH are attributed to creep. Therefore the influence of creep on SCG in hardened cement paste (with w/c-ratio of 0.3, 0.5, 0.6 and 0.7) was investigated. Tests at 10% RH showed that the measured relaxation from DT tests was mainly due to creep. Tests at 90% RH showed that creep and subcritical crack growth both contributed to the measured relaxation. The creep-induced relaxation was separated empirically from the measured relaxation to approximate the SCG-induced relaxation. Subcritical crack indices (i.e. susceptibility to SCG) were obtained based on this approximation, and were found to be higher than those calculated from the measured relaxation and generally consistent with the results from optical measurements. The subcritical crack indices were used as bases for life-time analyses in this study.

Moreover, self-healing of subcritical cracks in hardened cement paste (with w/c-ratio of 0.3 and 0.7) was examined, because it can potentially counteract long-term subcritical cracking. The subcritical cracks can undergo healing through precipitates from the environment or products from continued hydration reactions. For the (partially-)healed materials, the resistance against SCG can be recovered to a certain degree, depending on the specimen properties (i.e. w/c-ratio, degree of hydration) and healing time.

ZUSAMMENFASSUNG

Das subkritische Risswachstum (SKR) ist ein umgebungsbedingtes langsames Rissphänomen, welches in quasi-spröden Materialien unter statischer Last auftritt. Subkritische Risse breiten sich im Gegensatz zur schnellen dynamischen Rissbildung unter viel geringeren Spannungen aus. Dieser Risstyp wird durch einen zeitabhängigen Effekt an der Rissspitze gefördert, welcher das Material schwächt. Die SKR kann durch die Beziehung zwischen dem Spannungsintensitätsfaktor an der Rissspitze und der subkritischen Rissgeschwindigkeit charakterisiert werden. Im Allgemeinen wird der 'Doppel-Torsionstest (DT)-Tests' angewendet, um sowohl diesen als auch andere SKR-Parameter der Kraftrelaxationsmessung von DT-Proben zu bestimmen. Das Verständnis der SKR ist essenziell, um zuverlässige Vorhersagen für die Dauerhaftigkeit von Beton unter Langzeitbelastung treffen zu können.

In dieser Doktorarbeit wurde eine neue Methode entwickelt, die es erlaubt, das SKR an Zementstein (mit einem W/Z-Wert von 0.3, 0.4, 0.5, 0.6 und 0.7) mit Hilfe eines DT-Tests in einem ESEM (Environmental Scanning Electron Mikroscope) oder unter einem Lichtmikroskop visuell zu messen. Die Rissspitzenerkennung erfolgte durch digitale Bildkorrelation anhand von Zeitrafferbildern. Die DT-Tests an Zementstein zeigten bei 10% relativer Feuchte (RF), dass die optisch gemessenen Rissgeschwindigkeiten viel geringer waren als jene, welche aus der Relaxation der DT-Probe berechnet wurden. Bei vielen Experimenten kam es aufgrund fehlender Feuchte aus der Umgebung und der Diskontinuität der Zementmatrix zu einem schnellen Stoppen der SKR. Unter einer relativen Feuchte von ca. 90% kam es beim DT-Test, bedingt durch den höheren Feuchtegehalt der Umgebung, zu einer viel stärkeren Kraftrelaxation als bei einer

10%iger Feuchte. Auch unter diesen Bedingungen wurde herausgefunden, dass nur ein Teil der gemessenen Relaxation auf dem tatsächlichen Risswachstum beruht.

Die beobachtete Diskrepanz zwischen optisch gemessenen und berechneten Geschwindigkeiten bei 10 und 90% RF sind auf Kriechvorgänge zurückzuführen. Deshalb wurde der Einfluss des Kriechens in Zementstein (mit einem W/Z-Wert von 0.3, 0.5, 0.6 und 0.7) untersucht. Experimente bei 10% RF zeigten, dass die während des DT-Tests gemessene Relaxation hauptsächlich auf das Kriechen zurückzuführen war. Experimente bei 90% RF zeigten, dass sowohl das Kriechen als auch das subkritische Risswachstum gemeinsam zur gemessenen Relaxation beitrugen. Die durch das Kriechen induzierte Relaxation wurde empirisch von der gemessenen getrennt, um eine Annäherung an die SKR-induzierte Relaxation zu erzielen. Basierend auf dieser Annäherung konnten subkritische Riss-Indizes (d.h. Anfälligkeit für SKR) gewonnen werden. Diese lagen höher als die von den gemessenen Relaxation berechneten und zeigten generell eine gute Übereinstimmung mit den optischen Messungen. Die subkritischen Riss-Indizes wurden als Grundlage für die Lebensdaueranalysen in der vorliegenden Arbeit verwendet.

Darüber hinaus wurde der Selbstheilungseffekt subkritischer Risse in Zementstein (mit einem W/Z-Wert von 0.3 und 0.7) untersucht, da dieser langfristig dem subkritischen Risswachstum potentiell entgegenwirken kann. Die Risse können aufgrund von Ablagerungen aus der Umgebung oder Hydratationsreaktionen eine sog. Heilung erfahren. Solche (teilweise) geheilten Materialien können ihre Widerstandsfähigkeit gegenüber dem SKR bis zu einem bestimmten Grad zurückgewinnen, was von den Probeneigenschaften (W/Z-Wert, Hydratationsgrad) und der Heilungsdauer abhängig ist.

ACKNOWLEDGMENTS

I would like to express my special appreciation to Dr. Jan Bisschop. He has offered me tremendous assistance during my research: encouraged my research and guided me to grow as an independent researcher. I appreciate all his contributions of time and brilliant ideas to make my Ph.D. experience productive and meaningful. The wisdom, joy and enthusiasm he has for his research was contagious and motivational, even during tough times in my Ph.D. journey.

Especially, I would like to thank Prof. Dr. Robert J. Flatt for serving as my official supervisor. It has been a great honor to be one of his first Ph.D. students. I also want to thank him for supporting me to complete my Ph.D. study successfully, and for his brilliant ideas, suggestions and generous guidance. Without these, it would not be possible for me to finish the long journey. I am also very thankful for the excellent example he has set as a successful scientist and respectable group leader.

I also would like to thank co-examiner, Prof. Dr. Eugen Brühwiler from EPFL, for his inspiring comments and suggestions that helped make this work more complete.

I am especially grateful to Carsten Rieger, Dominik Meyer and Daniel Caduff for their very thoughtful discussions, comments and suggestions on my experimental methods. Without the mechanical specialty of Mariano Pauli, components of the testing device could not have been produced and assembled. Without the electrical specialty of Ernst

ABBREVIATIONS AND SYMBOLS

AAR	Alkali-aggregate reaction
AOI	Area of interest
BSE	Backscattered electron
CEM	Ordinary portland cement
CH	Calcium hydroxide
COS	Crack opening strain
CR	Creep-induced relaxation
C-S-H	Calcium silicate hydrate
DCB	Double-cantilever beam
DCDC	Double-cleavage drilled-compression
DICM	Digital image correlation method
DT	Double-torsion
ESEM	Environmental scanning electron microscope
HCP	Hardened cement paste
LEFM	Linear elastic fracture mechanics
LVDT	Linear variable displacement transducer
OPC	Ordinary portland cement
RH	Relatively humidity
SCG	Subcritical/slow crack growth
SSD	Solid state detector
W/C	Water-to-cement ratio

a	Crack length
d_t	Total specimen thickness
d_w	Specimen thickness of the cracked part
k'	A constant related to Poisson's ratio
m_w	Weibull modulus
n	Subcritical crack index
t	Time
u	Displacement
v	Crack velocity
w_m	Moment arm for the load
C	Cross-correlation coefficient
E	Young's modulus
G	Strain energy release rate
H	Activation enthalpy
I	Image grey level
K	Stress intensity factor
K_c	Fracture toughness
K_{Ic}	Critical stress intensity factor
K_o	Threshold stress intensity factor
K_Δ	Certain mode of stress intensity factor
L	Specimen length

P	Applied force
Pr	Probability of fracture
Q	Apparent activation energy
R	Gas constant
S	Shear modulus
T	Absolute temperature
U_K	Kinetic energy
V^*	Activation volume
W	Specimen width
Y	Shape constant
(i, j)	Cartesian coordinate system
(r, θ)	Polar coordinate system
α_{cem}	Degree of hydration
ε	Strain
$\sigma_{i,j}$	Stress in Cartesian coordinate system (i, j)
σ_c	Characteristic strength of material
λ	Compliance
ρ	Curvature radius of crack tip
μ	Poisson's ratio
ψ	Correction function
Λ	Strain energy function
Φ	Correction factor

LIST OF TABLES

LIST OF FIGURES

period. (b) shows a crack with large opening with precipitates inside. X and Y denote the coordinates of the image center (for the loading point: X = 0 mm, Y = 0 mm). (e) is the schematic illustration of the relative position of each imaging area in the DT specimen along the old subcritical crack. The images were taken during or immediately after DT tests and the specimens were not subjected to any subsequent treatment (e.g. grinding or polishing). 111

TABLE OF CONTENTS

CHAPTER 1 General Introduction

1.1. Background

Concrete is the most widely used building material in the world. It basically consists of aggregates (i.e., gravel or crushed rock, and sand) bound together by hardened cement paste. Cement paste is a mixture of cement and water, and hardens due to the reaction of water with cement that produces hydration products that function as the 'glue' in concrete. Different types of mineralogical cements exist in the world, but the most common one by far is still ordinary Portland Cement (OPC). OPC is mainly produced from limestones, which are cheap and widely available all over the world. Apart from being relatively cheap, concretes based on OPC also have a good mechanical and durability performance in comparison to other types of building materials.

Concretes are used for the construction of housing and infrastructure and they are required to maintain their desired engineering properties for long periods of time. Concrete, as a material, is chemically relatively stable at normal ambient conditions and over long periods of time it usually gets stronger rather than weaker. However, a wide range of environmental or loading conditions exist under which concrete or concrete structures are gradually deteriorating. Under such conditions, the performance lifetime of concrete is limited. Predicting the lifetime of concrete and concrete structures, and especially understanding the processes that affect concrete durability are currently highly important research topics.

Concrete deterioration caused by environmental influences include drying shrinkage, freeze-thaw damage, salt scaling, corrosion of reinforcement steel due to ingress of Chloride ions or carbonation, sulfate attack, leaching, acid attack, and weathering processes. Concrete also slowly deteriorates if incorrect types of aggregates are used (i.e., alkali-aggregate reaction – AAR).

Mechanical loading can lead to the slow deterioration of concrete and concrete structures as well, even when the failure load of the material has not been reached. Sustained load will make concrete creep. Creep is a very slow deformation process that can lead to the redistribution of stresses in a loaded concrete structure, which ultimately can cause a structure to fail. In addition, pre-existing flaws or cracks may grow under cyclic or sustained loading and reach sizes that start to impair the durability or even the safety of a concrete structure. The phenomenon of (dynamic) fatigue cracking in concrete has been particularly well studied (e.g. Bažant and Schell, 1993; Horii et al., 1992; Matsumoto and Li, 1999). On the contrary, slow crack growth under sustained load (static fatigue) is a poorly studied and understood phenomenon in concrete.

This PhD-work presented in this thesis 'Subcritical crack growth in hardened cement paste' aimed at making a significant contribution to our understanding of static fatigue in concrete. Subcritical cracking in the cement paste matrix of concrete and along the interface between the matrix and aggregates is believed to be the main reason for static fatigue of concrete. For this reason, this PhD-work focused on measuring subcritical crack growth in hardened (Portland) cement paste.

1.2. Subcritical crack growth in concrete

Slow crack growth (SCG) in concrete under a sustained load (i.e., static fatigue) occurs because of some kind of physical or chemical process that leads to weakening of the material in the crack tip or to a reduction of the fracture energy. These cracks grow slowly because the weakening (transformation) processes in the crack tip are slow, or because transport of certain chemical species towards the crack tip is limiting the weakening process. Since crack propagation occurs at stress-levels below the stress-level for fast (mechanical) crack propagation, slow crack growth is often referred to as *subcritical* crack growth. 'Critical' refers to the state in which the fracture propagates (fast propagation) once the critical stress intensity factor (K_{Ic}) or fracture toughness is reached. In the field of civil engineering, subcritical crack growth sometimes is simply called time-dependent fracture (Hu et al., 1988; Bažant et al., 1995).

Subcritical crack growth can occur in concrete under an externally applied and sustained load. A major pre-existing crack may grow slowly under such conditions, or dispersed microcracks may increase in size and start to coalesce to form larger cracks. In both cases the slow crack growth may ultimately lead to unwanted deformations in a concrete structure. This phenomenon can macroscopically be studied in laboratory by measuring the compressive, flexural or tensile strength of concrete as a function of loading rate. A lower loading rate typically decreases the strength of concrete (Bažant and Gettu, 1992; Mihashi and Wittmann, 1980). This effect is not only caused by subcritical cracking but also by basic creep of concrete (Shah and Chandra, 1970; Bažant and Gettu, 1992; Evans, 1974).

The effect of loading rate on concrete strength shows that subcritical cracking is a real phenomenon in concrete under load. The possibility exists that subcritical cracking occurs under much more circumstances than we currently know. Basically any process in which there is a slow built-up of stresses, subcritical cracking can be expected (Røyne et al., 2011). For example, chemical attack cases (AAR, sulfate attack) that lead to a slow expansion of the aggregates or matrix in concrete could cause cracks to grow subcritically. Whether or not cracks are growing critically or subcritically may affect the type and density of the crack-pattern that will develop. Modeling has shown that fracture patterns generated by a high degree of subcritical cracking have a much lower fracture densities than those produced by dynamic fracture (Schultz, 2000).

Surprisingly, little is understood about subcritical crack growth in cementitious materials, and one could even claim that true subcritical crack growth velocities have never been measured in these materials. The main difficulty is (or has been) to distinguish between creep and cracking effects in concrete if the crack growth process is not optically or otherwise monitored, as will be shown in this thesis. Concrete is the most commonly used building material in the world that is often under sustained load. Moreover it is used in a wide variety of wet and chemically aggressive environment, i.e. in direct contact with sea, fresh, sewage or industrial waste water. In order to make reliable predictions of the lifetime (durability) of concrete in such environments, it is essential to establish the importance of subcritical cracking in hardened cement paste under a range of environmental conditions.

1.3. Scope of research

In the 1970's and 1980's a number of studies on subcritical cracking in cement-based material were carried out by using the traditional Double-Torsion test (Evans, 1972; Williams and Evans, 1973; Atkinson, 1984; Swanson, 1984). As will be explained, when subcritical cracking is measured indirectly as was done in most of these studies, subcritical crack velocities are easily overestimated due to creep effects. Lifetime predictions for concrete based on such measurements will then be unreliable. Moreover, there has been no consensus about the effect of cement paste density (water-to-cement ratio) on the susceptibility to subcritical cracking in these studies (Beaudoin, 1982; Beaudoin, 1985). This is surprising because it is not expected that subcritical cracking shows erratic trends as a function of material density. Finally, there is no consensus about the mechanism of subcritical cracking in cementitious materials (Atkinson, 1984). For these reasons, this research was dedicated to revisit subcritical cracking in hardened cement paste using novel experimental approaches.

A number of experimental methods exist to measure subcritical cracking (Evans, 1972; Freiman et al., 1973; Janssen, 1974). The most popular one is the Double-Torsion (DT) test which is based on the principle that the measured stress-relaxation in a DT specimen is proportional to the crack propagation rate. This test is not necessarily more accurate the other tests, but does have the advantage of having a simple loading configuration and of enabling an easy optical access to the propagating crack. For these reasons, the double-torsion test was chosen in this study, because the prime approach was to measure subcritical cracking optically. Moreover, the use of the standard DT test allows making comparison between the results in this study with those of the previous ones.

A micro-loading device was designed and built to carry out DT test inside the Environmental Scanning Electron Microscope (ESEM) or under Stereomicroscope. The real-time images of the crack tip were recorded to provide direct observation of the crack propagation (e.g., crack-tip movement rate, crack opening width). Post-mortem analysis of these images was performed by Digital Image Correlation Method (DICM) to facilitate crack-tip identification. By measuring the crack growth directly it is possible to elucidate the contribution of creep in causing stress-relaxation of the DT samples. A significant part of this PhD-work was dedicated to the development of reproducible sample preparation and testing protocols to obtain strong observations that form a valuable database for subcritical cracking in hardened cement paste as function of w/c-ratio and relative humidity of the environments.

1.4. Outline of thesis

This thesis consists of six chapters, which describe the background and basic ideas, experimental results and analysis of this study.

Chapter 2 gives a background and literature overview of the key concepts and topics relevant to this research. General ideas about fracture mechanics and fracture behavior of cementitious materials are summarized, especially those related to time-dependent fracture. The accompanying phenomenon of creep is also introduced, and its likely influences in cracking are briefly discussed. Principles of subcritical crack growth in brittle and quasi-brittle materials are described. A comprehensive description about possible driving mechanisms is provided. Previous studies of subcritical cracking

behavior in cement-based materials are reviewed and disscussed. The available experimental methods are summarized, with emphasis on double-torsion method.

In Chapter 3, the materials and methods employed are explained. The procedures of producing, curing and cutting cement paste specimens are described. Basic theories and principles for the double-torsion method are described. The construction of a special micro-testing device designed to perform DT tests to study SCG is described in detail, as well as the specific testing protocols used. Then, necessary data such as the slow crack propagation rate, stress intensity factor, strain distribution around the tip can be obtained for evaluating different governing factors and possible mechanisms. Thereafter, other experimental instruments such as Environmental SEM, stereomicroscope and digital image correlation device are introduced and their primary features are explained. Then, their incorporation with the micro-testing device is described. Possible influences that are resulting from erroneous measurements on the accuracy of the test data are also discussed. Experimental programs of the different tests are summarized, with key parameters presented.

Chapter 4 presents all experimental measurements and observations from all the tests. The test results of single-crystal calcite specimens are presented to examine if, for a non-creeping material, the crack velocities calculated from force-relaxation curves are consistent with those measured optically by using the constructed testing device. The observations for SCG of hardened cement paste under different environmental conditions are provided. DT test results for cement paste specimens are shown with emphasis on the influence of relative humidity and water/cement ratio. Optical observations from the ESEM and stereomicroscope are also shown with post-mortem DICM analysis. The

7

results of creep-induced relaxation tests and self-healing tests using DT specimens are presented.

Chapter 5 combines all the experimental results and observations based on DT tests. An emphasis is placed on the influence of creep-induced relaxation on SCG, and on what the real SCG would be if creep-induced effects were tentatively excluded. Then the lifetime prediction based on traditional SCG studies is updated by taking the creep-induced effects into account for cement paste specimens. Besides, the self-healing of the subcritical crack are presented and discussed, as well as its subsequent effect on the specimen against further SCG. The possible influence of size-effect on SCG is also briefly discussed.

Finally, chapter 6 concludes/summarizes the major findings and provides some suggestions of how these could influence further investigations on related problems in cementitious materials.

CHAPTER 2 Background and Literature review

2.1. Introduction

In this chapter, topics related to subcritical crack growth (or subcritical cracking) are reviewed, including relevant fracture mechanics concepts. The fracture toughness or critical stress-intensity factor is an important parameter that describes the capability of a rigid solid to resist fracture. This is also expected to have a first order effect on the degree of subcritical cracking in materials. In order to compare the subcritical crack behaviors of different materials, the stress intensity factor at which subcritical cracking occurs should often be normalized with respect to fracture toughness. The principles of subcritical cracking are introduced in this chapter for different materials, as well as the proposed mechanisms. Also the different testing methods used are reviewed. Various aspects related to fracture in cementitious materials are addressed. These include the effect of moisture content, which is not only important under fast loading conditions, but also in subcritical crack growth. Also, the heterogeneous, multi-scale nature of cementitious materials is described since it plays an important role in fracture processes, as well as subcritical cracking.

2.2. Fracture mechanics concepts

2.2.1. Fracture toughness

An important parameter in fracture mechanics is the stress intensity factor (K) which was proposed by Irwin (1958). It characterizes the stress state at the crack tip as a function of remote load and specimen's crack configuration and is a measure of a solid's capability to resist fracture.
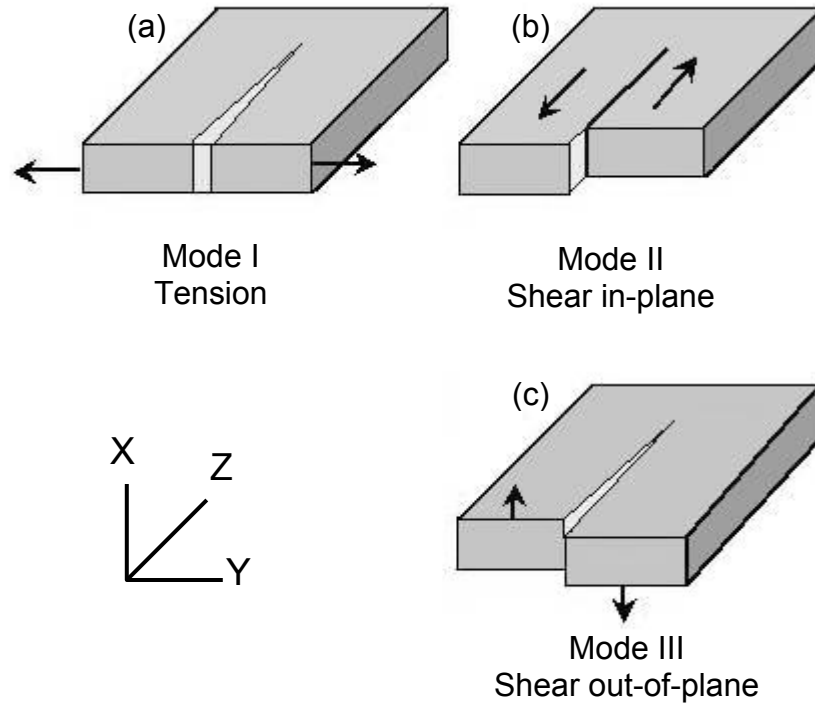
Figure 2.1. Fundamental modes of fracturing: (a) the crack opening mode (Mode I) due to tensile stress normal to the crack plane; (b) the crack sliding mode (Mode II) due to shear stress in the crack plane; (c) the crack tearing mode (Mode III) due to out-of-plane shear stress.

In general, the stress situation of an arbitrary crack can be considered as the Mode I, Mode II, Mode III or a mixed mode of them (see Figure 2.1). Mathematical treatment applied to Mode I fracture can be applied similarly to other modes of fracture (Shah, 1994). The stress field in the area around a Mode I crack tip (see Figure 2.1a) can be expressed in terms of stress intensity factor as (Lawn and Wilshaw, 1975)

$$\sigma_{i,j} = K_A /(2\pi \cdot r)^{1/2} \cdot f_{i,j}(\theta) \qquad (2.1)$$

where $\sigma_{i,j}$ is the stress in Cartesian coordinate system (i, j), K_A stands for a certain mode of stress intensity factor, r and θ are the transformations of (i, j) in polar coordinate

10

system, $f_{i,j}(\theta)$ is a function of θ, and depends on the load and specimen geometry. The stress intensity factor for a two-dimensional crack can be determined by

$$K_A = Y\sigma_\Gamma(\pi \cdot a)^{1/2}$$

(2.2)

where Y is a dimensionless shape constant to account for the crack geometry, σ_Γ is the remote applied stress, a is the crack length for a single-tip crack (or 1/2 of the crack length for a penny-shaped, internal crack with two tips). Taking mode I as an example, K can also be given in terms of fracture energy as

$$K_I = (G \cdot E)^{1/2}$$

(2.3)

for the plane stress conditions, or

$$K_I = [G \cdot E /(1-\mu^2)]^{1/2}$$

(2.4)

for the plane strain conditions, where K_I is for mode I condition, G is the strain energy release rate, E is the Young's modulus and μ is the Poisson's ratio. The plane stress (Equation 2.3) and plane strain (Equation 2.4) conditions illustrate two idealized stress states. In a simplified consideration, the plane stress condition is suitable for a structure with its one dimension being negligible if compared with the other two (e.g. a thin plate) and subjected to in-plane loading. The plane strain condition is suitable for a structure with its one dimension far larger than the other two (e.g. a long cylinder with small radius) and subjected to transverse loading.

A crack in brittle/quasi-brittle materials propagates when a certain criterion is satisfied: the stress intensity factor has to exceed a critical value, known as fracture toughness or K_c (in most cases K_{Ic} of Mode I loading configuration is employed), which is widely accepted as an inherent material property (Lott and Kesler, 1964; Jenq and Shah, 1985).

For a certain material, if the fracture toughness is known and the stress conditions can be obtained, the critical stress or the critical size of the crack required to cause catastrophic failure can be derived. Thus, it allows the determination for the safety-domain of crack sizes, the critical load on a structure at the moment of failure, the suitability of the materials used for manufacturing and the feasibility of the structure design. A large amount of literature can be found on the fracture behavior of glasses, ceramics, polymers, metallic and concrete materials. They are mainly based on critical stress intensity factor approaches to deal with catastrophic failure problems.

2.2.2. Fracture propagation

Apart from the concerns about the conditions under which a crack can be initiated, the problem of how it will grow after initiation is also essential in understanding the failure of a material. A general description of energy rate function for elastic cracking is shown through studies on quasistatic crack propagation problems (Gurney and Mai, 1972) as

$$P \cdot du = dA + R \cdot dA + dU_K \tag{2.5}$$

where P is the force applied, u is the displacement, A is the strain energy function, R is the specific work of cracking, A is the crack area and U_K is the kinetic energy. Through interpreting the kinetic energy U_K in terms of motion of crack-boundary mobile species and in terms of crack length during quasistatic loading under constant load, the energetically activated crack velocity can be derived as (Anderson and Grew, 1977; Lawn, 1993)

$$v = (\frac{2\pi E}{k' d(1-\mu^2)})^{1/2}(1-\frac{a_0}{a}) \tag{2.6}$$

or

$$v = (\frac{2\pi E}{k' d(1-\mu^2)})^{1/2}(1-\frac{a_0}{a})^{1/2} \qquad (2.7)$$

where v is the crack velocity, k' is a constant related to Poisson's ratio μ, d is the density of the cracked material, a is the instantaneous crack length the same as defined in Equation 2.2 and a_0 is the corresponding initial crack length. These two equations are generally similar, however Equation 2.7 is more convenient to calculate time of cracking if the crack length a is very large.

A crack can propagate either in a stable (ductile) way or in an unstable (brittle) way (Mai and Atkins, 1980). Being stable requires that the crack grows only when the applied load is raised. Thus stable cracks are relatively simple cases and can be visually tracked. Unstable cracks, also called spontaneous crack, can grow in a self-sustained manner without the need of additional loading. In this case, the energy released into the crack tip is larger than the amount required for propagation, implying that the time-independent crack behavior is more complex and difficult to predict. Figure 2.2 shows the basic cases. It shows that unstable cracking occurs only after the peak load.
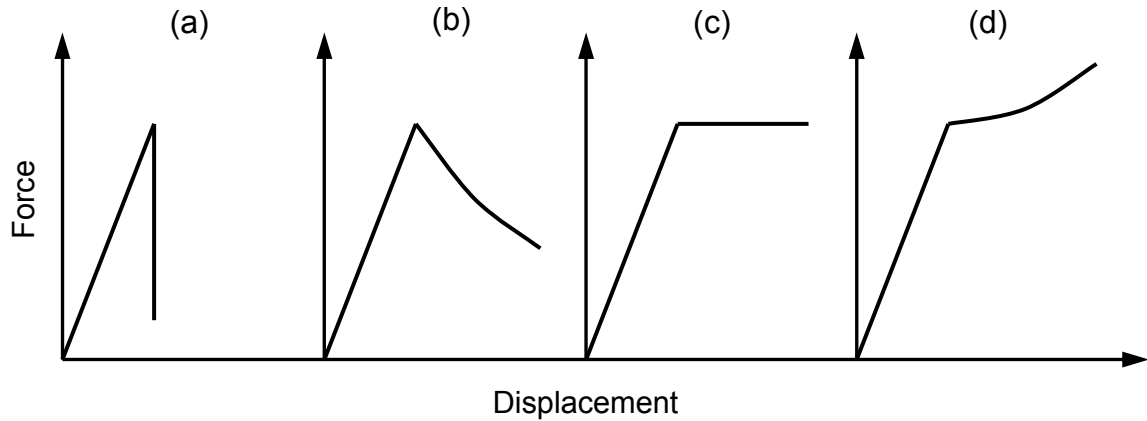
Figure 2.2. Typical diagrams of force-displacement pattern for cracking. (a) is unstable cracking along with sudden drop of applied force; (b) is stable cracking with gradual decrease of applied force; (c) is stable cracking with constant applied force; (d) is stable cracking with gradual increase of applied force (according to Mai and Atkins, 1980).

The upper limit of crack velocity is widely considered to be theoretically bound by the Rayleigh surface wave speed in the respective materials (Freund, 1979; Broberg, 1989). However this limit is found by, both experimental and simulation studies, to be $\sqrt{2}$ times the shear wave speed (Rosakis et al., 1999; Gumbsch and Gao, 1999).

2.3. Fracture behavior of cementitious materials

2.3.1. Microstructure

Multiple phases exist in cementitious materials at different scales as shown in Figure 2.3. A major component of cementitious materials is calcium silicate hydrate (C-S-H), which is the most abundant reaction product (50-60% of the cementitious matrix). C-S-H gel possesses amorphous disordered appearance. It is as shown in Backscattered Electron (BSE) images (Figure 2.3a and b). It consists of hydration products of cement clinker components. C-S-H gel forms the continuous matrix of the hardened paste and binds

14

other cement particles and aggregates (e.g. sands, see Figure 2.3a, c and d). Unhydrated cement grains, identified as bright white areas in Backscattered Electron images, exist in nearly all cement pastes. They are the unreacted remnants of clinker minerals (e.g. alite, belite, aluminate and ferrite, see Figure 2.3b) and can continue to hydrate, once being exposed to water. Lower water-to-cement (w/c) ratio will lead to higher proportion of unhydrated cement particles and therefore a lower degree of hydration for a cementitious material. Other components, such as calcium hydroxide (CH) and calcium sulfoaluminate (ettringite or monosulfate), exist in a dispersed way in the C-S-H phase. They have distinctive hexagonal-platy and needle-like morphologies, respectively. At meso-scale level the cement paste matrix can be considered as one phase with aggregates being the other one (Shah and Ouyang, 1994). Air voids also exist in the cement paste matrix, their sizes and porosity decrease with higher degree of hydration or lower w/c ratio.

C-S-H gel is responsible for the mechanical properties of the hardened paste, e.g. strength (Alizadeh et al, 2010). Interlayer water is considered to be present between the layers of C-S-H and significantly influences the strength of C-S-H. Higher water content will reduce the strength of C-S-H and in turn weaken the strength of the cement pastes (Alizadeh et al, 2010; Wittmann, 1973; Sereda et al., 1966). Other hydration products such as CH and ettringite only exist discretely within the C-S-H matrix, and therefore cannot form strong solid phases to reinforce the hardened paste. Their contribution to the strength is mainly through the reduction of the total pore-volume by converting certain amount of liquid water into their crystal structures.
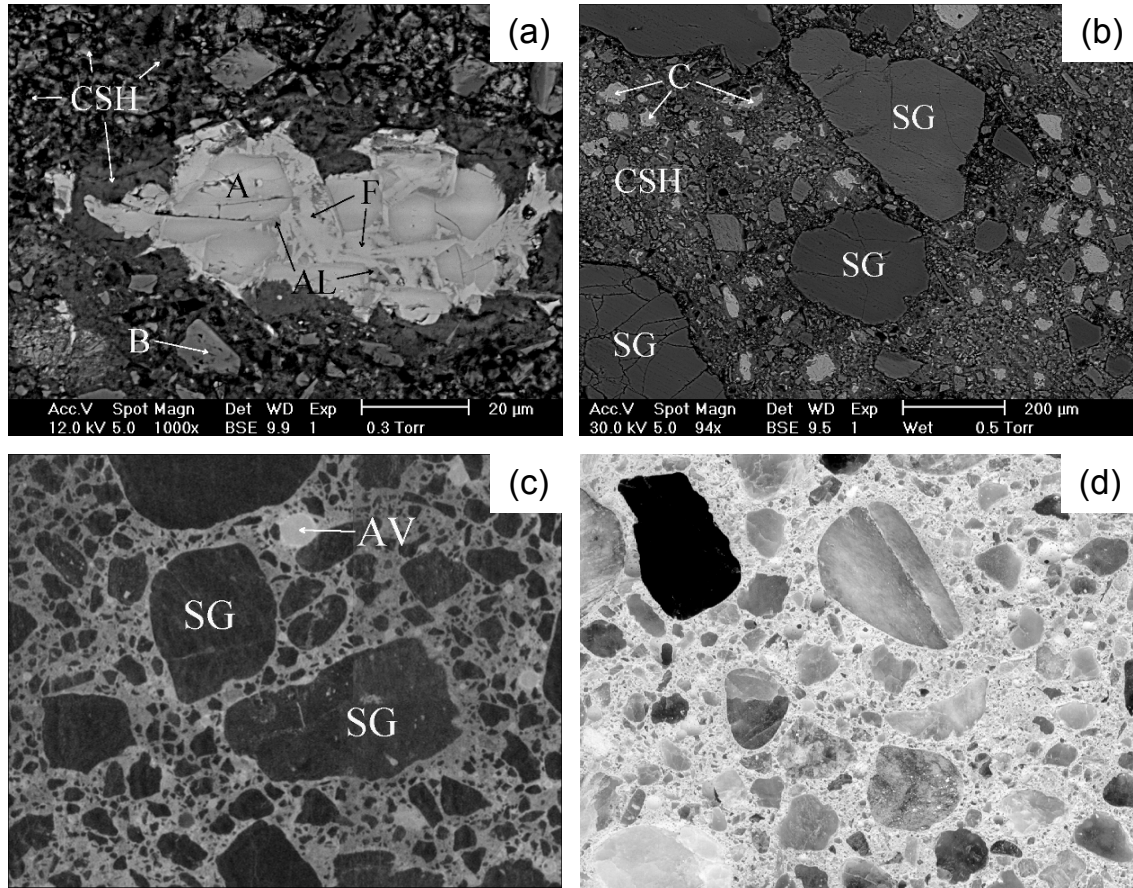
Figure 2.3. Multilevel structure of concrete. All images are from the same concrete, with an age of 28 days. (a) Partially unhydrated cement grain embedded in hydration products (CSH-gel). A = Alite, B = Portlandite crystal, F = Ferrite, AL = Aluminate. ESEM–Backscattered Electron recording; (b) Micrograph of matrix showing sand grains (SG) and unhydrated cement grains (C); (c) Mesolevel structure of concrete. SG = sand grain, AV = air void. Optical microscope–Ultraviolet light recording. Image size is 15 x 12 mm; (d) Mesolevel structure of concrete. Scanning-recording. Image size is 70 x 55 mm; (reproduced with permission from Bisschop, 2002)

Cementitious materials contain internal defects with sizes ranging from nanometers to millimeters. These defects are mainly pores and cracks present in the cement paste matrix, while their number and distribution can influence the mechanical properties of the materials. The pores, as a result of hydration reactions, include gel pores of fine sizes ranging from around 0.5 nm to 10 nm and larger-size capillary pores varying up to 10 μm. The cracks are due to thermal gradients, moisture-content variations and etc., their

16

existence inside the bulk before any external load being applied has been shown by others (Hsu, 1963; Slate and Olsefski, 1963). These cracks can occur at the interface of neighboring phases, which are the cement paste matrix and the aggregates of the concrete, as a result of bond failure (Cordon and Gillespie, 1963; Hsu, 1963; Slate and Olsefski, 1963). There can also be shrinkage cracks that are due to the tensile stress build-up in the paste during the loss of moisture. This type of cracks is only present in the cement paste matrix (Shah and Ouyang, 1994) and the inducing shrinkage is restrained by stiffer particles or boundary conditions. In areas of high stresses, the defects are able to function as stress-raisers to induce localized stress-concentrations, which can lead to mechanical failure of the cementitious material structures at stress-levels well below theoretically-expected strength. This strength-limiting effect has been discussed by various investigators (Yuan and Guo, 1987; Kaplan, 1959; Larrard and Belloc, 1992) just with some exceptions for high strength concretes (compressive strength > 41 MPa) where aggregates play an important role (Alexander and Davis, 1989; Baalbaki et al., 1991; Giaccio et al., 1992).

2.3.2. Stress-strain curve

Cementitious materials behave mostly in a quasi-brittle manner under loading with nonlinearity appearing in the crack-tip region prior to peak stress. Also due to the presence of nonlinearity in real materials, stresses at crack tips will not easily reach singularity. However, for only a short period of loading, a well hardened cement paste specimen can be treated approximately as a linear elastic material (Haecker et al., 2005).

A typical stress-elongation curve for a cementitious material like concrete under uniaxial tensile load is presented in Figure 2.4 (Gopalaratnam and Shah, 1985; Li et al., 1993). As indicated, four stages exist in the figure:
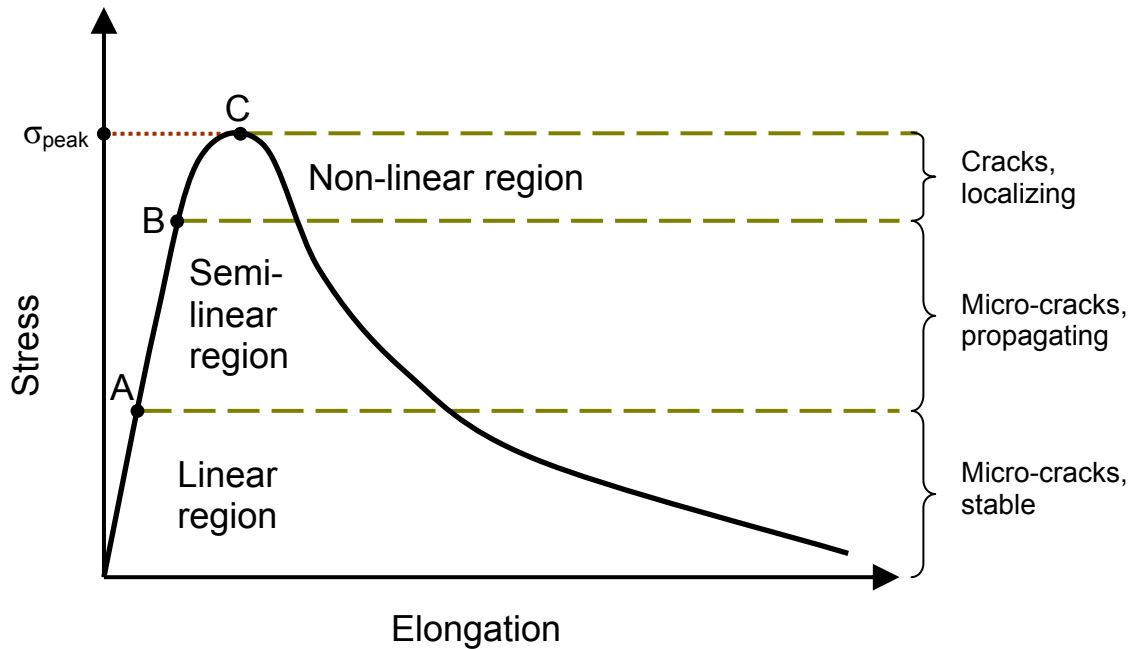
Figure 2.4. Stress-elongation curve for a cement-based material showing stages of crack propagation under tension (according to Li et al., 1993). "Semi-linear" means a mild non-linearity behavior.

Stage I — from the origin to point A, during this part the load is increased to around 30% of the peak load. The material behaves linear-elastically with internal defects being inactive through the whole bulk.

Stage II — from point A to point B, the load is increased to around 80% of the peak value. During this loading period internal defects start to play a role in the mechanical response by extending and propagating in the matrix. The loss of linearity starts to occur. However, the micro defects are still uniformly stressed inside the material compared with each other and stay relatively stable.

18

Stage III — from point B to point C, the load is further increased to the peak. At this stage, the linear behavior is lost. Micro defects continue to grow, as well as to emerge, in the weakest parts of the material and the most fragile micro defects begin to coalesce with each other to form macro ones – major cracks. Localized damages occur and keep developing as a result of the propagation of these major cracks until the maximum load is reached.

Stage IV — period after point C, the load is dropping but the major crack extends its propagation in a fast and self-sustained manner with the continued accumulation of damaged areas until final failure.

Therefore, the failure process of a cement-based specimen under tension starts from micro-cracking, then through developing, enlarging, coalescing of micro-cracks, finally ends at major cracking. Similar characterization of failure processes for specimens under compression can be found elsewhere (Bieniawski, 1967; Mehta and Monteiro, 1993), but with the occurrence of crack-closure stage at the very beginning.

2.3.3. Effect of loading rate on strength

It is well known that the loading rate has a significant effect on the flexural or compressive strength of cement paste, mortar, and concrete (Mindess and Nadeau, 1977; Mindess, 1985; Wittmann, 1985; Bažant et al, 2000): The lower the loading rate, the lower the strength, as shown in Figure 2.5. This dependence can be generally explained as: Microscopically, the probability of rupture of thermal activated atomic (or molecular) bonds increases with decreasing loading rate, which in turn facilitates the crack growth and decreases the strength at macroscopic scales (Bažant and Gettu, 1992; Wu and

19

Bažant, 1993). In addition to the growth of (micro-)cracks, creep is also considered to be rate-dependent, except at very high loading rates (Bažant et al, 2000). For cementitious materials, water-assisted weakening processes (corrosion effect and disjoining pressure exerted by inter-layer water in C-S-H) are proposed to be rate-dependent micromechanical processes (Wittmann, 1985). On the other hand, even under static load before the fracture stress is reached, failure can still be observed, and the failure time increases with lower load (Barrick and Krokosky, 1976; Husak and Krokosky, 1971). An example is shown in Figure 2.6 for concrete (Wittmann, 1985). This time-dependent failure observed was attributed to subcritical cracking and creep effects (Barrick and Krokosky, 1976; Bažant and Gettu, 1992).
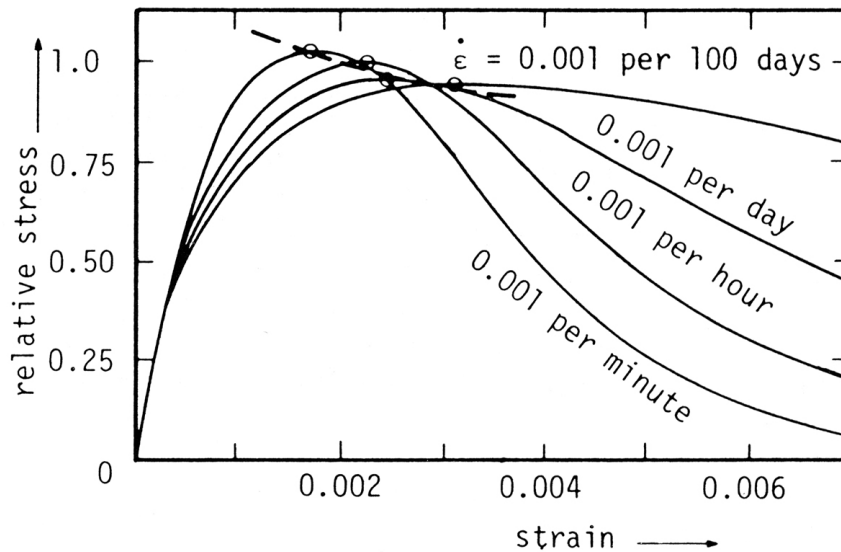
Figure 2.5. Stress-strain diagrams from identical concrete specimens under different loading rates (see: Wittmann, 1985).

η = σ/σ₀,
σ = applied stress;
σ₀ = ultimate stress under standard loading conditions.
t = lifetime (time of concrete failure)
τ = age at time of loading (= 50 days)
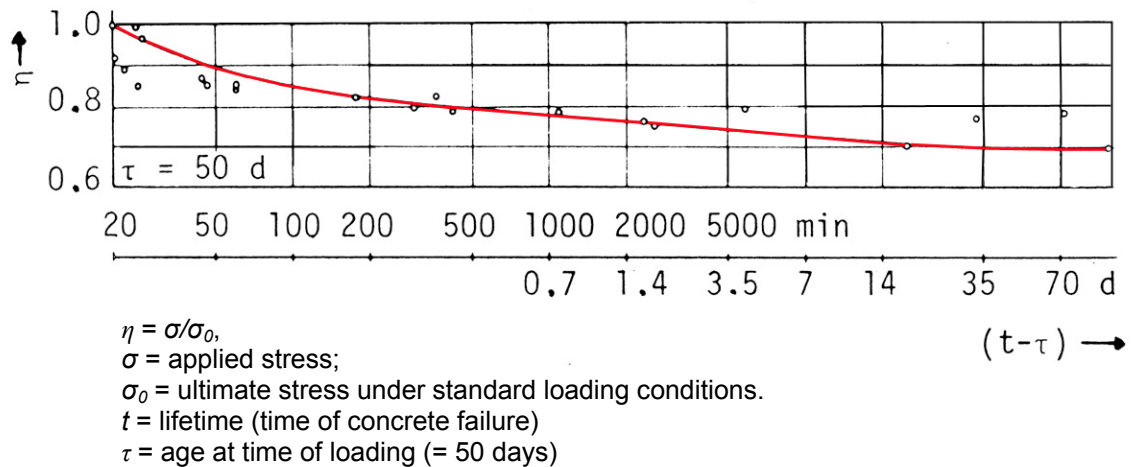
Figure 2.6. Static fatigue (lifetime) of concrete under high sustained load (see: Wittmann, 1985).

Concerning the interaction between creep and fracture, it becomes more complicate (refer to Chapter 2.3.5 for more details about creep). The rate of crack propagation is important in determining the fracture of cementitious materials and creep of the materials surrounding the crack tip can divert part of the energy needed for propagating the crack. When a material is subjected to slow loading or arrest of the crack mouth opening, creep can cause significant stress relaxation around the crack tip (i.e. in the fracture process zone), which is equivalent to the effect of unloading (Bažant, 1993). However, creep can also decrease the fracture resistance of the material, leading to lower strength at lower loading rates (Wittmann, 1985). Therefore, it is expected that the interaction between fracture and creep in cementitious materials is important for durability analysis (Bažant and Gettu, 1992).

2.3.4. Effect of moisture content on strength

In cementitious materials, water exists as free water in voids (i.e. in capillary pores), partially-bound water (i.e. gel water) or as chemically-bound water in the hydration products (i.e. interlayer/interparticle water in C-S-H gel). The free and partially-bound water can be affected by the moisture content (i.e. relative humidity) of the environment.

The strength (compressive and tensile) of concrete was found to be dependent on the moisture content of the environment (Wittmann, 1973; Sereda, 1966). A series of tests ranging from fully-dry to fully-wet concretes under both dynamic and static-loading conditions showed that the strength is higher for drier specimens (Ross et al. 1992; Ross et al. 1996). It was early proposed that the interlayer water in C-S-H gels plays an important role (Feldman and Sereda, 1970). The redistributed water exerts pressure on the gel surfaces, which weakens the inter-particle forces of the C-S-H gel and lowers the specific surface energy. And such effect is considered to cause lower fracture energy in concrete (Bažant and Prat, 1988). There are also studies proposing that the adsorbed water in the concrete could cause the C-S-H gel to dilate, leading to strength-weakening of the solid (Galloway et al., 1979). However, disagreement exists among studies on the real physical processes governing the moisture-dependence of strength, because various hydration products and specimen preparation methods lead to difficulties for making conclusions (Wittmann, 1973).

2.3.5. Creep

Unlike most brittle materials, a hydrated material as a cementitious one is not only sensitive to load and temperature but also to water content. As a consequence, when

22

under load or during drying, it exhibits deformation. The type of deformation due to external load is creep. The type of creep is considered to be basic creep if the material is in equilibrium with the environment, while to be drying creep if the material is not in equilibrium with the environment (Tamtsia and Beaudoin, 2000). It's well known that creep of concrete can last for many years without reaching a limit. There are both a recoverable part that occurs in a relatively short time and an irrecoverable part that lasts longer and is more critical. In the former part, water diffusion due to hindrance pressure change under external load, is thought to be dominant. The latter part can be the result of ever-lasting hydration or new bonding between interlayers moving closer in the matrix of cement paste (Powers, 1968). The exact mechanisms of creep in cementitious materials are not well understood, with several theoretical proposals available such as stress induced activated microcracking, stress induced redistribution of internal water or the sliding of adjacent interlayers over each other (Feldman, 1972). The w/c-ratio and specimen age can have some influence over the creep. Higher w/c-ratio or lower specimen age leads to lower strength, to which the modulus of elasticity is related. Creep is therefore expected to increase with w/c-ratio and decrease with specimen age (Soroka, 1993; Wang and Zhu, 2011).

It has been shown that water plays an important role in creep of cement-based materials, like hardened cement paste and concrete (Wittmann, 1973). The creep is apparently hindered under dry conditions, and is present under wet conditions. If water content is higher, creep is more pronounced. Basic creep is shown to be more pronounced above around 40% relative humidity, suggesting a possible acceleration due to weakened internal bonds (Wittmann, 1970). Completely-dry cement pastes exhibit negligible or

even no creep (Mullen and Dolch, 1964). Microstructure changes could happen in cement pastes when they are dried first (Bentur et al, 1979). The exchange of water in the pastes with organic fluids has shown no significant creep and swelling, which also suggests the possible change of structures during drying (Day, 1981). Hardened cement pastes cured at ambient temperature show a less pronounced secondary stage creep at latter times, suggesting the different pore size distribution patterns (Sellevold and Richards, 1972).

Some thoughts about interlayer hypothesis are also proposed (Feldman and Sereda, 1968). These consider that creep originates from the ongoing crystallization or aging of certain layered structures of silicates. This can then be influenced by water diffusion or local stress built-up. New spaces could form primarily between compacted layers of C-S-H gels when under stress, and this process is mainly irrecoverable. When the stress is released, some water will diffuse into the new interlayer space, causing the recovery of creep (Bažant, 1985).

Creep through a water-lubricated slip process between C-S-H particles that are close to each other is proposed to be another possibility (Ruetz, 1968). However, it anticipates that an increase of macroscopic water flux would lead to an increased creep rate due to microstructure disorder, but this is not well supported by water permeation tests at constant rates that showed no evident increase of creep rate with higher water flux (Bažant, 1972; Bažant, 1985).

Another hypothesis considers thermally-activated micro-regions in the paste to be responsible for the creeping behavior with time evolution (Klug and Wittmann, 1974). These regions described as creep centers are able to lower the deformation energy barriers when subjected to stress or temperature. Creep slows with time, which is then

24

thought to be due to possible depletion of creep centers that enable the creeping (Bažant, 1972).

Moreover, microfracturing is regarded as one of the primary mechanisms of creep in most brittle inhomogeneous materials (Scholz, 1968a), including cementitious ones. Under applied stress, the materials' complex microstructures with cracks and pores tend to produce fluctuation of stress field at the local level, resulting in microfracturing. Accumulation of microfracturing leads to incremental increase of strain in a time-dependent manner (Scholz, 1968a). The creep rate can be determined in terms of the applied stress, following a power-law relation (Scholz, 1968b), with the exponent approaching unity when the stress is low and being higher when the stress is higher.

2.4. Principles of subcritical crack growth

2.4.1. Driving force and rate-limiting steps

In a brittle solid, a sharp crack will be initiated once the critical value of stress intensity factor K_{Ic} is exceeded. It will then propagate at the velocities close to the magnitude of the sound-wave speeds, in the order of up to 10^3 m/s. Many studies in glass, ceramics, quartz and rocks etc. have revealed that cracks can grow at stress intensity factors well below K_{Ic} (e.g. Wiederhorn, 1967; Wiederhorn, 1968; Scholz, 1972; Atkinson, 1982). This phenomenon is called subcritical crack growth (SCG) or slow crack growth and the time duration can be very long in contrast with the rapid crack growth mentioned above. It is the main type of stable crack growth and depends on environmental conditions, usually involving water or chemical agents (Swanson, 1984; Wiederhorn et al., 1982). From a general point of view, the chemical actions resulting from these agents potentially

weaken the strained bonds at crack tips lower the energy requirement for crack growth and thus enable fracture propagation. The velocity of subcritical crack propagation is normally less than 10^{-1} m/s and depends on the material properties as well as applied load levels.

Subcritical cracking will occur only in a certain range of stress intensity factors. The upper limit is obviously the fracture toughness K_{Ic}, above which the slow crack growth shifts into more rapid and spontaneous mode. The lower limit is some threshold value K_o, below which the slow cracking velocity reaches zero. The exact value of K_o may be not evident for some other materials even at very low velocities, but its existence is widely-accepted (Atkinson, 1984). Within this range, the specific relationships between stress intensity factor and crack velocity are dominated by the crack propagation mechanism as well as the interaction between environmental conditions and material microstructure. A schematic illustrations for the stress intensity factor (K) versus crack velocity (v) are presented in Figure 2.7, including both the theoretical diagram (Figure 2.7a) and experimental measurements (Figure 2.7b).
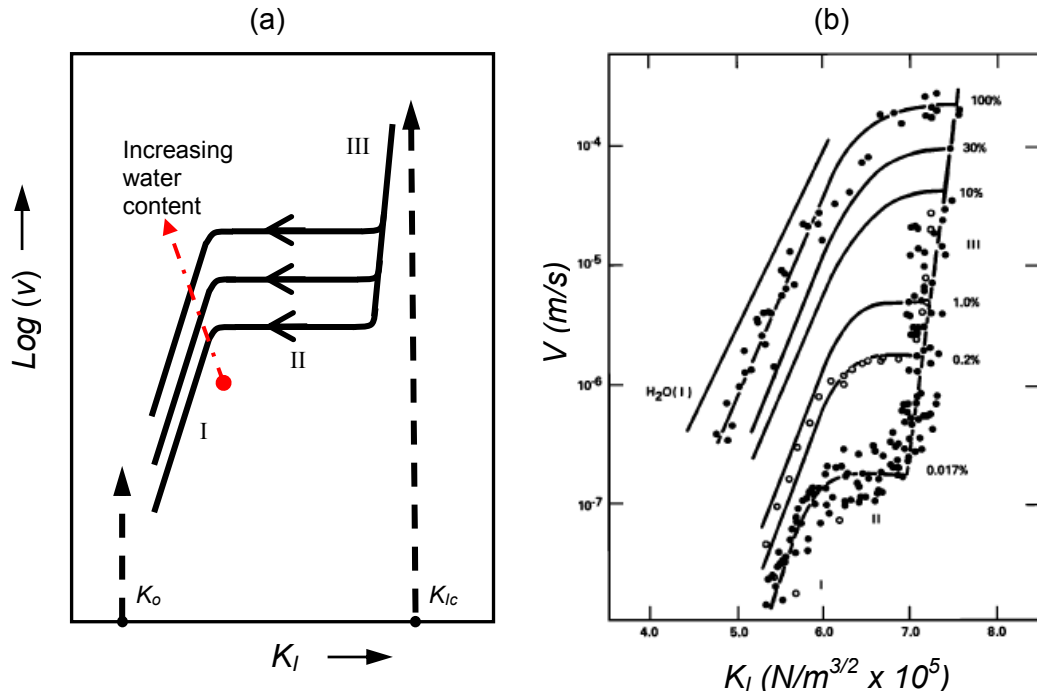
Figure 2.7. Schematic and experimental plots of *stress intensity factor (K_I)* versus *crack velocity* (*v*): (a) under tensile loading configuration, in logarithmic scale (according to Freiman, 1984); (b) the popular example of soda-lime-glass in a nitrogen atmosphere (according to Wiederhorn, 1967). The arrows on the curves indicate how normal processes proceed with time. K_{Ic} is the critical stress intensity factor of the material. K_o is the threshold stress intensity factor below which no slow crack growth is observed. I denotes the section of the corresponding curve where environment assisted deterioration processes at crack tip dominate the crack propagations. II denotes the section where transport of reactive species from surrounding environments to crack tips determines the cracking rates. III denotes the section, where rapid cracking occurs, is mostly independent of environmental influences.

An ideal diagram of *K−v* relationship based on the studies for glasses and ceramics (Freiman, 1984) is as presented in Figure 2.7a. Each curve contains three regions, which evolve in the sequence of III→ II→I over time as shown in the experimental studies. However, not all of the three stages have to be present in other materials, even some glasses or ceramics as the materials' structures or properties can be different and will influence the respective *K-v* interactions (Atkinson, 1984). The most commonly known

27

K-v diagram showing three regions is also shown in Figure 2.7b to provide a straightforward comparison (Wiederhorn, 1967).

In region I, the slope of the curve typically depends on the material and also on environmental conditions (see Chapter 2.4.2). The crack velocity is in the range up to 10^{-1} m/s, with lowest reported value of around 10^{-12} m/s (Simmons and Freiman, 1981, Wilkins, 1980). The majority of the lifetime-relevant crack velocities for a long-term loaded material are in this region. In this stage, active ingredients (e.g. H_2O) from the environment interact with crack tip materials and significantly lower the strength of tip bonds. The reactions (Wiederhorn, 1967) are enhanced by stress and cause bond-breakage before the consequent cracking can continue in a self-sustained manner. The influence of H_2O from the environment is stronger when the content or concentration of water is raised (Figure 2.7a). The curves tend to be displaced to the top-left corner of the diagram. The occurrence of such behavior could be due to higher concentration of water molecules at the crack tip, resulting in stronger chemical reactions and consequently lower resistance against subcritical cracking.

The crack then propagates with its K_I at the tip lower than the required criterion of K_{Ic}. The reaction products formed can be corrosive or not corrosive (Wiederhorn, 1967). Through the comparison of surface energy of glass in air and vacuum, it was suggested that contributions, which reduce the surface energy and consequently the strength of the material, can also come from attached species to the crack surface (Orowan, 1944). The rate-limiting factor is the respective reaction-rates at the crack tip.

In region II of higher K_I, the curve nearly falls flat with slopes near zero. There is little change of velocity at different stress intensity factors, just with slight dependence on K_I

originating from specimen configurations in experiments (Freiman, 1984). In this stage, the reaction rate reaches its limit and cannot increase further with increasing K_I. Due to the discrepancy between the crack-tip propagation speed and the transport rate of reactive species to the tip, the supply of these species is unable to keep up with the need of higher crack velocities. Therefore, the rate-limiting factor is the transport rate of surrounding reactive species.

In region III, the curves are quite steep with the slopes much larger than those in region I. From after the transition points at the end of region II, the crack velocity accelerates with increasing K_I to approach fast-cracking speed in the respective medium, faster than the reactive species' transport rates. However, the crack growth is still stable and of subcritical type until reaching K_{Ic} (similar as the case in Figure 2.2d). In this stage, the surrounding environments have little influence on the crack growth rates, while K_I has a strong influence. Compared with region I and II where chemical effects play an important role, the mechanical behavior is dominant in region III (Wiederhorn et al., 1982). For example as shown in Figure 2.7b, water vapor does not have significant effect on crack velocities in Region III.

2.4.2. Slope of the *K-v* diagram

A linear least square fit to the data within the region I can be extracted to obtain a value, known as the slope while denoted as *n*. This parameter is a constant for the material, known as subcritical crack index, and it reflects the material's capability to resist subcritical cracking. Higher *n*-values correspond to higher resistance against subcritical crack propagation and more brittle fracture within less time. A diagram

29

showing the relative values of *n* for a series of brittle materials is presented in Figure 2.8

(according to Swanson, 1984). A general trend can be identified from the figure that

higher degree of heterogeneity tends to show higher relative resistance against subcritical

crack growth. The *n*-value can also be used as an input in the lifetime analysis of brittle

materials under different types of load conditions (Hu et al., 1988).
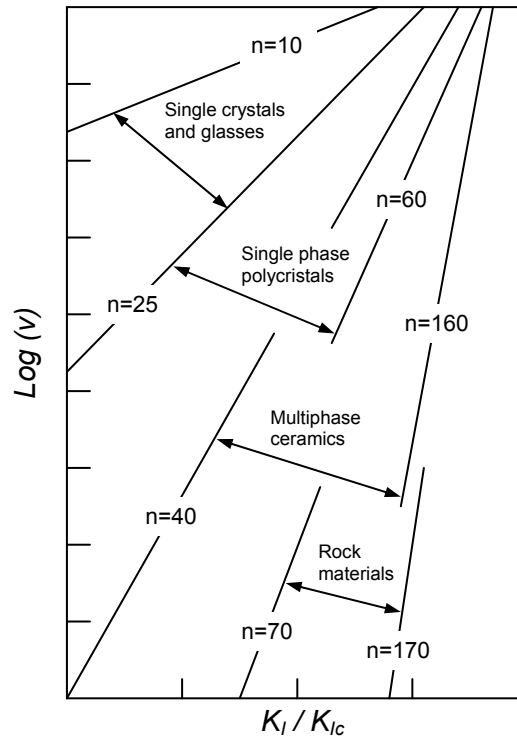
Figure 2.8. Schematic illustration of relative subcritical indices for common brittle
materials (according to Swanson, 1984). Normalization of K_I is based on
materials' respective K_{Ic}.

2.4.3. Proposed mechanisms for subcritical crack growth

The physicochemical processes of the mechanisms for subcritical cracking are

suggested to be stress corrosion, adsorption of the environmental species, diffusion of the

aggressive species, dissolution of the materials at crack tips, ion exchange and

microplasticity (Atkinson, 1984; Freiman et al., 2009).

Stress corrosion: The concept of stress corrosion was first brought up for metals under load before their yield point, and then extended to nonmetallic materials such as glasses, ceramics, etc. in adverse environments. There is no universal agreement on the definition of stress corrosion for nonmetallic materials, and subcritical cracking (or static fatigue) is used in many studies to stand for it. However, concerning the basics of stress corrosion, the hypothesis that aggressive species react at the crack tip rather than in the interior of the material is widely accepted (Anderson and Grew, 1977). And a general adaptive equation outlining the processes can be expressed as (Atkinson, 1984; Michalske and Freiman, 1982):

$$n\text{A} + \text{B} \leftrightarrow \text{B*} = \text{products} \tag{2.8}$$

(1) Transport of the active species to the crack surface;
(2) Adsorption of the species;
(3) Reaction at the adsorption site;
(4) Desorption of the reaction products;
(5) Removal of the products.

In Equation 2.8, A denotes the environmental species, n is the number of A, B denotes the crack tip bond and B* is its activated status. There is not much information about which step determines the overall rate. An example of the bond rupture process facilitated by H_2O proposed for stress corrosion reaction in silica glasses is presented in Figure 2.9.
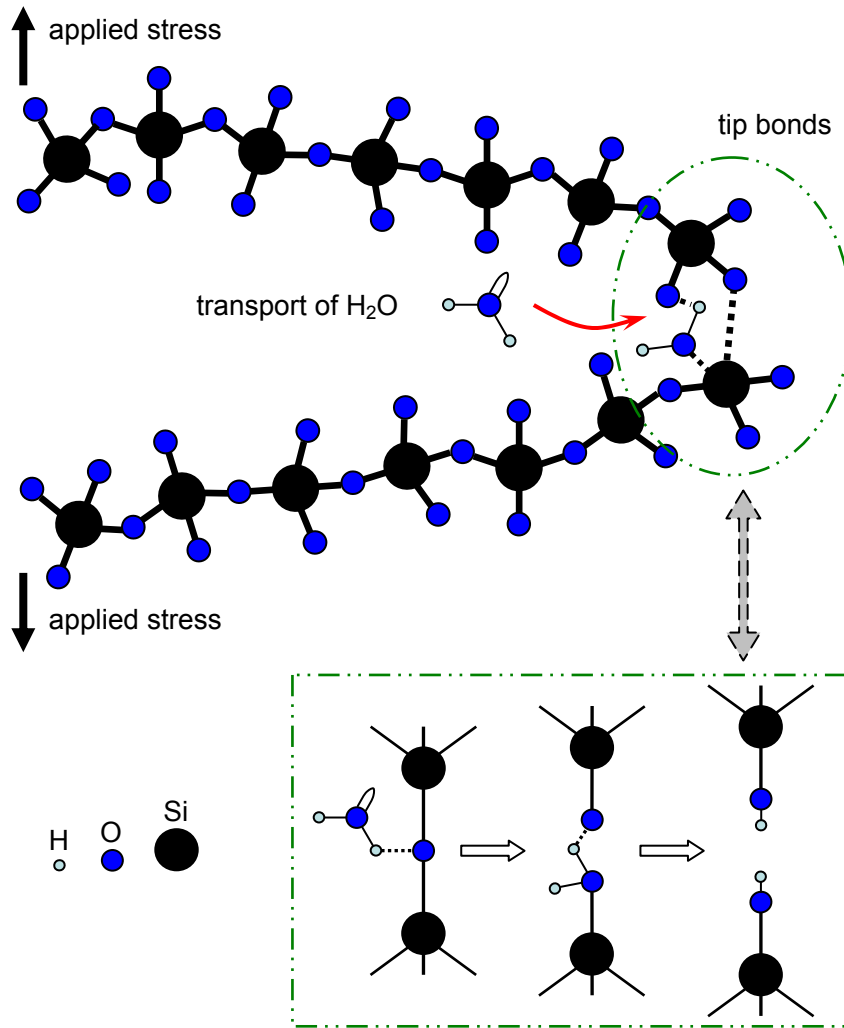
Figure 2.9. Schematic illustration of the hydrolysis process of stress corrosion at crack tip for glass.

Adsorption: Fracture surface energy was found to be dependent on the surrounding environment, based on early studies on mica (Orowan, 1944). The lowering of the fracture surface energy, due to adsorption of environmental species (i.e. water molecules) to the crack surfaces, was suggested to be responsible for the findings (Orowan, 1944; Lawn, 1983). The rate of crack growth was suggested to be controlled by the diffusion of the adsorbed species to the crack tip. However, the difference between this adsorption theory and the stress corrosion theory (also includes adsorption process) was considered

to be trivial. There are major similarities such as the crack growth pattern (i.e. in exponential way), the existence of crack healing and experimental parameters (e.g. stress intensity factor) between these two theories (Freiman et al., 2009). The difference was suggested mainly to be that the adsorption theory emphasizes on the lowering of surface energies while the other one emphasizes on the bond-rupture reactions.

Diffusion: Subcritical crack growth at high temperatures can be controlled by the mass transport processes, which has been shown for ceramics (Dutton, 1974). Possible paths for the diffusion include bulk diffusion, surface diffusion, grain boundary diffusion or diffusion through gaseous phase, of which the grain boundary diffusion is most likely at relatively low temperatures (Stevens and Dutton, 1971; Dutton, 1974). Concerning materials with internally bound chemical impurities such as structural bound water, they can as well have an aggressive effect on the materials even with very small quantities (e.g. Griggs and Blacic, 1965). Diffusion of these impurities can be led towards the crack tips under the influence of stress, then participate in the degrading reactions or enhance dislocation activities, thus promoting the crack propagation (Dutton, 1974).

Dissolution: Studies on Na_2O-SiO_2 glasses and calcite rocks have suggested a possible dissolution of crack tip materials into the ambient solution (e.g. water), which in turn facilitates the crack extension (Simmons and Freiman, 1981). Just with a small stress, the products can be released into the environment and thus enhance the cracking. This claim is supported by the observation that acceleration of cracking is pronounced at low crack velocities (i.e. 10^{-8} to 10^{-9} m/s in this case) in region I, where the dissolution rate is expected to be relatively fast to exert some influence. For high K_I region where crack velocities are higher, this dissolution-mechanism is not applicable.

Ion exchange: Ion exchange is based on two conditions: (a) there is species in the surrounding environment that can change its ions with the tip materials; (b) replacement of ions will lead to lattice strain due to resulting lattice mismatch (Atkinson, 1984). Then the crack propagation will be facilitated when stressed. Another possibility is when the exchange of ions results in a modification of the environment chemistry at the crack tip, e.g. the pH value (Wiederhorn and Johnson, 1973). If then a more aggressive environment is formed, the crack propagation will thus be enhanced. The influence of ion exchange is thought to be pronounced also at low K_I values, where the then chemically modified environment can keep up with the crack tip.

Microplasticity: Besides the above mechanisms, the explanation for the *K-v* diagram with three regions have been tried by plastic flow theory in some studies (Marsh, 1964; Williams and Marshall, 1975), however the validity has not been supported by a number of studies on environmental effects during slow crack growth. It has even been further suggested that, even accepting the plastic flow, its influence should be negligible for most non-metallic materials at low temperatures such as the ambient ones (Martin and Durham, 1975; Dunning et al., 1980).

Moreover, if the mechanism is certain, this then allows predicting the effect of external/internal factors on SCG. In general, these factors include relative humidity, temperature, environmental chemistry (e.g. pH, corrosive species), microstructure of corresponding materials (e.g. degree of heterogeneity, microcracks), possible residual strain in the interior of materials, and maybe effective pressure as well. The relative humidity, temperature and environmental chemistry are the major factors for the most types of materials. They function as variables that influence the SCG behaviors and most

of them can also be adjusted in experiments. However, due to the complex effects incorporating different governing mechanisms, exact influences depend on specific mechanisms involved.

2.4.4. Kinetic models for subcritical crack growth

Many studies on the SCG have attempted to predict the rate of subcritical crack growth (Anderson and Grew, 1977; Atkinson, 1982). These prediction models are not definitively mechanism-specific. It has been show in metals, ceramics and geological materials that increase of temperatures lead to enhanced cracking if other parameters are kept the same. This is also consistent with the theoretical thought that cracking is thermally activated. At low temperatures this dependence is quite small, however at high temperatures (e.g. above 200 °C) the influence of temperature on SCG can be orders of magnitude higher (Evans and Wiederhorn, 1974).

Through studying glass, the most well-known power law equation to describe subcritical crack growth has been proposed as (Charles, 1958)

$$v = A\,exp(-H / RT)K_I^{\,n} \tag{2.9}$$

where v is the crack velocity, A is an empirical constant, H is the activation enthalpy, R is the gas constant, T is the absolute temperature, and n is a constant or the subcritical crack index for region I as mentioned before in Figure 2.7a. The Equation 2.9 is generally accepted for describing the behavior over all three regions (Atkinson, 1982). Another popular expression, which is only valid for describing SCG in region I, has been proposed through other studies as (Wiederhorn and Bolz, 1970)

$$v = B \, exp\{[(-Q + 2V^* \cdot K_I)/(\pi\rho)^{1/2}] / RT\} \qquad (2.10)$$

Q is the apparent activation energy, B is an experimentally determined constant, V^* is 'activation volume' and ρ is the curvature radius of the crack tip. The main difference is the energy term being expressed into two parts which include a mechanical contribution part and a chemical contribution part. The former is stress-independent while the latter with K_I is stress-dependent. The crack tip curvature is taken into account due to the crack sharpening effect (i.e. the decrease of curvature radius) during SCG from studies on glass (Wiederhorn and Bolz, 1970). Based on stress corrosion studies in metals, the SCG behavior in region II is given through energy consideration as (Vogt and Speidel, 1972)

$$v = C \, exp(-Q / RT) \qquad (2.11)$$

where C is a constant determined experimentally. This equation approximates the plateau of region II where the change of K_I has little influence on v. If following the argument that the SCG in region II is limited by diffusion of reactive species to the crack tip, the behavior can also be kinetically expressed as (Wiederhorn, 1967; Card et al., 2007)

$$v = mDC_0 / \delta \qquad (2.12)$$

where m is a constant dependent on bond configurations, D is the diffusivity of the mobile species, C_0 is the molar concentration of the mobile species, and δ is the effective distance through which the species need to travel to the tip. The thermally activated cracking process in region III is related to stress corrosion, however can be treated in an approximate way as fast crack growth mode as shown in Equation 2.5 or 2.6.

Other approaches attempting to approximate degrading effects include: considering the bond-breaking and bond-healing in terms of potential energy and surface energy (Stuart and Anderson, 1953); taking into account both tip curvature and crack length, through

kinetic and thermodynamic considerations (Charles and Hillig, 1962, Hillig, 2006), which was later modified in terms of K_I to have an identical form to Equation 2.10 (Wiederhorn and Bolz, 1970); or approaching the cracking by assuming that atoms evaporate from the crack tip and crack surfaces (Thomson and Fuller, 1974). Studies at this stage are largely empirical, with satisfactory understanding mainly for the behavior in region I.

2.4.5. Subcritical crack growth in cementitious materials

Concerning cementitious materials (mainly concrete, mortar and cement paste), little is understood about subcritical crack growth. No accurate measurement of subcritical crack growth velocities has been obtained or reported for cementitious materials (see Chapter 2.6.1). A few investigations were carried out, which were dedicated to slow (subcritical) crack growth in cement based materials (Nadeau et al., 1974; Mindess et al., 1974; Evans et al., 1976; Wecharatana and Shah, 1980; Beaudoin, 1985a and b). They all employed the double-torsion test (see Chapter 2.5.2) to study subcritical crack growth in hardened cement paste or mortar. The measured subcritical crack velocities ranging from μm/s to mm/s, many orders of magnitude slower than the mechanical crack velocities in cementitious materials, which may possibly be as high as 100's m/s (see Chapter 2.2.2). In these studies the *stress intensity factor* vs. *crack velocity* diagrams (or K_I-v plots) were obtained from force-relaxation tests at constant displacement. In none of these studies the calculated crack velocities were confirmed independently by other methods, especially through optical ways.

The susceptibility of hardened cement paste to subcritical crack growth was not found to vary much from glass: the subcritical crack index (*n*-value) of the log(K_I) – log(v) plot

is the same order of magnitude as that of glass in region I (Beaudoin, 1985b). However, the region II, characteristic of the K_I-v plots for many glasses (see Figure 2.7b), is much less pronounced in cement paste (Mindess et al., 1974; Wecharatana and Shah, 1980; Beaudoin, 1985a). The effect of relative humidity on subcritical crack growth in cementitious materials is more difficult to investigate than in glass, because cementitious materials are moisture-sensitive. Apart from the hydration process of cement, which leads to hardening of the material, many physical properties of fully hydrated materials depend on moisture content. Cementitious materials are porous and are internally wetted or dried upon a change of relative humidity in the environment. Wetting or drying causes shrinking and swelling of cementitious materials respectively, and this may affect subcritical crack growth if experiments are not well controlled. Early studies found that wet specimens are more susceptible to subcritical crack growth than dry specimens (Mindess et al., 1974). It was also showed that the stress intensity factor associated with subcritical crack growth does not increase continuously with relative humidity (Beaudoin, 1985a): in cement paste specimens, K_I generally increased to a maximum (at 11 or 32% RH) as humidity decreased. A decrease in K_I was then observed with the relative humidity approaching 0%. The effects of water-to-cement ratio and curing time, both determining the free water content in cementitious materials, on subcritical crack growth have been poorly investigated without consistent results (e.g. Mindess et al., 1974; Beaudoin, 1985a; Evans et al., 1976).

In glass and cement paste ,the similarity of subcritical crack growth in region I of the K_I-v plot (region II and III are usually not conspicuous in cement paste) and the similar dependence on relative humidity suggests that the mechanism(s) underlying subcritical

38

crack growth could be the same in both materials: stress-enhanced rupture of Si-O-Si bonds. The Si-O-Si bonds in the hydrated silicate structures of Portland cement could break more easily under stress in the presence of water (Shah, 1970; Husak et al., 1971; Krokosky, 1973; Barrick and Krokosky, 1976; Beaudoin, 1985a and 1985b). In a review of the '*influence of time on crack formation and failure of concrete*', Wittmann concluded that 'there is no direct evidence of stress corrosion in cementitious materials', and that 'further research is needed to clarify the role of chemical stress corrosion in the context of subcritical crack growth' (Wittmann, 1985). However, the existence of stress corrosion in concrete in the presence of very corrosive agents like ammonium sulfate (Werner et al, 2000) and ammonium nitrate (Schneider and Chen, 2005) has been shown. Studies also suggest that creep, possibly involving the internal redistribution of capillary water, may be one of the mechanisms involved in subcritical crack growth (Nadeau et al., 1974).

Microstructures are also expected to be important. Its influence is manifested mainly through the nonlinear microcrack zone around a crack tip. The microstructures that produce a denser microcrack zone can facilitate major crack initiation and propagation, thus enhance the SCG (Wu et al., 1981). Multiple crack formation, branching and deviation tend to weaken the SCG at crack tip because they can absorb part of the energy that is needed for subcritical cracking. Cementitious materials are brittle disordered composite materials with a significant amount of micro defects, and cracks propagate through different phases and interfaces. The subcritical crack velocities (and, possibly, the underlying mechanisms as well) may vary for different phases and interfaces.

2.5. Measurement of subcritical crack growth

2.5.1. Existing test methods

The subcritical crack growth in a material is characterized by the typical stress intensity factor (K) versus crack velocity (v) diagram, and the parameters extracted can be used to perform lifetime prediction and to investigate how the environment influences subcritical cracking. The major methods allowing determination of K-v diagrams for SCG are presented in Figure 2.10, and they are:

(1) Double-torsion method (Evans, 1972);
(2) Double-cantilever beam method (Freiman et al., 1973);
(3) Double-cleavage drilled-compression method (Janssen, 1974; Fett et al., 2009).
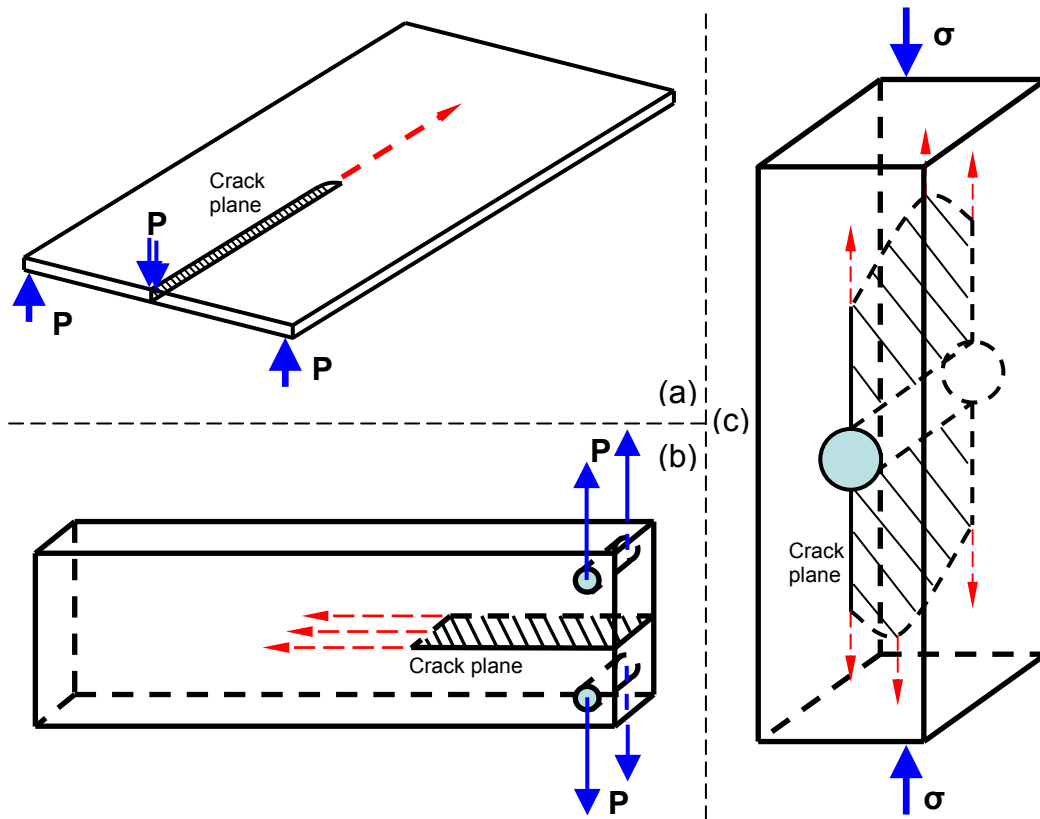
Figure 2.10. Schematic illustration of major experimental methods for subcritical crack growth: (a) double-torsion method; (b) double-cantilever beam method; (c) double-cleavage drilled-compression method.

The double-torsion (DT) method is the most commonly used testing tool to study slow SCG in a wide of range of brittle or quasi-brittle materials (Shyam and Lara-Curzio, 2006). It is characterized by a rectangular plate-shaped specimen being loaded in a 3 or 4 point-bending manner at one side (as shown in Figure 2.10a). A particular feature of the DT method is that along with a propagating crack, the K at the moving crack tip is independent of the crack length (Evans, 1972). Thus the time and force can be recorded for directly calculating corresponding K and v values without the necessity to track the crack evolution. This feature renders the DT method convenient for studies on opaque materials or in harsh environments where direct access to observing crack propagation is difficult (Tait et al, 1987). The DT method is employed in this study, and it will be discussed in detail later.

The double-cantilever beam (DCB) method is employed mainly to obtain fracture parameters such as critical stress intensity factor or energy release rate for brittle materials (Freiman et al., 1973). It is characterized by a beam-shaped specimen being loaded in pure Mode I by a moment at one end, and this end is already pre-split into two cantilever beams (as shown in Figure 2.10b). The crack travels in the common plane of these two beams and its front shape is symmetrical. However, the K at the crack tip is dependent on the crack length and increases with the crack extension, thus the cracking quickly becomes unstable (Gonzalez and Pantano, 1990). Modification to this problem will then lead to complex specimen geometry which is not so easy for machining. To obtain the crack velocity data, optical access to the crack tip is needed.

The double-cleavage drilled-compression (DCDC) method is aimed at studying slow facture behavior of monolithic brittle materials or bi-materials (He et al., 1995), mainly of glasses. It uses a rectangular bar-shaped specimen with a circular hole in the center, and is loaded in compression along its length (as shown in Figure 2.10c). Its major advantages are the crack stability due to compression, self-precracking under load, pure mode I fracture at crack tip and able to provide interfacial fracture energy measurements (He et al., 1995). Moreover, crack propagation needs to be tracked optically to provide the data for v determination.

2.5.2. Principles of double-torsion method

The DT theory originates from the experimental analysis of the compliance relationship for double-torsion load-displacement relationship at the loading points for a specimen as shown in Figure 2.10a, as (Shyam and Lara-Curzio, 2006)

$$\lambda = \Delta / P = aJ + \lambda_0 \tag{2.13}$$

where λ is the compliance, Δ is the load-point displacement, P is the force, a is the crack length, J and λ_0 are parameters dependent on the material's elastic properties and geometry. This linear relationship is valid for most crack length, except the regions where crack length is very short or very long. With the help of Equation 2.13 and by assuming that the crack extension is equal to crack-surface-area change rate (Fuller, 1979), the strain energy release rate for DT configuration can be then expressed as

$$G = \frac{P^2 J}{2d_w} \tag{2.14}$$

42

G is the strain energy release rate, and d_w is the thickness of the cracked part (if a guide groove along the crack path exists). G can also be expressed, in terms of stress intensity factor K_I and shear modulus S, as

$$K_I = \sqrt{2SG /(1 \mp \mu)^{\pm 1}} \tag{2.15}$$

where the plus or minus sign ($\pm$) refers to plane strain or plane stress condition respectively. The plane strain condition is more favored in earlier studies, while the plane stress condition is favored in later studies because of the thin-plate shape of DT specimens (Shyam and Lara-Curzio, 2006, Ciccotti et al., 2000). Here, using the Mode I configuration is supported by studies on DT method (Evans, 1972; Williams and Evans, 1973). Then by combining Equation 2.14 and 2.15, it can be obtained that

$$K_I = P\sqrt{\frac{SJ}{(1 \mp \mu)^{\pm 1} d_w}} \tag{2.16}$$

The analytical expression of compliance is given on the basis of analyzing the torsion of rectangular beams and has the form of (Williams and Evans, 1973)

$$\lambda = [3w_m{}^2 / SWd_t{}^3 \psi(z)]a \tag{2.17}$$

$$\psi(z) = 1 - 0.6302z + 1.20z \, exp(-\pi / z) \tag{2.18}$$

where w_m is the moment arm for the load applied, W is the specimen width, d_t is the total specimen thickness, ψ is a correction function to take into account the finite thickness and z is the thinness ratio defined as $z = 2d/W$. Therefore, by combining Equation 2.13, 2.16 and 2.17, the K_I is

$$K_I = Pw_m\sqrt{\frac{3S}{(1 \mp \mu)^{\pm 1} d_w d_t{}^3 SW\psi(z)}} \tag{2.19}$$

On the other hand, with the help of Equation 2.13, when the load-point displacement is constant, the crack velocity can be written as

$$v = \left(\frac{da}{dt} \right)_{\Delta} = -\frac{Ja + \lambda_0}{JP} \left(\frac{dP}{dt} \right)_{\Delta}$$

(2.20)

where t denotes time. Since Equation 2.13 is valid over the full range of crack length, together with constant Δ, thus

$$(J \cdot a + \lambda_0)P = (J \cdot a_i + \lambda_0)P_i = (J \cdot a_f + \lambda_0)P_f$$

(2.21)

the subscript i and f represent the corresponding values at initial or final stage respectively. Substituting Equation 2.21 into 2.20 and considering the most likely situations that $\lambda_0/J << a_i$ which is based on compliance studies (Williams and Evans, 1973), the final expression of velocity can be obtained as

$$v = -\frac{P_i a_i}{P^2} \left(\frac{dP}{dt} \right)_{\Delta} = -\frac{P_f a_f}{P^2} \left(\frac{dP}{dt} \right)_{\Delta}$$

(2.22)

Therefore, the K-v relationship can be extracted from the DT method for the case of constant displacement at the load points. Following the same principle, other possible mathematical treatments keep the displacement rate ($d\Delta/dt$) constant or keep P constant to derive the respective v.

2.5.3. Double-torsion testing modes

As suggested by the analytical derivation (Fuller, 1979), there are three possible conditions to obtain a simple expression for crack velocity, and these lead to three testing modes for crack propagation studies (as shown in Figure 2.11):

44
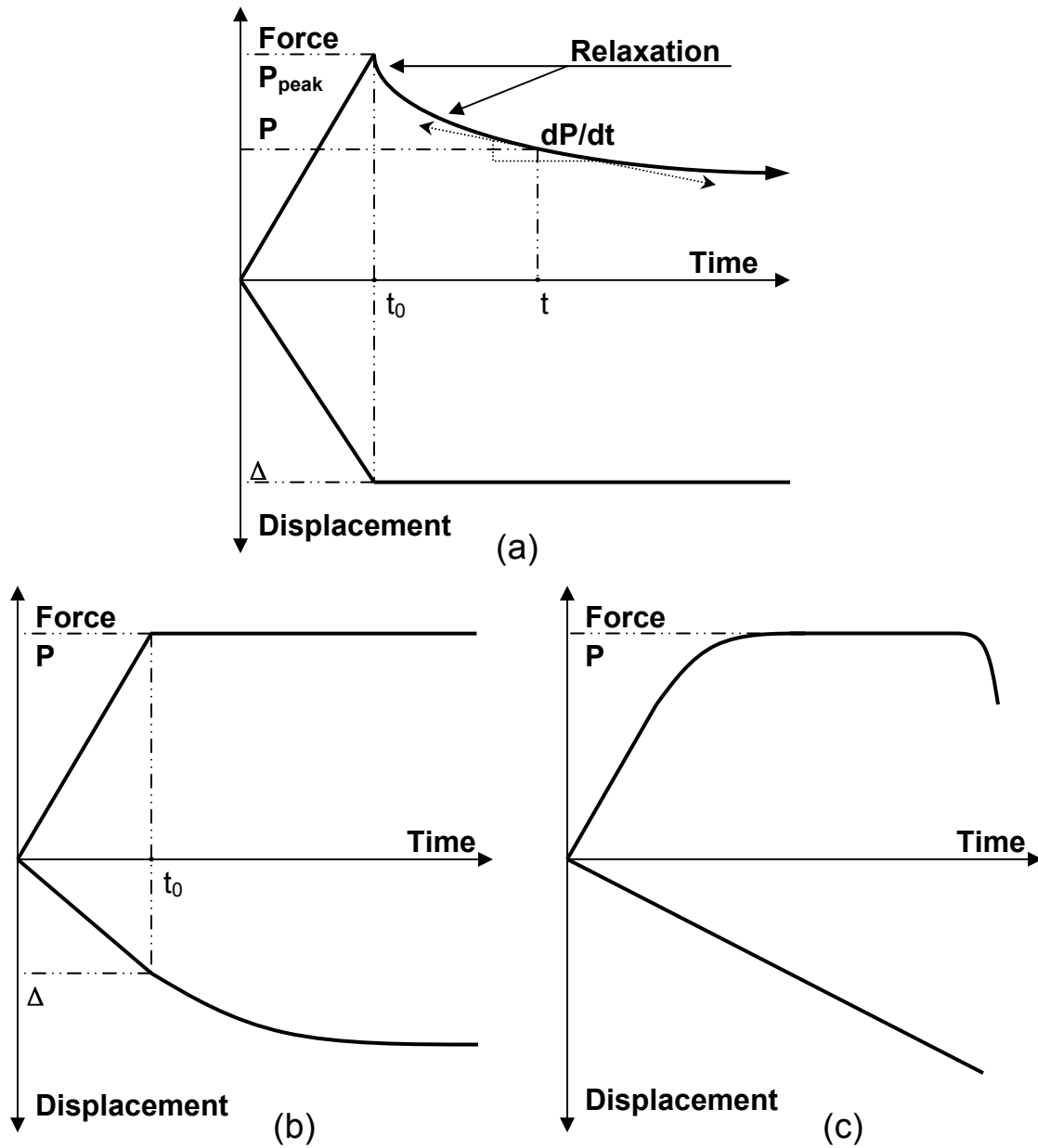
Figure 2.11. Schematic illustration of typical force-time and displacement-time curves for: (a) constant displacement test; (b) constant load test; (c) constant displacement rate test (Pletka et al, 1979).

(1) Constant displacement test, which keeps the position of load points constant, as shown in Figure 2.11a. The starting load at the loading points is below the fracture load, of around 90%. With the recorded force and time data, the K-v diagram can then be generated through Equation 2.19 and 2.22. A complete K-v curve can be obtained from a

single experiment (Pletka et al, 1979). While, this test is suitable for relatively higher range of crack velocities (e.g. $> 10^{-7}$ m/s) and erroneous effects from testing devices should be considered with caution (Virkar and Gordon, 1975). This testing mode is the mostly used one in SCG studies.

(2) Constant load test, which keeps the load at the load-points constant, as shown in Figure 2.11b. The load is also below the critical fracture point. This test mode is suitable for extremely low velocities (e.g. $< 10^{-7}$ m/s), however each test can produce just one data point for the *K-v* curve as only an average crack velocity can be obtained (Shyam and Lara-Curzio, 2006). Thus in order to make a curve complete a significant number of tests is needed, which can be time-consuming. The mode is mainly complementary to the constant displacement test.

(3) Constant displacement rate test, in which the load-points moves at constant displacing rate each time until failure of each specimen and this rate changes incrementally, as shown in Figure 2.11c. This testing mode can produce crack velocities at very low values but only one data point can generated each time, thus it is also a complementary one to the constant displacement test especially at high temperatures (Evans, 1972).

2.5.4. Double-torsion specimen geometry

One of the typical specimen geometries is presented in Figure 2.12. A subcritical crack is supposed to initiate at the notch tip and run in the middle of the specimen. Due to the assumption of a thin plate, the DT specimen needs to follow the geometry requirement of $12d_t \leq W \leq L/2$ and a *W/L* ratio between 1/2 and 1/3 is suitable (Pletka, 1979; Tait et al.,

46

1987), with d_t, W, L being shown in Figure 2.12. The K_I is expected to be independent of the crack length, while finite element studies have shown that this independence only holds for a certain range along crack length due to nonlinear end effects (Trantina, 1977). Accordingly, a crack is in this effective range when the crack length satisfies: $0.5W < a < L$-$0.65W$, with a being the crack length. For cementitious materials, the size of the process zone was considered to depend on the size of possible inclusions (e.g. sands, aggregates), and therefore the uncracked part of the specimen should be much larger than the inclusions (Wecharatana and Shah, 1980). It was also suggested that L be no less than the magnitude of 10 mm for cement paste and 100 mm for mortar and concrete, by taking into the account the fact that the bending moment is distributed along the centerline rather than concentrated around the crack tip (Hillerborg, 1983).
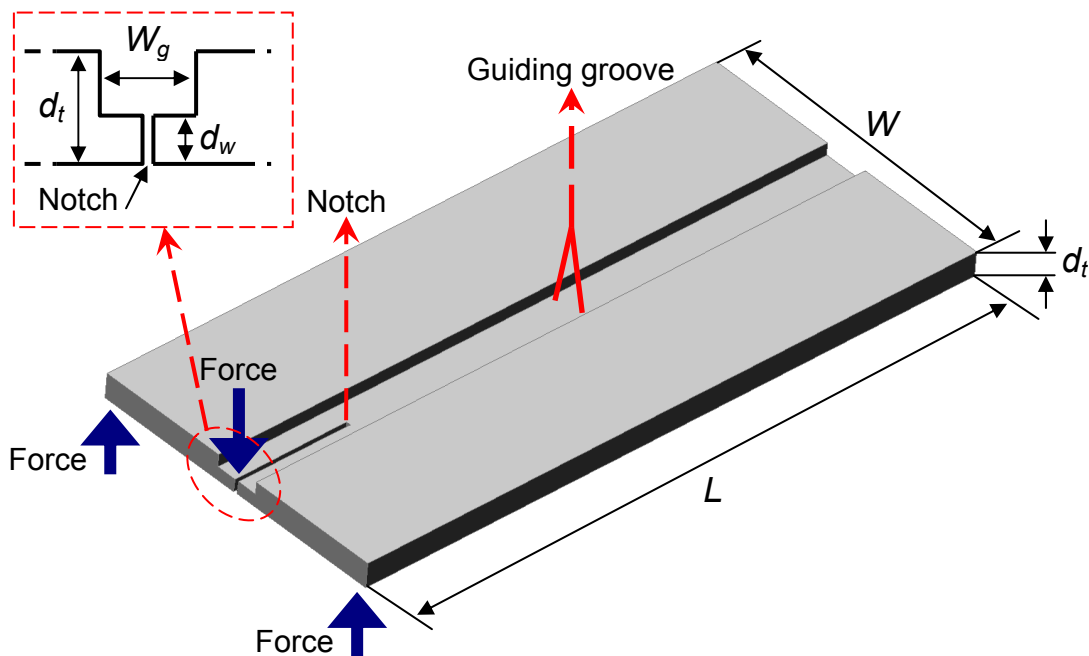
Figure 2.12. A general schematic drawing of the specimen in the double-torsion test.

A guide groove is normally cut in one surface to ensure the crack propagation is along the central line and down to the end, especially for the materials with severe crack path deviation. But double-side narrow grooves should be avoided due to high data scatter (Pletka, 1979). A relatively wide rectangular guide groove can provide higher data reproducibility than V-shape and semicircular-shape guide grooves for heterogeneous materials like rocks, although specimens with no grooves are preferred if possible (Nara and Kaneko, 2005). Furthermore, a tapered notch at one end of a DT specimen can also be machined to help facilitate crack initiation at loads below the critical fracture load (Shyam and Lara-Curzio, 2006), and it has to be as narrow as possible. For a propagating crack during DT test for brittle materials the crack front is known to be inclined (Evans, 1972), and the crack front is illustrated in Figure 2.13.
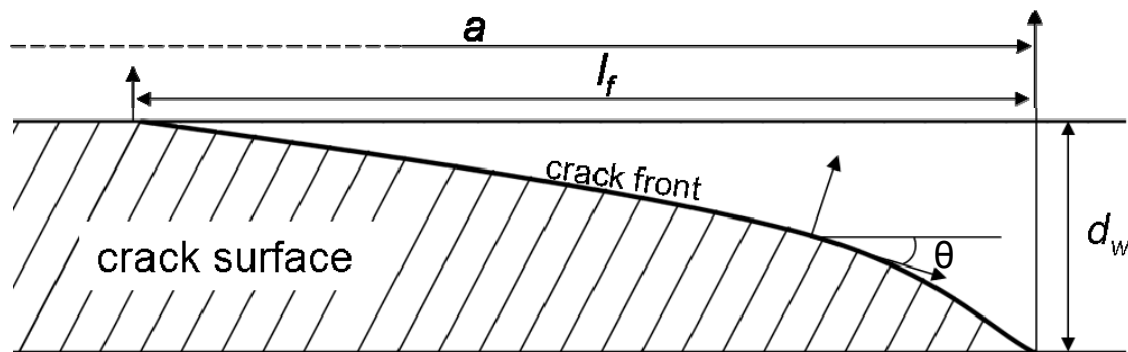
Figure 2.13. Schematic illustration of a typical crack front profile of a DT specimen. a denotes the crack length at the tension side, d_w is the thickness of the cracked part, l_f is the length difference of upper surface crack and lower surface crack and θ is the inclined angle at specific point on the font.

The degree of inclination depends on the characteristics of SCG in specific material and surrounding environment, but is independent of the crack length (Virkar and Gordon, 1975). The crack velocity on the tension-side of the surface is usually not exactly the same as the overall velocity, due to the inclination. Such influence on the overall crack

48

velocity can be corrected by introducing a correction factor $\Phi = d_w / (l_f^2 + d_w{}^2)^{1/2}$ (Evans, 1972), and if the d_w is much larger compared to l_f, this influence can be neglected.

CHAPTER 3 Materials and Methods

3.1. Materials

3.1.1. Cement

Ordinary Portland Cement of the type CEM I 52.5R (Holcim Normo 5R) was used for all cement specimens in this study. The cement was sieved (< 63μm) before use to remove the larger particles or agglomerates of cement particles. The major constituents are listed in Table 3.1 and the corresponding Bogue composition is listed in Table 3.2. The cement was stored in sealed condition, avoiding contact with surrounding moisture.

Table 3.1. Chemical composition of the cement used in terms of common oxides, according to Holcim (Rieger, 2011).

Oxide Component	Weight Fraction (%)
CaO	61.5
SiO_2	19.8
Al_2O_3	4.9
Fe_2O_3	3.3
MgO	2.1
K_2O	0.8
Na_2O	0.3
Others	7.3

Table 3.2. Bogue composition of the cement (calculated according to Taylor, 1989).

Chemical Compound	Weight Fraction (%)
Tricalcium silicate-C_3S	62.2
Dicalcium silicate-C_2S	10.2
Tricalcium aluminate-C_3A	7.4
Tetracalcium aluminoferrite-C_4AF	10

3.1.2. Specimen preparation

The specimens in this study were prepared from cement pastes with w/c-ratios of 0.3, 0.4, 0.5, 0.6 and 0.7. No admixtures were used in this study. An electric vibrator and a combination of sieves (250 μm, 125 μm and 63 μm) were used to obtain dry cement with particle sizes smaller than 63 μm. The cement pastes were stirred for 5 min in a Hobart mixer at intermediate speed, and then stirred for another 5 min by using a mixing beater attached to a drilling machine at high speed. Possible introduction of air voids was minimized by carefully moving the drill in the pastes. The ready-pastes were poured into brass moulds of 65 mm × 25 mm × 10 mm (length × width × height) size to cast DT specimens. The moulds are as shown in Figure 3.1 and they were oiled thinly beforehand to facilitate demoulding later. A brass piece with an inverted T-shaped cross-section was fixed inside each mould to help form a 1 mm wide × 3 mm deep guiding groove in the middle of each specimen (Figure 3.1). The moulds with pastes were vibrated mildly on a table vibrator for around 5 min to exclude large internal air voids. The moulds were then sealed with plastic foil and stored in a conditioning room at 95% relatively humidity (RH) at 20 °C for hardening. After about 24 hours the specimens were carefully removed from the moulds and placed in saturated lime water for 8-9 months of curing.
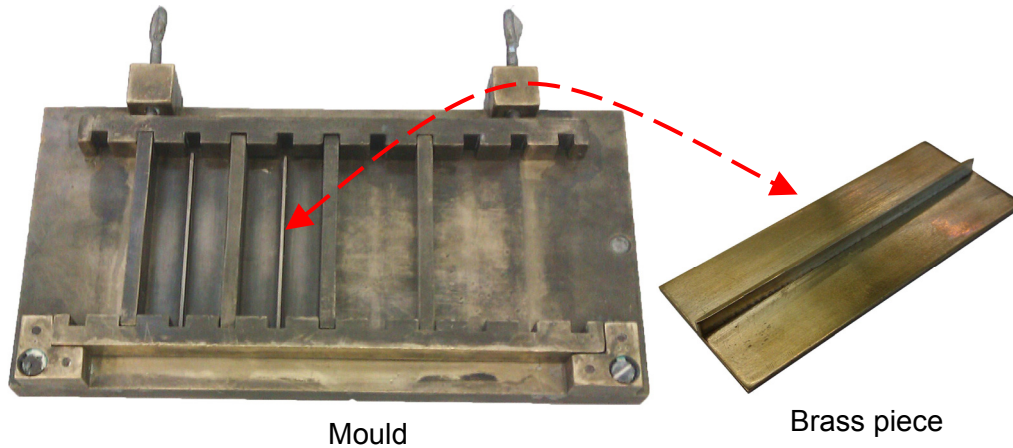
Figure 3.1. Picture of the brass mould for preparing DT specimens and the brass piece with an inverted T-shaped cross-section to add guiding grooves.

Cured specimens were coarsely ground on grit-120 sand paper and then finely ground on grit-1000 sand paper to the size of 60 mm × 25 mm × 1.7 mm (length × width × thickness) for DT tests. Selecting this size value, the specimens could fit the micro-testing device and need minimum treatment (i.e. cutting, grinding or so), while still satisfying the dimensional requirement (see Chapter 2.3.4). Before thinning, a 10 mm × 0.45 mm (length × width) notch was cut, at a low advancing speed of 0.1 mm/s and wheel rotation speed of 3000 rpm by a precision diamond saw (Struers Accutom-5), in one end of each specimen to avoid introducing cracks during cutting. The real specimen is as shown in Figure 3.2.
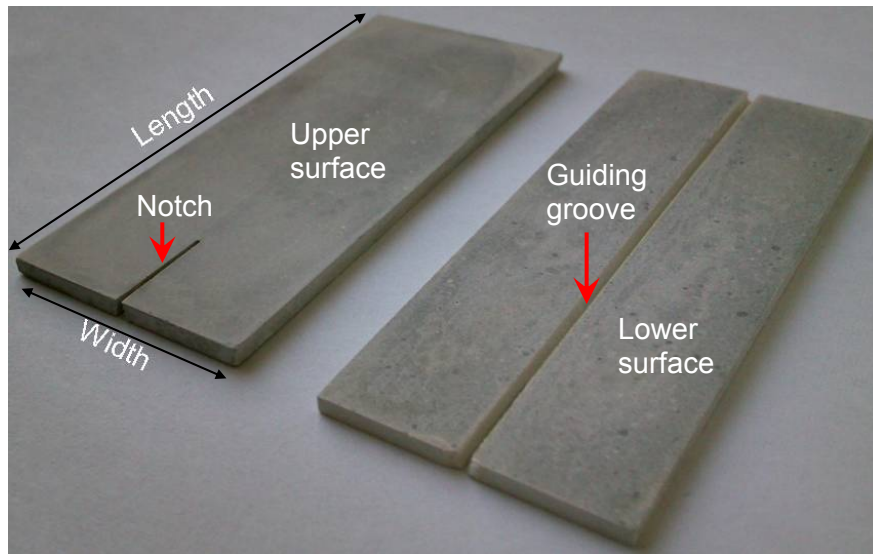
Figure 3.2. The picture of ready-for-test DT specimen showing both the upper and lower surfaces.

The thickness of each specimen was kept below 2 mm to avoid desiccation cracking that otherwise may occur upon equilibrating or testing the specimens at low relative humidity (Bažant and Raftshol, 1982; Bisschop and Wittel, 2011). Before each DT specimen was tested, a tapered pre-crack was cut by a razor blade at the notch tip to facilitate crack initiation (Tait et al., 1987). Extreme care was taken for introducing these artificial cracks in specimens to ensure that no side damage would occur. Example of specimens with poorly-cut and finely-cut notch tip are presented in Figure 3.3. All specimens were checked by microscopes and only those without side cracks at the notch tip were used for tests. Additional specimens were left without this pre-crack for identical creep-induced relaxation tests. Constant-displacement tests were performed on each of these specimens that were without pre-existing cracks. At certain load levels there were no major cracks being initiated and the corresponding force relaxation can then reflect creeping of the specimen. Additional unnotched specimens of the size of 28 mm × 4 mm

× 2 mm (length × width × thickness) were prepared for beam-bending tests using the DT set-up to measure creep-induced relaxation of the cement pastes.
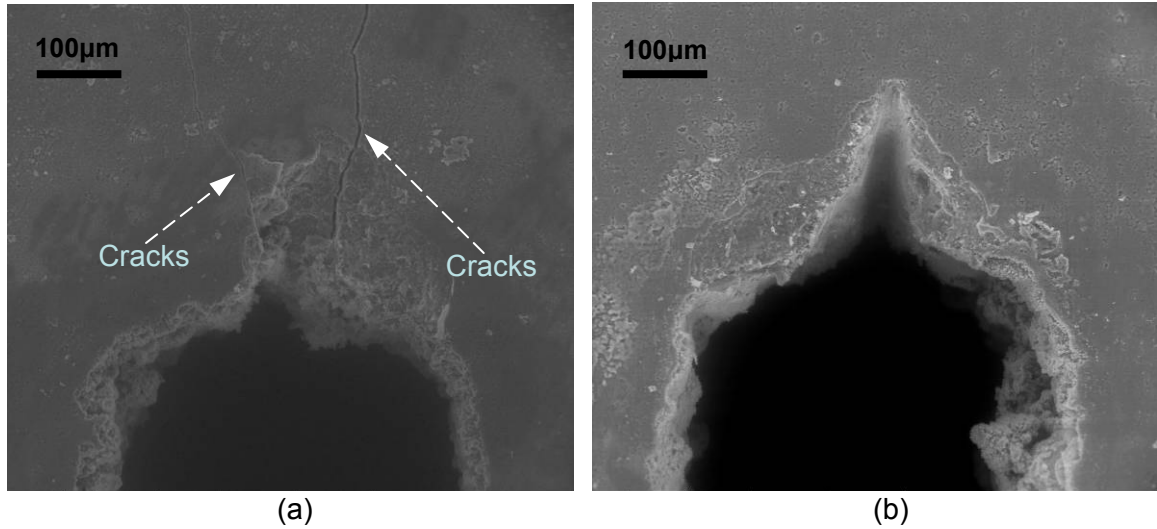
Figure 3.3. Top view of ESEM pictures for the notch tip: (a) poorly machined notch tip with cracks introduced by notch cutting, (b) finely machined notch tip with razor blade cut.

3.1.3. Pre-conditioning

DT-tests were performed inside the ESEM at controlled relative humidity and temperature, or under the optical microscope in a conditioning room for cement paste specimens. For dry-condition tests, before being tested each cement paste specimen was equilibrated at the RH of 65% in conditioning room for 3 days, and then at the same RH (i.e. 10%) and temperature as during the DT-test in a climate chamber (Vötsch VC4060) for about 4 more days until the weight stabilized. This step-by-step equilibration with gradually lowering of relative humidity helped to prevent desiccation cracks in the specimens. Images of specimen surface showing desiccation cracks (i.e. poorly equilibrated) and absense of desiccation cracks (i.e. properly equilibrated) are presented

54

in Figure 3.4. For wet-condition tests, each specimen was equilibrated directly in conditioning rooms at corresponding RH and temperature, until the weight stabilized (normally within 3 days). The age of the DT specimens at the time of testing varied between 8 and 9 months (cured in limewater). It was assumed that variations in age between 8 and 9 months had little influence over the fracture behavior of cementitious materials. The carbonation at specimen surface during the equilibration period was also expected to have negligible effect over the fracture behavior of the bulk of each specimen. 1% solution of Phenolphthalien in ethanol was sprayed onto fresh fractured specimen surfaces and no significant carbonation was observed.

(a)   (b)
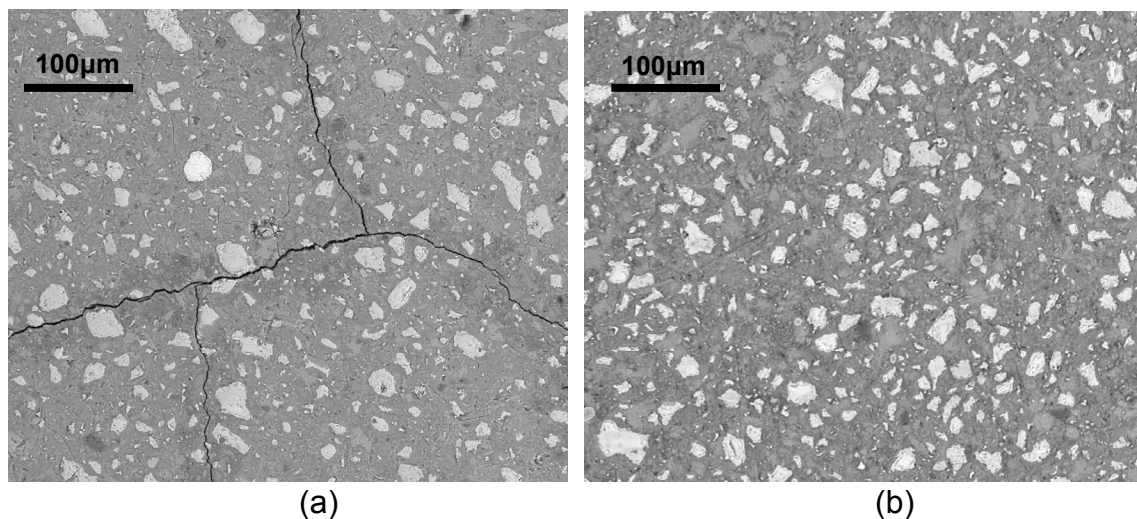
Figure 3.4. ESEM images showing cement paste specimens (a) with desiccation cracks due to improper control of equilibration (e.g. fast drying), and (b) without desiccation cracks. The specimens were cured for the same time, with w/c ratio of 0.3.

Some DT specimens were used to perform fracture toughness tests that were suggested by previous studies (Shyam and Lara-Curzio, 2006; Salem et al., 2008). Some other DT specimens with cracks extended into their middle part were preserved in the saturated

limewater for studying healing effects. Specific testing set-up and specimen parameters will be described in later sections.

3.1.4. Degree of hydration

The degrees of hydration of the cement pate specimens were estimated at the age of 9 months after the DT tests. This is important because many mechanical properties of cement paste are related to the degree of hydration (e.g. strength development, fracture toughness). The estimation was conducted by pixel-counting on BSE images and corresponding binary images (Feng et al., 2004). An example is shown in Figure 3.5. Each specimen was equilibrated at 10% RH for 3 days. Then the surface layer (about 0.5 mm) of the specimen was removed by grinding. Ethanol was used as coolant during grinding. The BSE images (e.g. Figure 3.5a) of the specimens were taken in ESEM at the water vapor pressure of 1 torr and at a temperature of 20 °C. Each BSE image was transformed into corresponding black and white image (Figure 3.5b). The numbers of black pixels (n_1) and white pixels (n_2) were counted through Matlab. They were then used to estimate the degree of hydration (α_{cem}) through the following relationship (according to Feng et al., 2004):

$$\alpha_{cem} = 1 - n_2 /(n_2 + \frac{n_1 \rho_w}{r_{wc} \rho_c + \rho_w})$$

(3.1)

where ρ_w and ρ_c are the densities (g/mm^3) of water and cement respectively, r_{wc} is the w/c-ratio of the specimen. The porosity of the imaging areas was assumed to be less 1%

56

so that it was not taken into account in the calculations. The estimations of the degree of

hydration for the cured specimens are listed in Table 3.3.

(a) BSE image   (b) Binary image
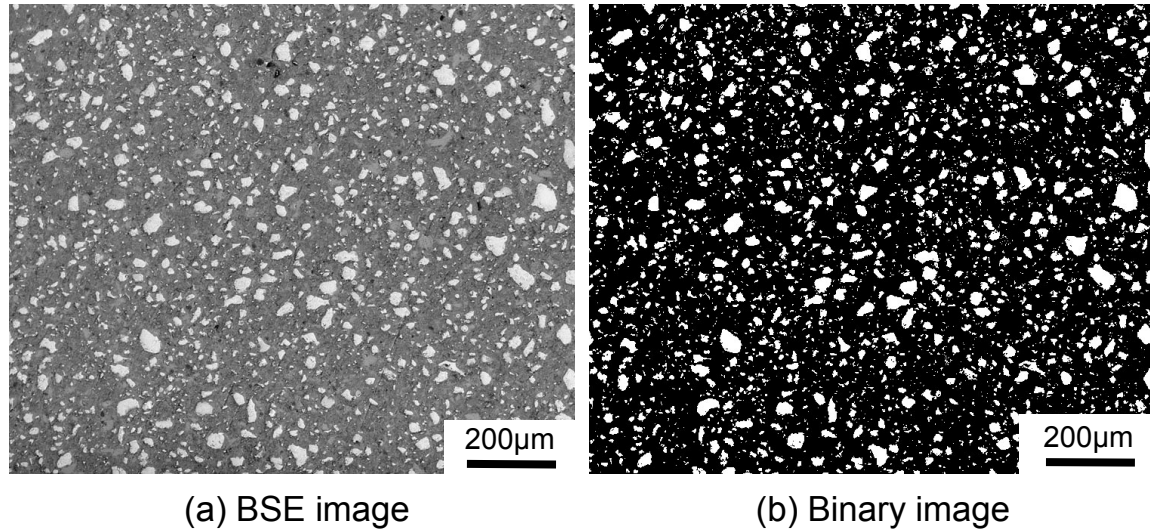
Figure 3.5. Example of the images for estimating the degree of hydration of DT
specimens, with w/c ratio of 0.3. (a) the original BSE image; (b) the
corresponding binary image.

Table 3.3. The degree of hydration of DT specimens at the age of 9 months.

w/c ratio	0.3	0.5	0.6	0.7
α_{cem}	75.9±1.5%	87.6±1.4%	90.2±2%	94.6±2.3%

3.2. Methods

3.2.1. Double-torsion testing device

To study the subcritical crack growth (SCG) in hardened cement paste, the double-

torsion (DT) method was adopted in this research. The main advantage of the DT method

is that during subcritical cracking the stress intensity factor at the crack tip is independent

57

of the crack length in the center region of the DT specimen (Williams and Evans, 1973). Also, both the specimen geometry and the loading configuration are relatively simple and easy to be adopted for subcritical cracking studies (see Figure 2.10). Also, as previously mentioned in Chapter 2.3, DT method is more convenient than other available methods for optically tracking crack propagation, especially for opaque materials where high-magnification observation is needed to identify the position of the crack tip.

Previous studies, on cementitious materials through direction observation of fracturing of specimens inside SEM, showed the capability for imaging crack paths (Mindess and Diamond, 1980; Mindess and Diamond, 1981; Mindess and Diamond, 1982). However, the specimens suffered from severe drying cracks due to the high vacuum of the SEM chamber. "Wet cell" was later employed to avoid drying cracks (Diamond et al., 1983). However, no successful crack-velocity measurements were reported. *In-situ* studies using a developed DT-testing device were performed in SEM for studying SCG in brittle materials (Tait et al., 1986; Tait and Garrett, 1986), but no results that were capable of deriving the *K-v* diagrams were reported.

In this study, a micro-mechanical testing device was designed and constructed to carry out DT tests. The basic characteristics of this device were: (i) performing DT tests with high accuracy inside the vacuum chamber of the ESEM; (i) allowing optical access (directly or via electron scanning) to the specimen surface in order to monitor the crack propagation; (iii) withstanding humid conditions while running. The mainframe of the device was constructed by stainless steel and special protections were also implemented for other key components (e.g. force cell, displacement transducer), to resist corrosion in humid environment. The size and weight of the whole device were kept as small as

possible to be placed on the specimen stage in the ESEM. While a high degree of movement was still allowed during ongoing tests. The DT tests can be controlled from outside the ESEM chamber and necessary data (force, displacement and etc.) can be recorded in real time.

This micro-testing device consists of the following key components: a mechanical-loading stage, a Peltier cooling stage with temperature sensors, a computer-assisted control unit and a data-acquisition unit. A general view of the loading device with the cooling stage is presented in Figure 3.6.
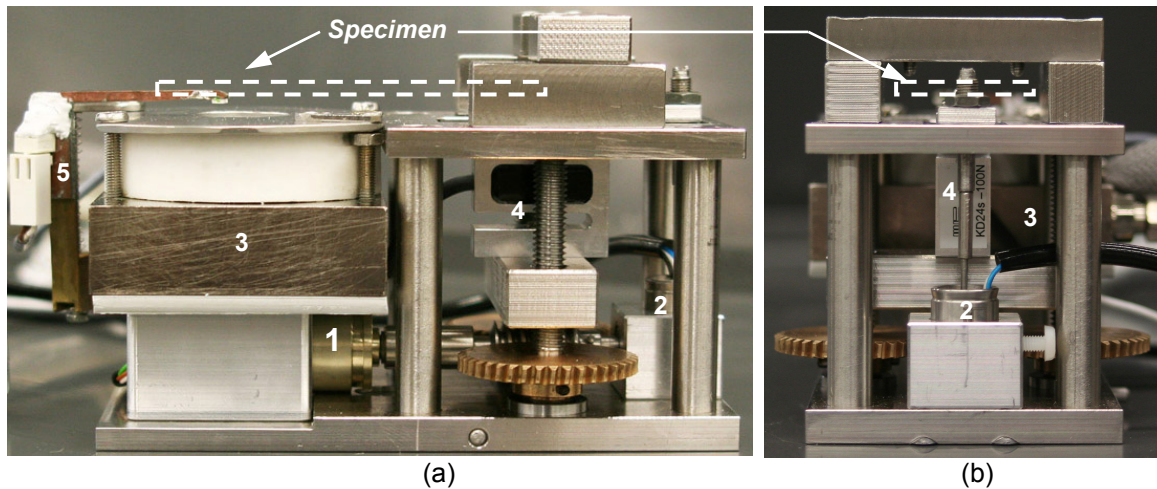
Figure 3.6. Double-torsion testing-device pictures from (a) side view and (b) front view. 1 denotes the stepper motor with the gearhead, 2 is the LVDT, 3 is the cooling stage, 4 is the force cell and 5 is the temperature sensor.

The mechanical-loading stage consists of a PRECI*step* two-phase stepper motor mounted with a zero-backlash spur gearhead (1/900 reduction ratio), a Transmetra force sensor (accuracy of ±0.1 %), an HBM linear-variable displacement transducer (LVDT, accuracy of ±2 μm) and a high-precision micro-transmission system used to integrate these components. This loading stage was devised specifically for DT tests inside the

59

vacuum chamber of Quanta-600 ESEM. Attention was also paid to avoid possible harmful effects such as mechanical abrasion, heat generation and electric short circuit of key parts.

The Peltier cooling stage enables fast and accurate temperature control of the specimen under vacuum conditions through heat conduction. An aluminum table (not shown in Figure 3.6) is connected to the cooling stage and DT specimens can be placed on the table. In vacuum, poor contact between the specimen and the aluminum table could lead to poor heat transfer. Therefore silicone grease was used to improve the contact between them without introducing significant external forces on the specimen, causing erroneous influences. This grease was used to improve the heat conduction between the aluminum table and the cooling stage. Two temperature sensors are attached to the set-up: one inside the cooling stage measuring the core temperature and one placed on the upper surface of the specimen measuring the specimen temperature. Through adjusting the core temperature from the external control panel, the desired temperature could be obtained for the specimen.

The computer-assisted control unit manages the following functions: (i) the calibration of the force cell and the LVDT; (ii) the up and down movement of crosshead at the loading point through rotary motion of the stepper motor; (iii) the control of specimen temperature by the cooling stage. A program with graphical user interface coded by Labview helped to control the rotation of the motor, display and record the data. The data acquisition unit is responsible for collecting all data (load force, displacement of crosshead vs. time) at a rate of one data point per second from the LVDT and the load cell, through the amplifier (DMC*plus*, HBM). The analog signals are converted into

60

digital signals for computer processing, by A/D converters. A special connector was mounted on the ESEM to allow cables from the in-chamber testing device to be connected to external instruments. This set-up can also be used at ambient conditions under an optical microscope. The relaxation of the loading device was examined by using stiff specimens (i.e. brass) and was lower than 0.5% under relatively low loads (i.e. below 20N) applied in this study. The relaxation lied within the error range of the load cell ($\pm$0.1 N). To minimize this effect on the total measured data, two solutions were used. Either the loading device was relaxed before each DT-test series or the erroneous relaxation was measured first and then used for subtraction from the total relaxation measurement. A schematic diagram showing the experimental set-up is shown in Figure 3.7.
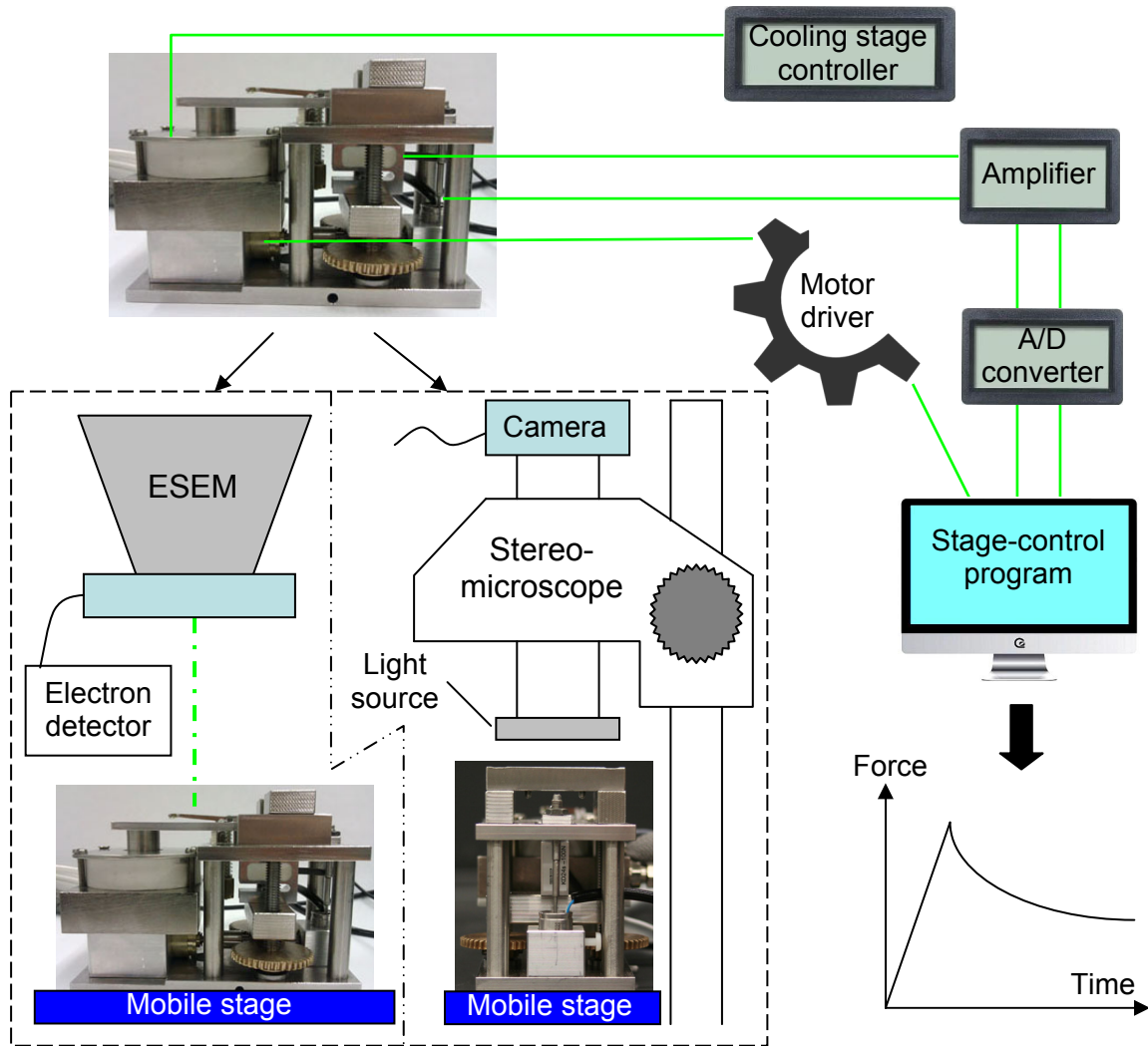
Figure 3.7. Schematic illustration of the control chart for the DT-testing device operating inside the ESEM or under stereomicroscope.

3.2.2. Double-torsion testing protocols

In this study, the constant-displacement test was adopted as the main test mode, due to its capability of extracting the complete curve of stress intensity factor (K) versus crack velocity (v) in a single test. The whole process proceeded as following: The specimen was placed on the loading stage and equilibrated at the same relative humidity and temperature as of the scheduled test. The equilibration time depended on the dimension

and microstructure properties of the specimen. Then it was loaded at a speed of approximately 1.5 μm/min till an initial rapid crack growth originating from the tapered notch tip occurred at the peak force. This peak value was below the critical failure value so that the catastrophic fracture wouldn't occur and the crack growth could be managed by the change of the applied force. The crack was then guided to propagate step by step and the loading points were arrested immediately after the crack rapidly propagated into the effective working range, within which the stress intensity factor at the crack tip is independent of the crack length. The range used for cement paste specimens in this study was: 13 mm ≤ crack length ≤ 42 mm for the specimens with a length of 60 mm and width of 25 mm (refer to Chapter 2.3.4). The loading points were held stationary (i.e. LVDT readings varied within ±0.5μm) and the force relaxation was recorded for about 30 minutes during which the crack propagation was around tens to hundreds of micrometers. Up to three constant-displacement tests could be performed on one specimen.

The following equations as for calculating SCG in brittle or quasi-brittle materials by DT constant-displacement tests were adopted:

$$v = -a_f (P_f P^2)(dP / dt)$$
(3.2)

$$K = PS_m [3(1 + \mu) / d_w d_t^3 W \psi]^{1/2}$$
(3.3)

notations here are the same as those in Equations 2.19 and 2.22. Measurement of final crack length a_f was done by optical observation via microscopes. Values of the instantaneous force P and final force P_f were obtained from data recorded by the force cell. Plane-stress assumption was employed as the precondition for calculating stress intensity factor in this study according to the geometry configuration of the DT specimens, which have their shapes as thin plates. During each test, environmental

conditions were all kept constant. These equations are based on the presumption that the mechanical behavior of the specimen is linear elastic. Thus for materials that can behave nonlinearly (e.g. creep) under applied forces, the calculated velocities are not accurate. Other methods capable of justifying the real crack velocities are necessary for studying SCG in quasi-brittle materials.

3.3. Image acquisition and analysis

3.3.1. Environmental scanning electron microscopy

The ESEM was employed to observe the subcritical crack behavior since it is able to provide high-magnification optical access to the crack tip. Also, it allows the presence of water vapor inside the vacuum chamber. This is especially important for hydrated specimens that undergo severe damages (e.g. surface microcracking due to desiccation) in dry conditions (Neubauer and Jennings, 1996). The water content inside the chamber is controlled by changing the water vapor pressure through the ESEM. If the water content in the chamber is too high, the image resolution is then decreased by the interactions between water molecules and electrons. In this study, the ESEM can produce images of good resolution with the vapor pressure below 5 torr and relative humidity below 50%. Water vapor pressure and temperature determine the corresponding relative humidity. The relationship among them was proposed by previous studies (e.g. Buck, 1996). With the ESEM and cooling stage, it is possible to perform DT tests under controlled relative humidity in vacuum conditions. In a normal SEM, the charging problem during imaging often occurs for non-metallic materials due to their electrically non-conductive properties. Accumulation of excess electrons could deflect the electron beam from ideal paths and

produce distorted images. This can be circumvented in ESEM under wet mode since the generation of positively-ionized water-vapor molecules help to neutralize the excess electrons on the surface region of the specimen. Good images can therefore be obtained without having to make the specimen conductive, which is often destructive for the specimen.

Because ESEM images are obtained through line-by-line scanning, a certain amount of time is needed to acquire a full image. The principle of measuring crack velocity from ESEM images is shown in Figure 3.8, for the case of a running crack in the vertical direction. From the start time t_1, the scanning time needed to reach the crack tip is Δt_1 in the first image. From the start time t_2, the time needed to reach the new crack tip is Δt_2 in the second image. Thus, the actual time difference between two crack tip locations should be $\Delta t = (t_2 + \Delta t_2) - (t_1 + \Delta t_1)$. And Δt_1 and Δt_2 are derived by dividing the scanned area of image above the crack tip position by the total image area and then multiplying the total scanning time. Practically, this area ratio can be approximated by using the length ratio, which is the length from tip to the upper boundary of image divided by the total length. For the case when the crack propagates along the horizontal direction as shown in Figure 3.9, that is Δt_1 equal to Δt_2, the time difference is directly $\Delta t = (t_2 - t_1)$. The crack velocities derived in both ways are averaged, especially for the discontinuous movement of crack tip. Besides time, the propagated distance of the crack is measured directly from the images whose coordinates are recorded simultaneously. If the crack tip extends out of the initial scanning region, the upper limit for such velocity measurement is dependent on the moving speed of the ESEM specimen stage. If the crack tip is still in the same scanning region, the upper limit then depends on the scan rate. The latter situation is less

common for fast cracking period, because, during the imaging process, the crack tip could have already extended out of the scanning region. The highest velocity that was tracked in this study was approximately 0.6 mm/s, limited by the moving speed of the ESEM stage.

(a) image taken at t_1 (b) image taken at t_2
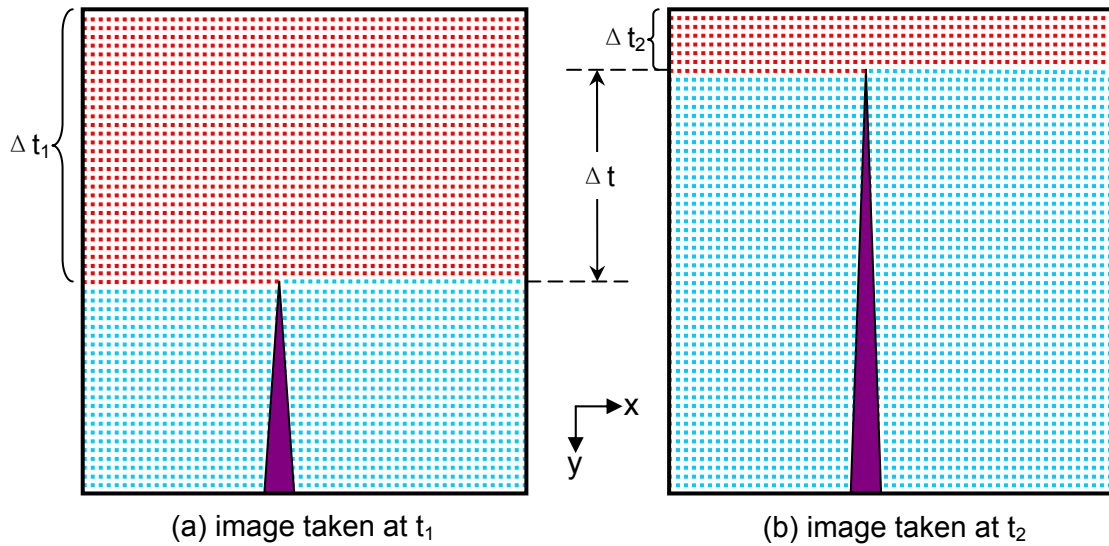
Figure 3.8. Schematic illustration of the ESEM scanning for a propagating crack along vertical direction: (a) the image taken starting at t_1; (b) the image taken starting at t_2. The purple region in each image stands for the crack, red dots denote the scanned points in the area above crack tip and blue dots denote those in the area below the crack tip. Δt_1 and Δt_2 are the time needed for the scanning beam to reach respective crack tips in (a) and (b), while Δt is the actual time spent on this crack extension. Axis-x denotes the horizontal direction and axis-y denotes the vertical direction.

(a) ESEM image taken at t_1 (b) ESEM image taken at t_2
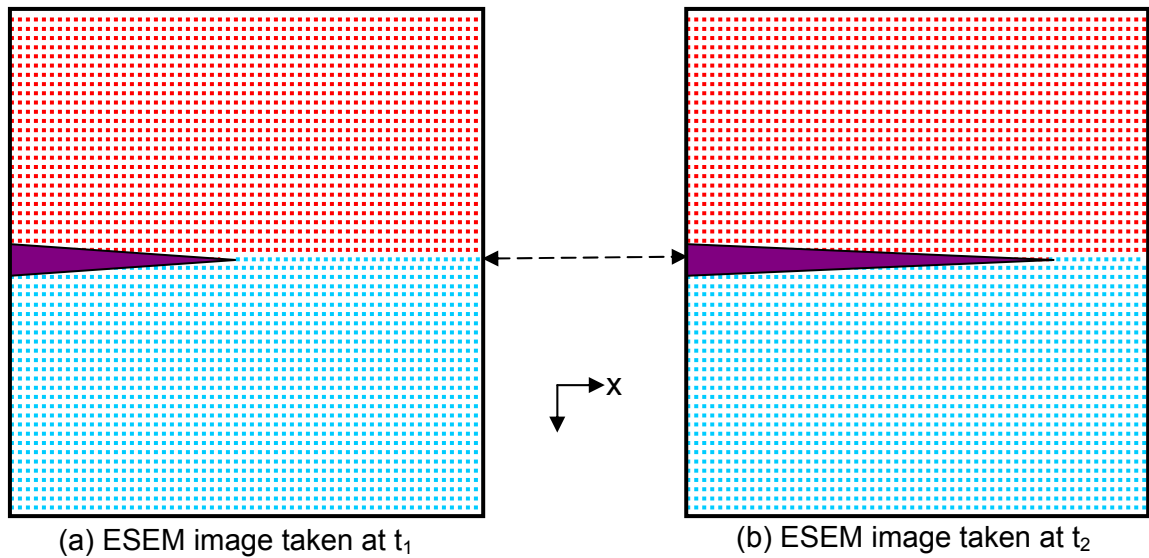
Figure 3.9. Schematic illustration of the ESEM scanning for a propagating crack along horizontal direction.

In this study, most DT-test images were taken using the image resolution of 1024×884 pixels. The frame-scanning time was chosen to be 9.47 s with the line-scanning time of 10.59 ms, thus each of the image was recorded in a relatively short time while still maintaining a reasonable quality for post-mortem analysis. The image resolution of 2048×1768 pixels was used for images that are used for microstructure observation. The gaseous secondary electron detector was used to obtain images of specimen surfaces showing topography information and the SSD/BSE-detector was used to obtain backscattered electron images showing contrast map for different chemical components.

3.3.2. Stereomicroscope

Since good ESEM imaging is only applicable under water vapor pressure below 5 torr or relative humidity below 60%, the Olympus-SZX9 stereo-microscope was adopted to take specimen-surface images during DT tests under high relative humidity. The

Olympus-Altra-20 digital camera mounted to this optical microscope was used to take images of the specimen surface and just a few seconds were needed for recording each. However, due to the relatively low magnification compared with electron microscopes, it is difficult to track the crack tip in real time by using the stereo-microscope alone, especially for opaque materials (interfering the with crack tip detection). However, this situation can be improved by combining a post -processing technique (i.e. the digital image correlation method, DICM) to locate the crack tip and extract the necessary information for calculating velocity. The images of the regions that were expected to contain crack tip were all recorded for post-mortem determination. The crack velocity was then directly derived by dividing the travelled distance of the crack tip by the recorded time between two successive images. Under the optical microscope the maximum velocity that can be measured is expected to be higher than in the ESEM and limited by the shutter speed (less than 1 s) of the digital camera.

The frequency of image recording during the test can be adjusted. This value should be limited to capture small displacements for DICM processing. If the frequency is too high each image taken cannot be recorded in time, leading to storage error and time-consuming post processing. In each test, images were therefore taken at a time interval of about 1 min during the first 10 min and longer afterwards.

3.3.3. Digital image correlation method

The DICM is an image processing technique used to measure 2-dimensional surface displacement or strain fields from time-lapse image series (Chu et al., 1985; Choi and Shah, 1997). The principle of DICM is as follows: In the first image of such series, the

68

area of interests (AOI) is normally undeformed. This AOI is also denoted as the reference region. In the following images, the AOIs are deformed in comparison with this reference. In each image, the corresponding AOI is divided in the same way into many smaller regions called subsets, which are as shown in Figure 3.10. The correlation between these subsets is calculated pixel by pixel and in terms of speckles for each deformed image with respect to the reference one, in order to find the best matching pairs in both images. The general expression of calculation is shown in the following equations:

$$C(x,y,u,v) = \frac{\int_{\Delta M^*} I(x,y) \cdot I^*(x+u+i, y+v+j) dA}{\sqrt{\int_{\Delta M} [I(x,y)]^2 dA \int_{\Delta M^*} [I^*(x+u+i, y+v+j)]^2 dA}} \qquad (3.4)$$

where $i = (\frac{\partial u}{\partial x} \Delta x + \frac{\partial u}{\partial y} \Delta y)$, $j = (\frac{\partial v}{\partial x} \Delta x + \frac{\partial v}{\partial y} \Delta y)$, C is the cross-correlation coefficient, x and y are the coordinates of the pixel in undeformed image, u and v are the corresponding displacements of the pixel, ΔM and ΔM^* denote subsets in undeformed and deformed images respectively, I and I^* denote grey values in undeformed and deformed image respectively and A denotes the area of subset. The maximum value of C gives the best similarity of the subsets. Perfect match ($C = 1$) is not possible due to noise produced during the imaging process, e.g. the change of grey levels even for different images of exactly the same region and the shape of the subset could change between subsequent images. These erroneous effects generally can be treated by Taylor expansion of order zero to two or performing photometric transformation on the processing images. Then, for each subset center, the maximum correlation gives the corresponding subsets and the relative displacement can be calculated. By applying this process for each of the successive images, the evolution of displacement field can be obtained. If the

displacement field is differentiated, the corresponding strain field is thus derived. The lateral (ε_{xx}), axial (ε_{yy}), shear (ε_{xy}) and major principle (ε_1) strains are calculated as:

$$\varepsilon_{xx} = \frac{\partial u}{\partial x} + \frac{1}{2}(\frac{\partial u}{\partial x})^2 + \frac{1}{2}(\frac{\partial v}{\partial x})^2 \tag{3.5}$$

$$\varepsilon_{yy} = \frac{\partial v}{\partial y} + \frac{1}{2}(\frac{\partial u}{\partial y})^2 + \frac{1}{2}(\frac{\partial v}{\partial y})^2 \tag{3.6}$$

$$\varepsilon_{xy} = \frac{1}{2}(\frac{\partial u}{\partial y} + \frac{\partial v}{\partial x}) + \frac{1}{2}(\frac{\partial u}{\partial x}\frac{\partial u}{\partial y}) + \frac{1}{2}(\frac{\partial v}{\partial x}\frac{\partial v}{\partial y}) \tag{3.7}$$

$$\varepsilon_1 = \frac{\varepsilon_{xx} + \varepsilon_{yy}}{2} + \sqrt{(\frac{\varepsilon_{xx} - \varepsilon_{yy}}{2})^2 + (\varepsilon_{xy})^2} \tag{3.8}$$

To be able to obtain high resolution and accuracy, a natural or artificial speckle pattern is required on the surface and is better of tiny size (but not less than the size of 3 × 3 pixels) and irregular distribution. The camera needs to be placed as perpendicular and as distant as possible to the specimen surface to minimize the out-of-plane deformation errors.
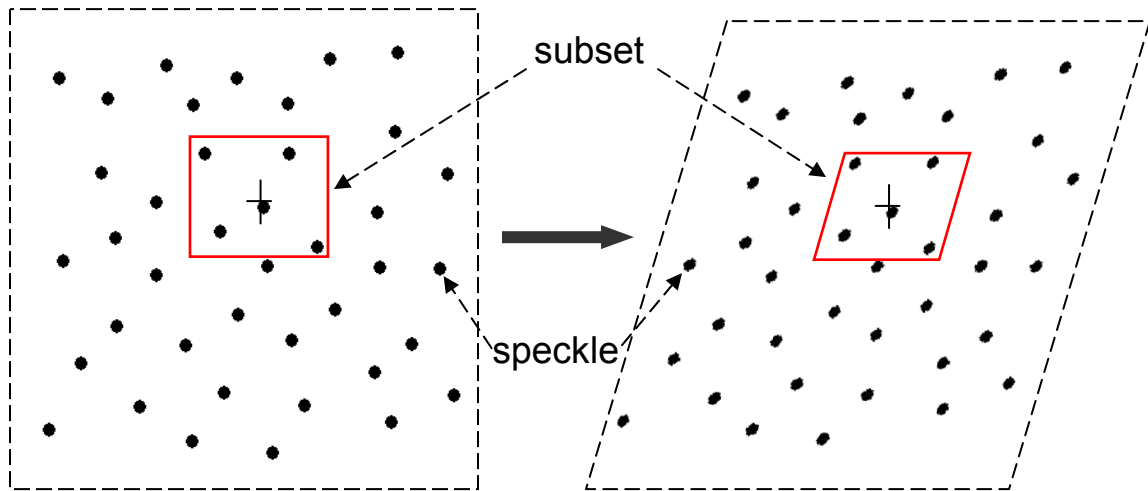
Figure 3.10. Schematic illustration of undeformed (left) and deformed (right) images, and general correlation for the corresponding subsets.

In this study, the resolution of DICM displacement/strain field was not high enough for observing elastic or plastic deformation of small scales. However, it was able to detect the crack tip and its propagations. The accompanying surface deformation was identified in terms of pseudo-strain field (not real strain, because the material surface is parted along the crack). The ε_{xx}, ε_{yy} and ε_{xy} in Equations 3.5, 3.6 and 3.7 were used in Equation 3.8 to obtain the 'major principal strain (ε_1)' field, which functions as pseudo-strain field in this study. Through DICM, the detection of crack tip was realized by comparing two successive deformed images, in the form of incremental-strain field, or it was done by comparing an image to the original, undeformed one, in the form of total-strain field. The determination of crack tip by DICM is not possible on images from high water-vapor pressure conditions inside the ESEM, due to the poor resolution and unrecognizable speckle pattern as shown in Figure 3.11a. The speckles resulting from surface composition variation (e.g. Figure 3.11b) were used as natural speckle pattern for DICM analysis. Under optical microscopes, the crack tips were beyond resolution and difficult

71

to be directly visible. Thus images were recorded for all the possible regions that might contain crack tips and these regions were estimated based on the extent of the force drop. In certain cases, the crack tip was not captured in the images at high magnifications or its extension was too small to be detectable, i.e. less than 10 μm in this study. The identified crack-tip position based on the DICM strain fields may be not precise enough. But it still allows the near-tip position to be recorded and tracked (i.e. distinguished by a border line of two colors in the pseudo-strain field). The velocity of the tip movement was expected to be proportional to the moving rate of the border-line front.
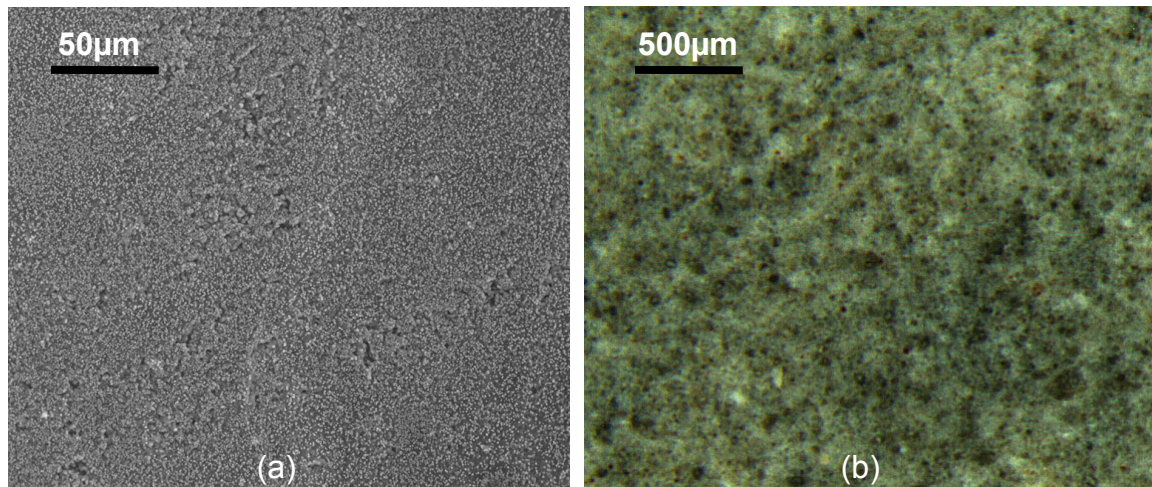
Figure 3.11. Examples of natural speckle pattern of cement paste specimens for digital image correlation: (a) adequate speckle pattern of ESEM image. The speckles come from grayscale variation due to surface roughness and precipitates; (b) adequate speckle pattern of Stereomicroscope image. The speckles are due to composition variation.

The width for a crack shown in the DICM strain fields is dependent on the size of strain window selected. The strain window determines, in the displacement field, the number of adjacent subsets that are weighted for calculating the average strain over a certain region. A smaller strain window can result in higher spatial resolution, and thus

seemingly shaper and thinner cracks. But this also increases the noise ratio as well as miscalculations in the strain-field image, and is more time consuming. An example of the dependence of DICM results on the subset and strain-window sizes are shown in Figure 3.12. The crack opening strain (COS) used in this study to provide an approximate measure for the actual crack opening, as it is calculated through strain windows (size of around 18 μm). These windows are larger than the actual crack width near the tip (1~2 μm or less). The VIC-2D program from Correlated Solutions was employed in this study to perform the digital image correlation.

(a) Subset: 31
Strain window: 15

(b) Subset: 91
Strain window: 15

(c) Subset: 31
Strain window: 45
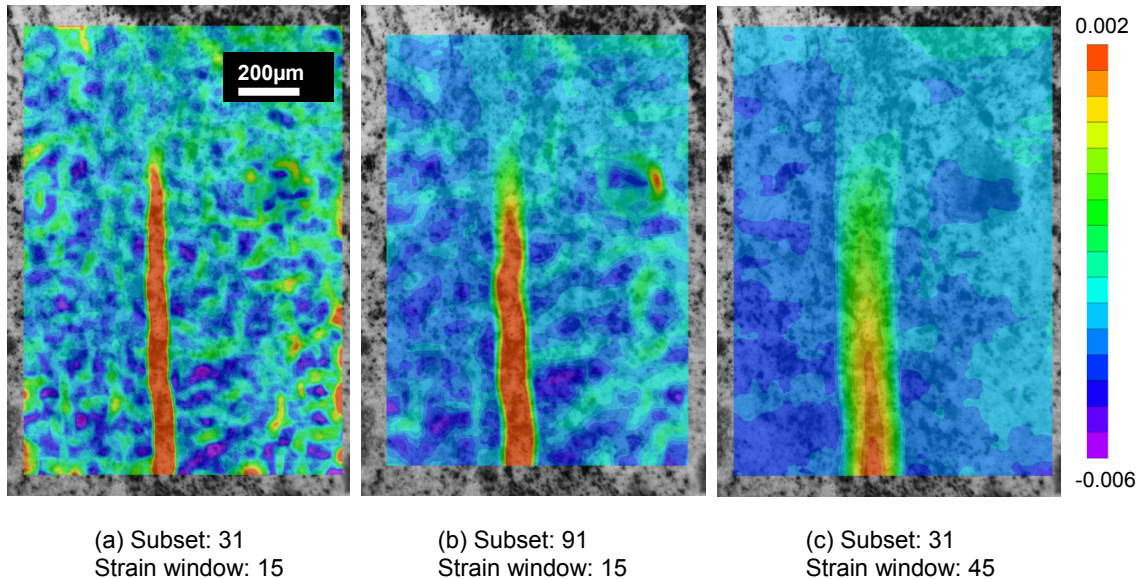
Figure 3.12. Example of the DICM results based on different subset sizes and strain window sizes.

3.4. Experimental program

3.4.1. Double-torsion tests on cement paste

To examine subcritical crack growth in cementitious materials, double-torsion (DT) tests were carried out on cement paste specimens with different w/c-ratios at 10 and 90%

relative humidities (RH). Microscopic images were taken for the crack tip region and post-mortem analysis based on digital image correlation method (DICM) was performed to obtain crack growth rates. The calculated crack velocities (by Equation 3.2) were also compared with the microscopically measured values. Specimen preparation methods are referred to Chapter 3.1.2. Constant-displacement test was employed and the loading configuration is presented in Figure 3.13.
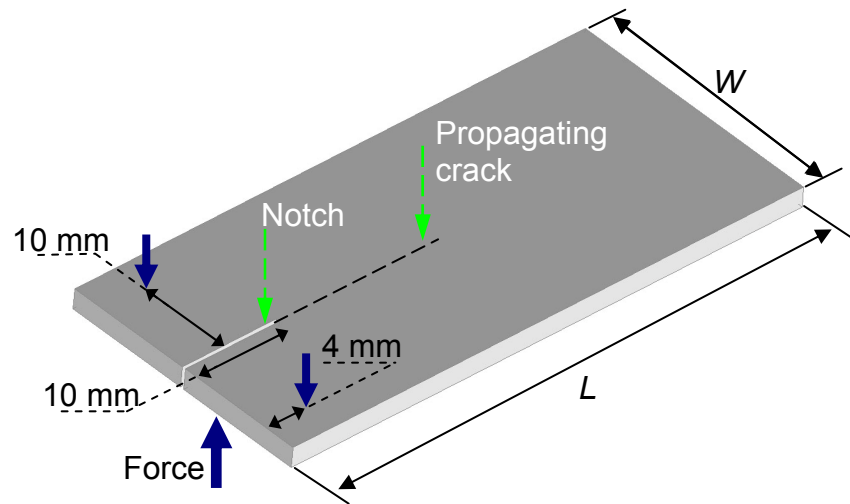
Figure 3.13. Schematic illustration of the DT loading configuration for hardened cement paste specimens. *L* denotes length and *W* denotes width. The crack is not drawn to scale.

Positioning of each specimen on the testing stage was monitored under optical microscope with the accuracy of 0.05 mm. Before the testing stage was transferred into the ESEM chamber, the specimen was also subjected to a force of about 0.1 N to preserve its positioning. The crack tip movement was monitored continuously during each test. The total crack length was controlled to be between 20 and 35 mm, within the range of 15 to 45 mm where the stress intensity factor at the crack tip is independent of the crack length. Within this range, one to three tests were performed on each specimen. The tests in which the subcritical crack deviated significantly (i.e. ≥ 1 mm) from the centerline

were excluded to avoid erroneous force measurement (i.e. much higher than normal values).

A resolution of 1024 × 884 pixels was set for ESEM imaging during DT tests. A resolution of 1596 × 1196 pixels was set for stereomicroscope images and cold light source was placed above the specimen surface to maintain stable lighting. During each test as many microscopic images as possible were taken for the surface region containing the crack tip. Due to the curved geometry of the crack front in the DT specimen (Virkar and Gordon, 1975) and a guiding groove in the compression surface (lower side), the tension surface (upper side) was monitored for imaging crack tip. In ESEM image series of high quality, the crack tip position could be directly identified with accuracy of 2 μm (in terms of crack length, with the accuracy of 0.02% total length). For most cases DICM was used to help identify the crack tips from the microscopic images. DICM settings were optimized case by case for each series of images.

Fracture toughness determination was carried out on extra DT specimens of the same type. Each specimen, with a pre-crack tip in the region where stress intensity factor was independent of crack length, was loaded at a rate of 0.06 N/s (or 1.1 μm/s) until fracture occurred along the centerline. The peak force was recorded and Equation 3.3 was subsequently used to calculate the corresponding fracture toughness.

3.4.2. Creep-induced relaxation tests

Creep-induced relaxation (denoted as CR) tests on cement paste specimens, which exhibit viscoelastic behavior under stress, were performed to examine the relaxation

effect using the double-torsion test set-up. The DT specimens, with the same geometry and treated in the same way as in SCG studies but without any pre-crack at the notch tip, were used. The notch in each specimen was carefully cut to the length of 25 or 27 mm, which was close to the measured length of subcritical cracks, using the diamond saw. This notch was used to approximate an existing subcritical crack that did not propagate (by avoiding high levels of stress concentration at the blunt notch tip). The loading configuration is the same as shown in Figure 3.13. The tests were performed in the similar way as constant-displacement test but without the crack initiation. Each specimen was loaded at a speed of about 1.5 μm/min, till below 90% of the respective peak force recorded for crack initiation in previous SCG studies (usually 0.5 to1 N lower). Specimen was loaded during CR test for the same duration as the loading time spent during DT test. The displacement at the load points were held constant and the creep-induced relaxation test started. Each specimen was examined in ESEM both before and after test to ensure that there was no artificial crack initiated, especially around the notch tip. The measured relaxation curves were compared with those from the DT constant-displacement tests.

3.4.3. Beam-bending tests

In addition to measuring creep-induced relaxation directly on uncracked DT specimens, a standard beam-bending test (Scherer, 2000; Vichit-Vadakan and Scherer, 2000) was carried out to measure the creep-induced stress relaxation. These three-point beam-bending tests were performed on cement paste specimens to qualitatively show the pattern of the creep-induced relaxation under dry and wet conditions, and the effect of w/c-ratio.

76

In these tests, creep-induced relaxation at constant deflection was measured at relative humidities of 10 and 95% for specimens with w/c-ratios of 0.4, 0.5 and 0.6. The specimens, of the size 28 mm × 4 mm × 2 mm without any artificial defects, were cured for 9 to 10 months and then equilibrated at 10 or 95% RH (with respect to the test condition) at 20°C. The flexural tests were carried out on the micro-testing device. The loading configuration is given in Figure 3.14. Specimens were loaded to 2.9 ± 0.1 N at a rate of 0.12 N/s (or 1.1 μm/s), such that no major crack was initiated before or during the relaxation test. Then the deflection imposed by the loading rods was held steady and the relaxation of force was recorded. Note that, the thin nature (2 mm) of the specimens helped reduce the possible internal residual stresses resulting from nonhomogeneous equilibration (over the thickness in large specimens) with the environmental water content (Bažant et al., 1976). Thus the observed relaxation was not considered to be associated with the internal stress state. All the tests lasted for 30 min, same as the duration of DT tests. Fracture tests by bending the specimens to break were also performed under the same conditions.
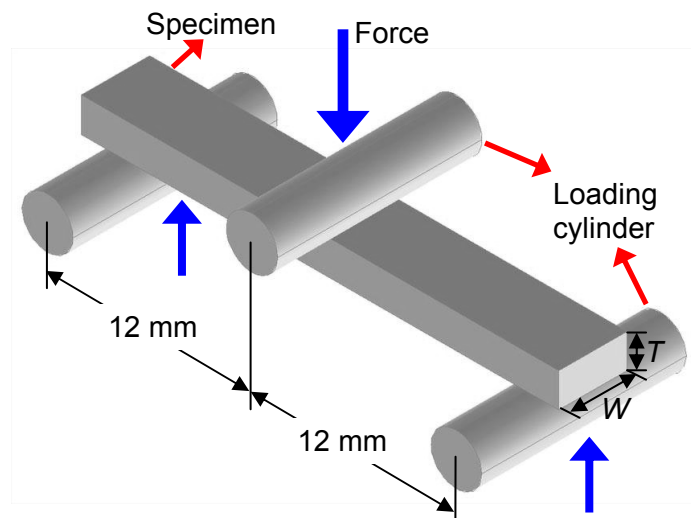
Figure 3.14. Schematic illustration of the bending configuration. W and T denote the thickness and width of the specimen respectively. The upper loading cylinder is placed on the center position of the specimen along its length.

3.4.4. Double-torsion tests on calcite crystals

Single-crystal calcite ($CaCO_3$) behaves linear-elastically and is free from significant dislocation creep at room temperature (Bažant et al., 1993; Barber and Wenk, 1978; Renner et al., 2002). It fractures straight along its cleavage planes. In order to provide a comparison with the cement paste specimens, calcite specimens obtained from Photox Optical Systems Ltd. (Røyne et al., 2011) were used as reference specimens. The dimension of the as-received calcite specimens is 30 mm × 10 mm × 1 mm (length × width × thickness), with surfaces of 30 mm × 1 mm parallel to cleavage plane and other surfaces normal to this plane. The 30 mm ×10 mm surfaces were optically polished. A cleavage pre-crack (notch), with a length of approximately 3 mm, was machined at one end. The picture of the specimen is as shown in Figure 3.15a.

(a)   (b)
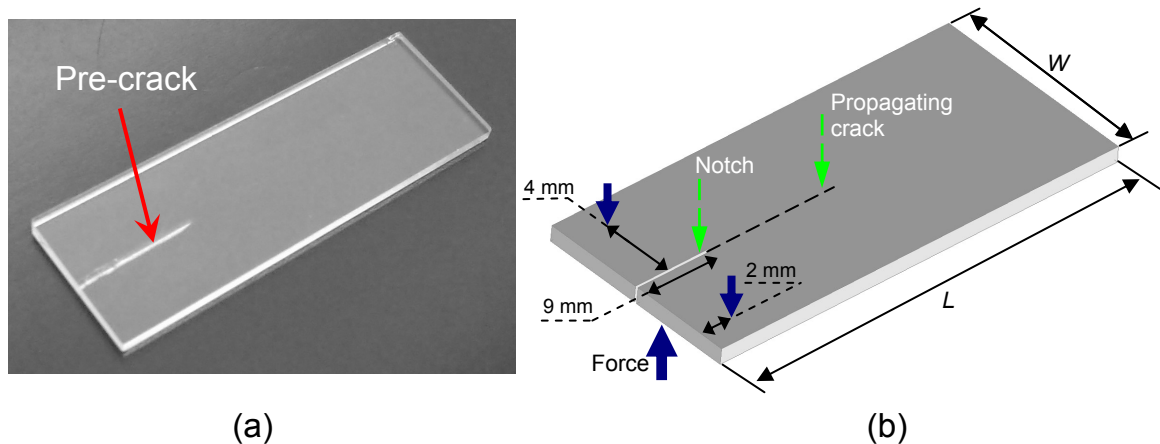
Figure 3.15. (a) Image of the single-crystal calcite specimens and (b) schematic illustration of DT loading configuration. *L* denotes length and *W* denotes width. The crack is not drawn to scale

78

Double-torsion (DT) tests were performed on single-crystal calcite specimens. The calculated subcritical crack velocities (by Equation 3.2) and the optically measured values were obtained. The two sets of measurements were compared respectively to show that whether, by using the DT micro-testing device built in this study, the calculated values can be consistent with the optical ones. To reach this goal, constant-displacement test mode was employed and the loading configuration is given in Figure 3.15b. Each specimen was marked and the positioning of it on the testing stage was done by aligning the mark with respect to the loading point connected to the force cell. This process was monitored under optical microscope with an accuracy of 0.05 mm. Then before the testing stage was transferred into the ESEM chamber, the specimen was subjected to a force of about 0.1 N to preserve the accurate positioning while minimize the erroneous influence from applied force before testing. The crack tip movement was monitored using the secondary-electron (SE) detector throughout the test. During each imaging process, coordinates of the center position were recorded. The total crack length was controlled to be between 9 and 15 mm, within the range from 5 to 23 mm where the stress intensity factor at crack tip is independent of the crack length. Due to this narrow range, only a single test was performed on each specimen. To improve the quality of imaging and to facilitate the detection of crack tip, the experiments were carried out at 1% relative humidity (RH) and 25°C for about 20 min. A resolution of 1024 × 884 pixels was set for ESEM images.

3.4.5. Self-healing tests

Cementitious materials can exhibit the self-healing phenomenon, which is facilitated either by chemical products from the materials or by substances from the surrounding environment over a certain period of time. According to previous studies, certain conditions need to be fulfilled for self-healing of cracks to occur in cementitious materials:

(1) The crack width has to meet certain criteria, below 150 μm and preferably below 50 μm, to allow cracks to heal effectively (Li, 2007; Reinhardt, 2003; Mangat and Gurusamy, 1987). Otherwise the cracks cannot be healed completely;

(2) The water content is critical to the self-healing of cracks, higher exposure to water leads to higher degree of healing. In contrast, cracks in dry cementitious materials don't show self-healing (Nishiwaki et al., 2006; Edvardsen, 1999);

(3) The presence of specific species such as unhydrated or partially hydrated cement particles enables the healing to occur. Higher temperature, if not too high, is also found to facilitate the self-healing of cracks (Reinhardt, 2003).

The subsequent microcrack closing can help to limit harmful effects for cement-based materials (e.g. the chloride ingress according to Jaobsen et al., 1996). This phenomenon is also expected to be present in subcritical cracks, of which the width can be less than 50 μm for the part close to the tip. Moreover, because the subcritical crack is growing in a relatively slow manner, crack healing can be expected to take place simultaneously. Subcritical cracking and crack healing can therefore be two competing time-dependent processes. But the relative importance of self-healing in subcritical cracks is unknown.

To examine the self-healing of subcritical cracks in cementitious materials and its effect on crack growth, specimens with the same geometry and prepared in the same way as DT specimens were used. The w/c-ratios of the specimens were 0.3 and 0.7. Specimens with the w/c-ratio of 0.3 were cured for 1 month and those with 0.7 were cured for 8 months. The DT test was performed on each specimen inside ESEM to introduce subcritical crack with a length of 20 to 30 mm.

The pre-cracked specimens were subjected to wet-and-dry cycling for 1 month (about 15 cycles) and then submerged at 20°C in saturated calcium hydroxide water (limewater) for another 5 months to enhance healing and limit leaching, as commonly seen for concrete materials (Hearn, 1998). One cycle corresponded to limewater-submersion for 24 hours and then drying in 65% RH conditioning room at 20°C for another 24 hours. This cycling was used to enhance the self-healing effects in the specimens. After the submersion period, constant-displacement DT tests were again performed on the specimens. The relaxation recording of each test started once a load drop occurred due to the onset of fresh cracking. It is important that the recorded new cracking was not due to the propagation of the previously-formed crack, so that the effect of self-healing can be identified. This requirement was ensured by optically monitoring the new crack tip and comparing it with the previous one (i.e. X and Y coordinates of the crack tip). Several specimens were left intact for optical studies inside ESEM. A solid state detector (SSD) for backscattered electrons (BSE) was used for imaging distinctive healing products from other phases, i.e. hydrated, unhydrated cement particles.

3.4.6. Experimental overview/summary of testing programs

An overview of the tests performed in this study is presented in Table 3.4. The temperatures of specimens were kept in the range of 15 to 20°C, close to the room temperature (i.e. 20°C). The specimen temperature was therefore easy to achieve and the measured temperature variation across the specimen was within ±1°C. To obtain the specific relative humidities, the Buck equation that describes the relationship among water vapor pressure, relative humidity and temperature was referred to (Buck, 1996).

Table 3.4. Microscopes and testing conditions adopted in different experimental tests for hardened cement paste (HCP) specimens with different added w/c-ratios. The numbers denote number of tests on different specimens.

Test	Relative humidity	w/c-ratio				
		0.3	0.4	0.5	0.6	0.7
DT-test inside ESEM	10%	3	3	8	4	3
DT-test under Stereomicroscope	90%	4		5	3	4
Beam-bending test	10%		3	3	3	
	90%		3	3	3	
Creep-induced relaxation test	10%	3		3	3	3
	90%	3		3	3	3
Healing test	10%	3				3
Fracture toughness test	10%	4		3	4	6
	90%	5		5	3	3

* ESEM denotes Environmental SEM, OM denotes Stereomicroscope

CHAPTER 4 Experimental observations

4.1. Double-torsion tests on calcite crystals

To examine if, for a non-creeping material, the crack velocities calculated from relaxation curves is consistent with those measured optically using the built-testing device, DT tests were performed on single-crystal calcite specimens. The ESEM images showing the crack propagation are presented with respect to the data points in the force-time curve. It is found that the propagation of the subcritical crack can be tracked in time by using the built testing device inside the ESEM, except for the fast growing period (i.e. normally within the first 30 s in this study). The crack path is straight along the specimen's cleavage plane, where the strain energy release rate is expected to be at the maximum. And guiding grooves, which help ensure the crack propagation along the specimen centerline, are therefore not required. Single-crystal calcite is therefore suitable for carrying out DT test. An example of the measurements is shown in Figure 4.1.

The subcritical crack can be easily detected as a white line by using the secondary-electron detector (e.g. Figure 4.1a, c and e). The crack tip is defined as a point at the forefront of the white line where it changes to black (e.g. where the arrows point to, in Figure 4.1). Although this might not be the exact tip position, it is expected to be able to represent the crack tip with an accuracy of ± 2 μm. The total growth of a subcritical crack that can be recorded was between 50 and 200 μm. Also it is noted that the decrease of force with time was not perfectly smooth during the test (e.g. in Figure 4.1), due to stepwise propagation of the cracks.
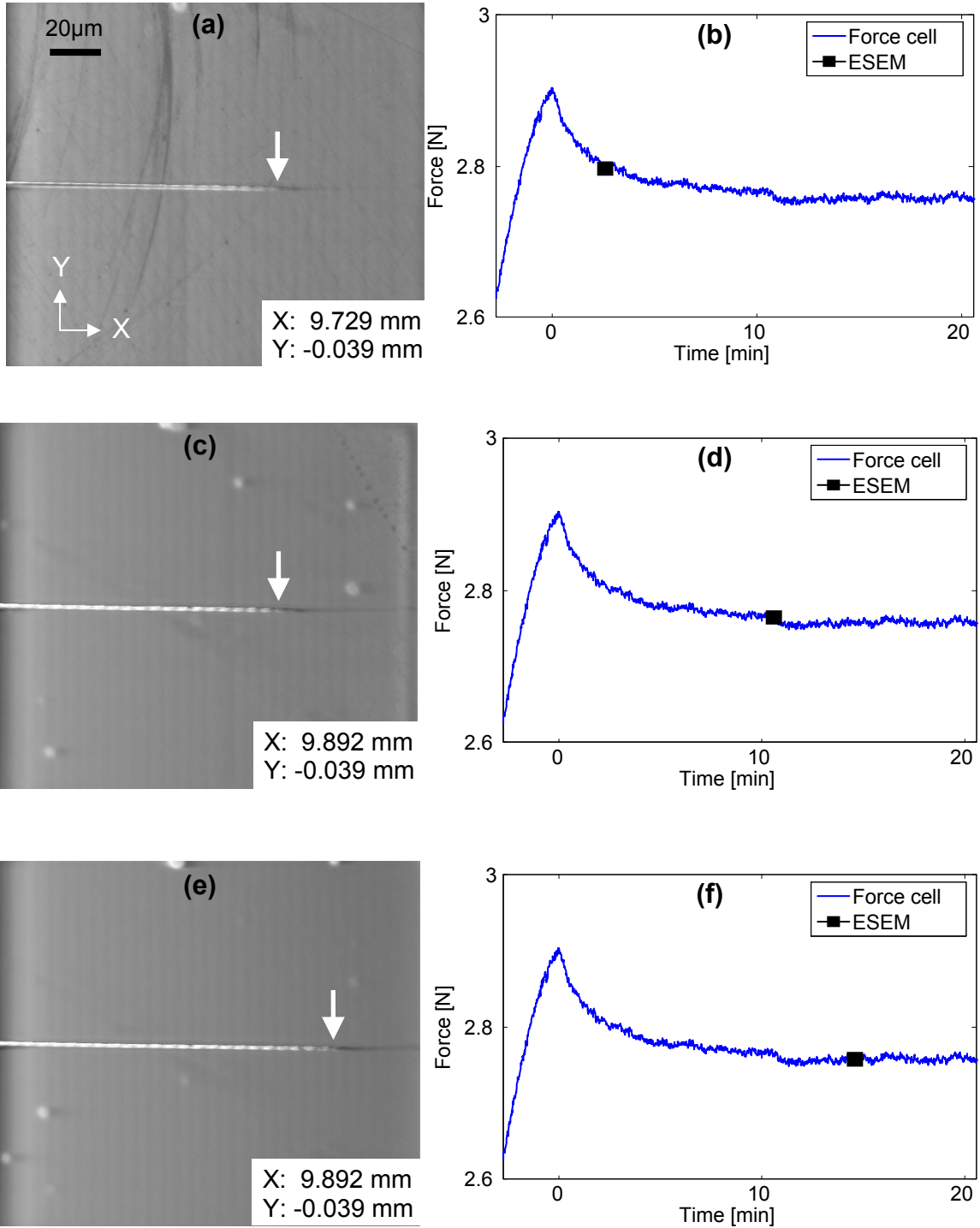
Figure 4.1. Examples of the DT test results on a single-crystal calcite specimen. (a), (c), and (e) are the ESEM secondary-electron images recording the crack tip movement. X and Y denote the coordinates (accuracy of ±1 μm) of the center position in each image (for the loading point: X = -0.039 mm, Y = -3.296 mm). The arrow indicates the tip region. (b), (d) and (f) are showing the

corresponding points in the force-time curve. The square marker represents the data at each imaging time. The starting time of the relaxation test is "0 min".

A comparison between the crack velocities obtained from the force-time curves and those from the ESEM images is made in Figure 4.2. The two sets of data are generally consistent with each other. Likewise, no evident erroneous relaxation resulting from the testing device can be identified. The crack propagation was decelerating exponentially and during much of the test the velocities were in the range of 10^{-5}~10^{-7} m/s.
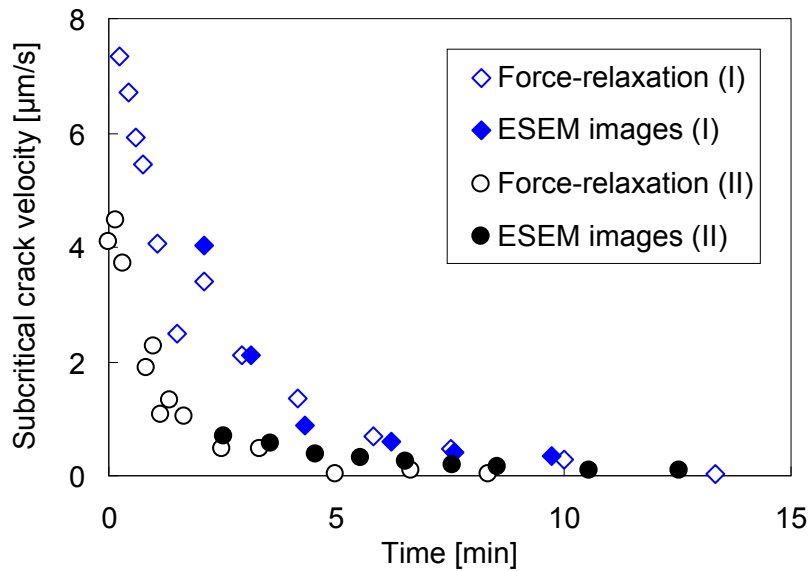
Figure 4.2. Double-torsion test results for different calcite specimens at 1% RH and 25°C. Open data points denote the velocities calculated from the force-time curves, solid data points denote the velocities measured from ESEM images.

4.2. Subcritical crack growth studies on hardened cement paste

4.2.1. Microstructural observations

To examine the microstructure of the hardened cement paste along the subcritical crack, specimens were observed in the ESEM after being tested or fractured. The subcritical cracks were macroscopically straight along specimen centerline, while being tortuous

microscopically. The subcritical cracks were mostly observed to propagate continuously through the hydrated cementitious matrix. In the presence of unhydrated cement particles, the crack appeared to circumvent the unhydrated particles and propagated along the interfaces between the unhydrated particles and hydrated matrix.

Examples of the BSE and SE images are presented in Figure 4.3, showing the subcritical-crack-path patterns and some hydration products observed at the fresh crack surfaces (i.e. CH and entringite inside the voids). For specimens with lower w/c-ratio of 0.3 and 0.5, more unhydrated cement particles existed (e.g. Figure 4.3a and b), and cracks often changed direction to pass around unhydrated cement particles. Crack propagation, through air voids and with some minor components of cement paste, can be observed at crack surfaces (e.g. calcium hydroxide and ettringite in Figure 4.3e and f) as well, but was not found to influence the crack direction significantly.
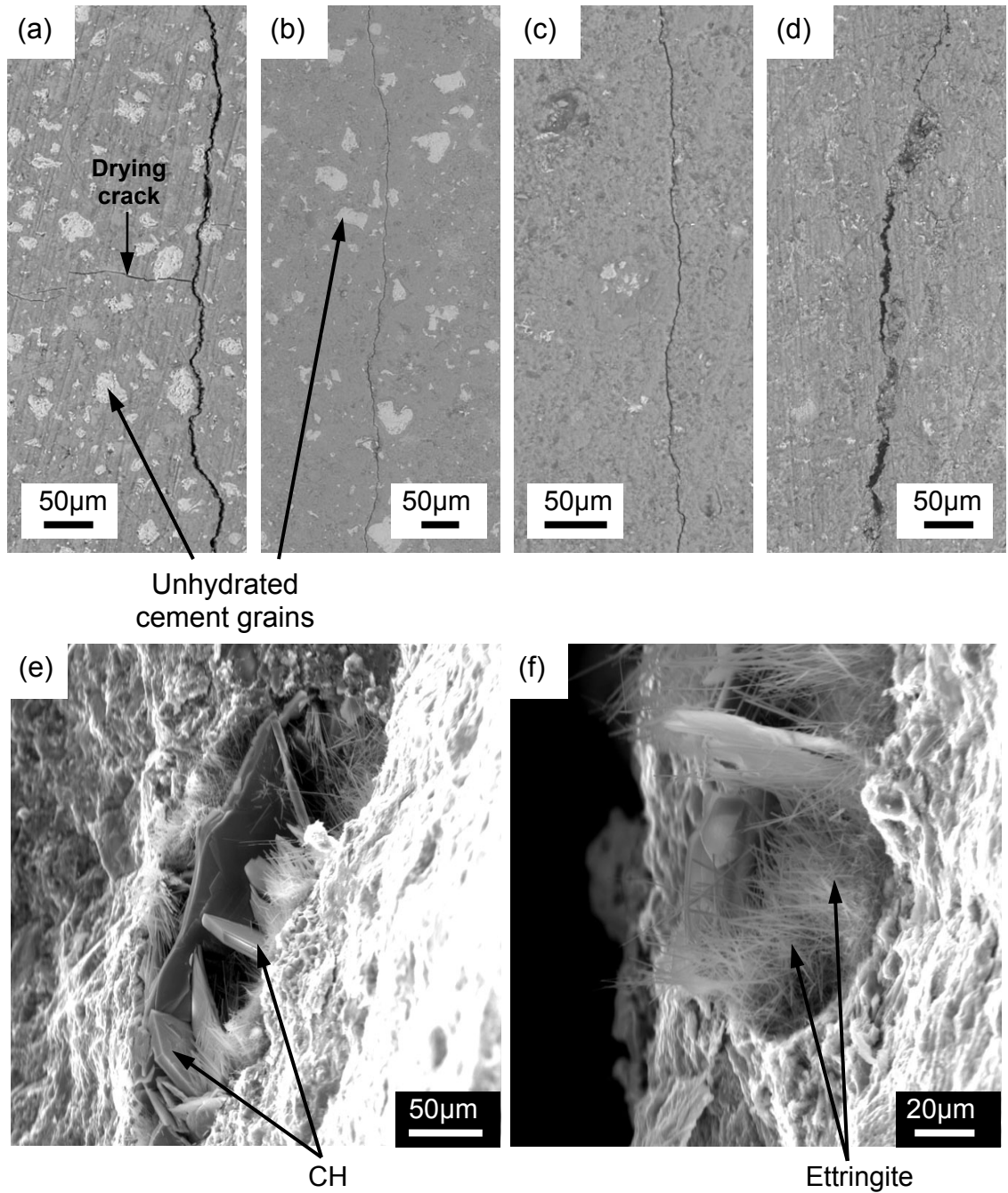
Figure 4.3. BSE images showing crack paths (major cracks along the vertical direction) in different cement paste specimens (impregnated with epoxy): (a) w/c=0.3; (b) w/c=0.5; (c) w/c=0.6; (d) w/c=0.7. (e) and (f) are SE images showing the fresh crack surfaces in fractured specimens.

4.2.2. Traditional double-torsion test results

In order to evaluate the SCG behavior and compare the DT-test results in this study with those published earlier for cement pastes (Mindess et al., 1974; Evans et al., 1976; Beaudoin, 1985), subcritical crack velocities (v) and stress intensity factors (K) calculated using Equations 3.2 and 3.3 were plotted in the traditional K-v diagrams. Results of the diagrams for Portland cement paste specimens with added w/c-ratios of 0.3, 0.4, 0.5 and 0.6 at 10 or 90% RH are presented in Figure 4.4 and Figure 4.5. These diagrams show the systematic trend of the K-v curves for specimens with the different w/c-ratios. However, among those with the same w/c-ratio, scattering of the curves can also be observed. For given moisture content (i.e. 10 or 90% RH), the K-v curves lie in the regions with higher K values for the specimens with lower w/c-ratios. And in all of these curves, the plateau that corresponds to Region-II behavior during SCG was not observed. The apparent crack velocities are between 10^{-2} to 10^{-9} m/s.
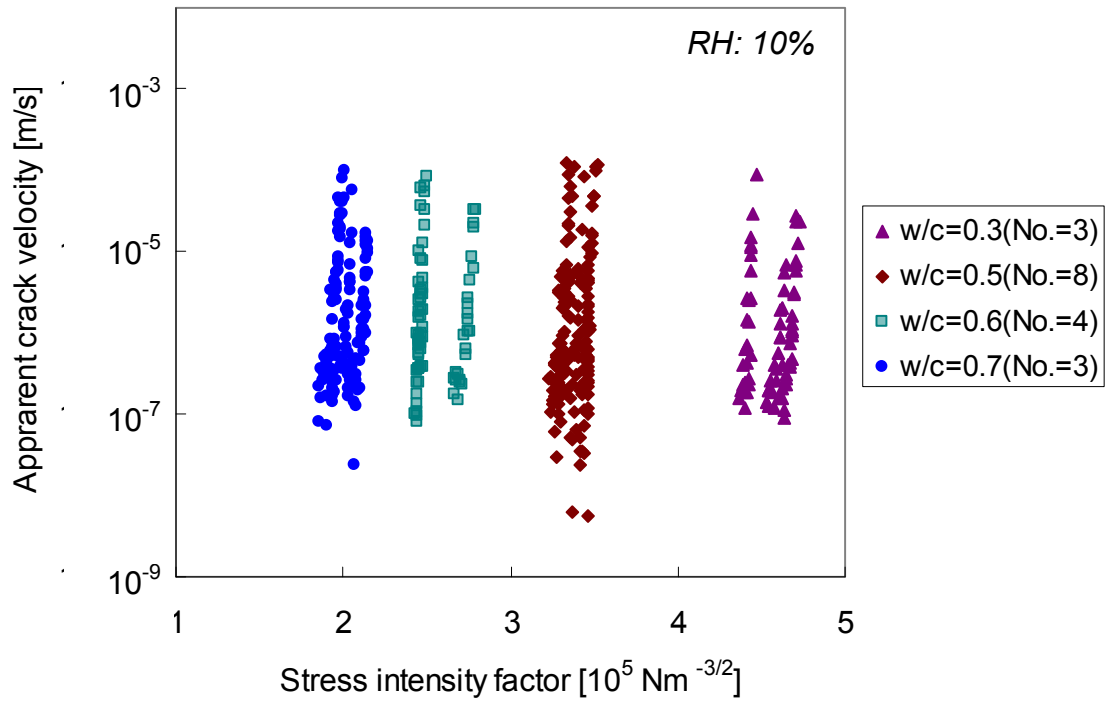
Figure 4.4. Apparent subcritical crack velocities versus stress intensity factor, calculated from load-relaxation measurements, for specimens with different w/c-ratios at RH of 10%. Each *dot* in the diagram represents a single pair of calculated values for *K* and *v*.
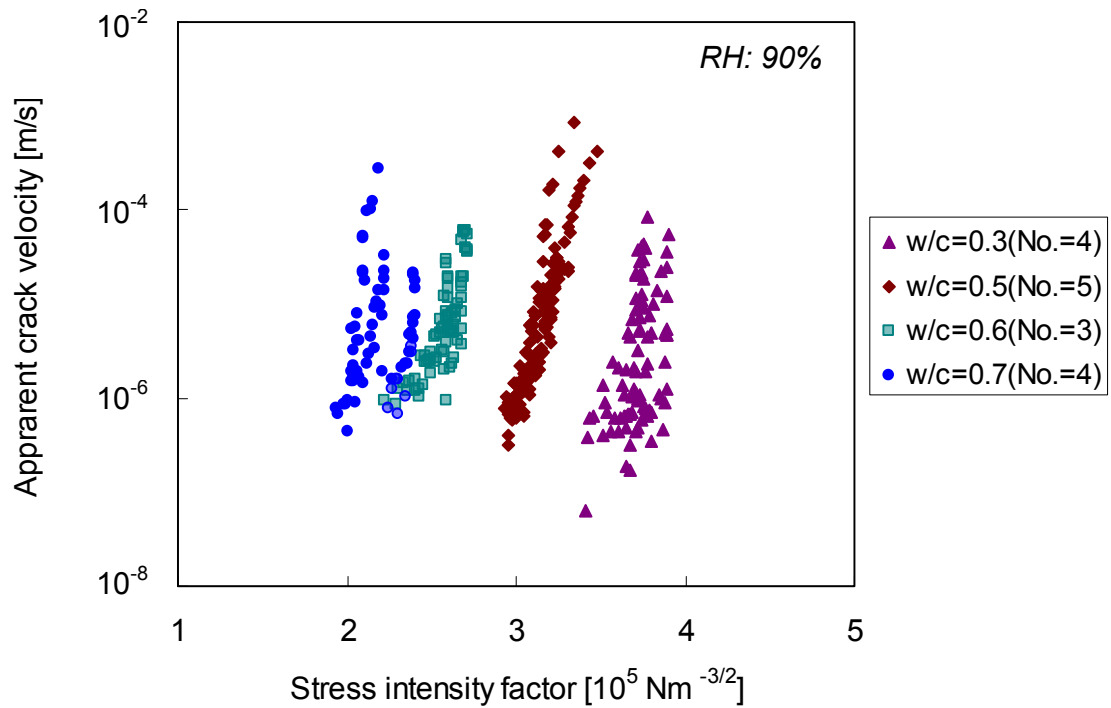
Figure 4.5. Apparent subcritical crack velocities versus stress intensity factor, calculated from load-relaxation measurements, for specimens with different w/c-ratios at RH of 90%. Each *dot* in the diagram represents a single pair of calculated values for *K* and *v*.

The fracture toughness, or critical stress intensity factor (K_{Ic}), measurement is presented in Figure 4.6 as a function of w/c-ratio at 10 and 90% RH. A downward trend can be observed for the K_{Ic} with the increase of w/c-ratio. Moreover, the specimens at 10% RH show higher values of K_{Ic} than those at 90% RH with the same w/c-ratio.
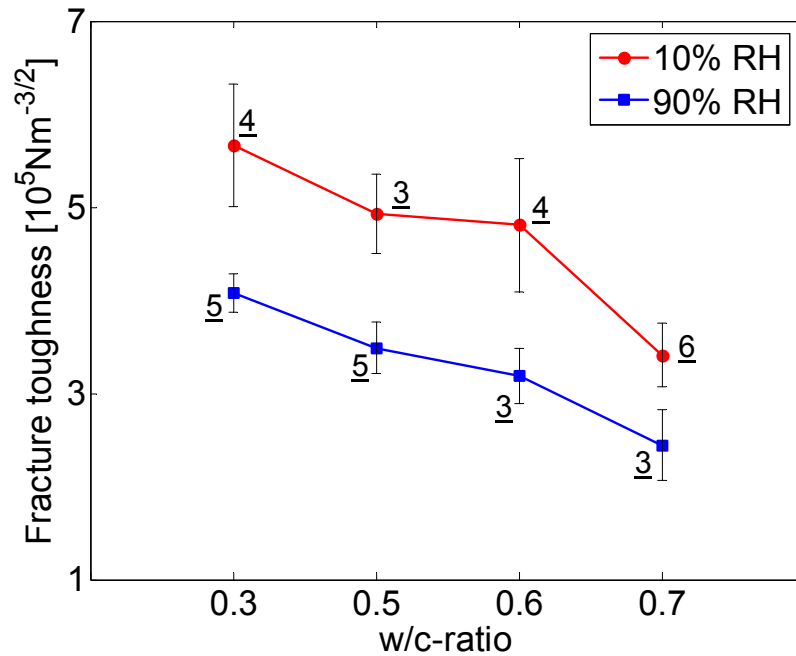
Figure 4.6. The average values of the facture toughness versus w/c-ratio for hardened cement paste specimens at 10 and 90% RH. Error bars represent the corresponding standard deviations from the average values. Underlined numbers denote the number of measurements for the respective test.

Apart from the interpretation of the results of K_I and v, the slope n of the K-v curve (when in *log-log* scale), referred to as the subcritical crack index, offers another measure for the susceptibility of the material to subcritical cracking. The average values of the subcritical crack index based on the apparent crack velocities are listed in Figure 4.7, for specimens with different w/c-ratios and under different relative humidities. Apparently, the n-values are lower for all specimens at 90% RH than at 10% RH. No clear influence of w/c-ratio (or porosity) can be observed.
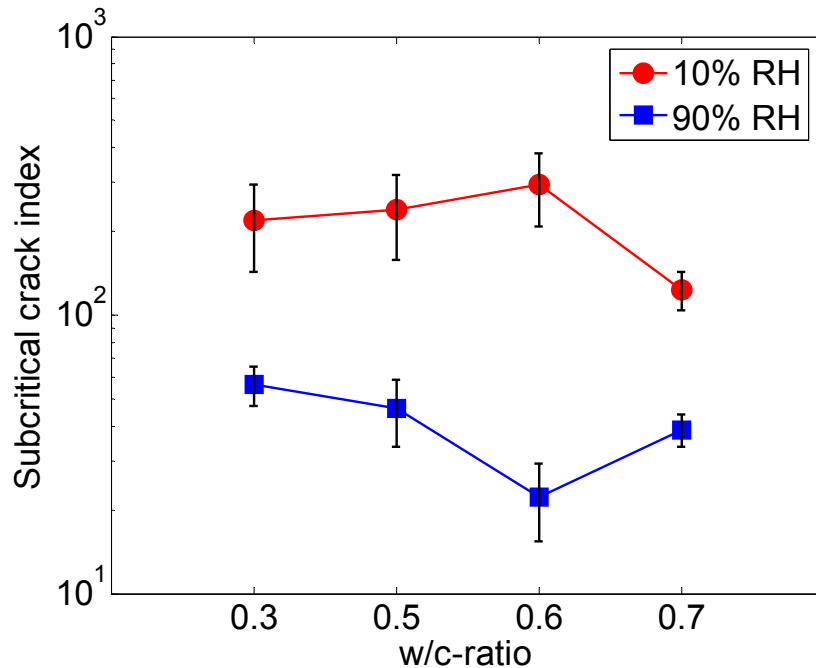
Figure 4.7. The average values of the apparent subcritical crack index versus w/c-ratio for hardened cement paste specimens at 10 and 90% RH. Error bars represent the corresponding standard deviations from the average values.

4.2.3. Optical studies at 10% RH (ESEM)

Under dry conditions the DT tests were performed inside ESEM, while for wet conditions high-resolution ESEM imaging was not applicable as explained earlier (see Chapter 3.3.1). In all constant-displacement tests carried out at 10% RH in the ESEM, the propagation or absence of propagation of the crack tip could be optically recorded at high magnifications (800 to 3200×) with further confirmation from DICM analysis for most cases. Local deceleration or acceleration of subcritical cracking can be optically observed occasionally but difficult to record inside ESEM, because of the limit of acquisition-time. The examples showing the capability of DICM for identifying crack propagation in cement paste specimens during DT tests are presented in Figure 4.8. The crack and its growth can be identified through DICM (e.g. Figure 4.8c and Figure 4.8d) as the region

92

showing the highest pseudo-strain values (up to 0.02). The surface-region displacement resulting from opening of the crack can also lead to higher pseudo strain than less deformed or undeformed regions (e.g. comparing Figure 4.8b to Figure 4.8a), besides that due to newly formed crack.

In Figure 4.8, from 336 s till 456 s the crack tip was in the same imaging region and traveled over a distance of about 20 μm. Between 456 s and 700 s, the crack growth accelerated. And at 1000 s, new location over a further distance of about 300 μm was recorded for the tip region.
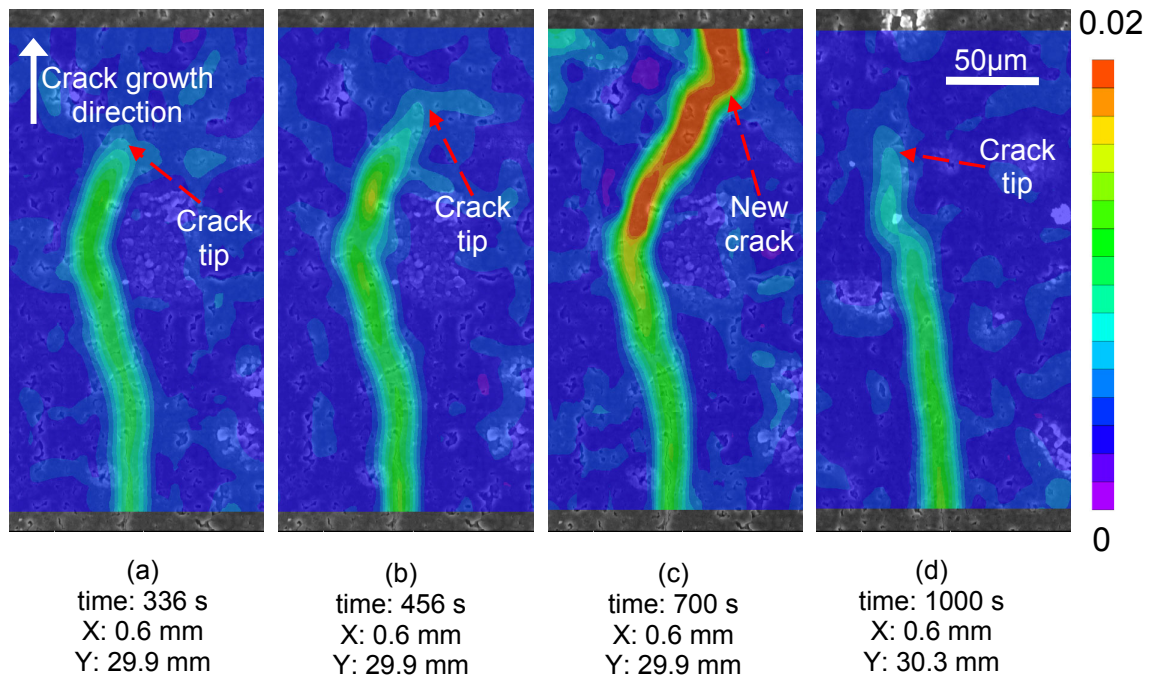
Figure 4.8. Example of the DICM performed on ESEM images showing subcritical crack propagation in cement paste specimen at 10% RH by pseudo-strain field. 'time' denotes the imaging time referring to the start of the DT test. X and Y denote respectively the horizontal and vertical coordinates of the center position of each image. The color-bar denotes the scale of the pseudo strain applied in DICM to present the strain map.

In principle, all the DT tests performed at 10% RH showed rapid deceleration of the subcritical crack growth after the initial cracking and the crack was arrested within minutes. During the test afterwards, the propagation of the subcritical crack was not identified under high magnifications, while the continued force-relaxation was still observed. In some tests, discrete cracking could be observed occasionally during this period but subjected to crack arrest often soon after. An example of the measurement in ESEM for a specimen with w/c-ratio of 0.3 is presented in Figure 4.9, showing the absence of crack propagation during much of the DT test at 10% RH. No crack propagation after 28 s was observed in the DT test with duration of about 30 min. The crack was identified through the ESEM and DICM results (see Figure 4.9) and the tip position was monitored. With the accuracy of 5 μm at the magnification of 3200×, the crack tip was not directly observed to be moving during the test. DICM results also showed, besides the increase of the crack-opening width, no evident crack propagation (see Figure 4.9b and c). According to the velocities calculated for the expected subcritical cracking (see the *K-v* diagram in Figure 4.9), the total length of propagation should be above 180 μm (assuming 0.1 μm/s for 30 min), but this was not observed from the ESEM images.
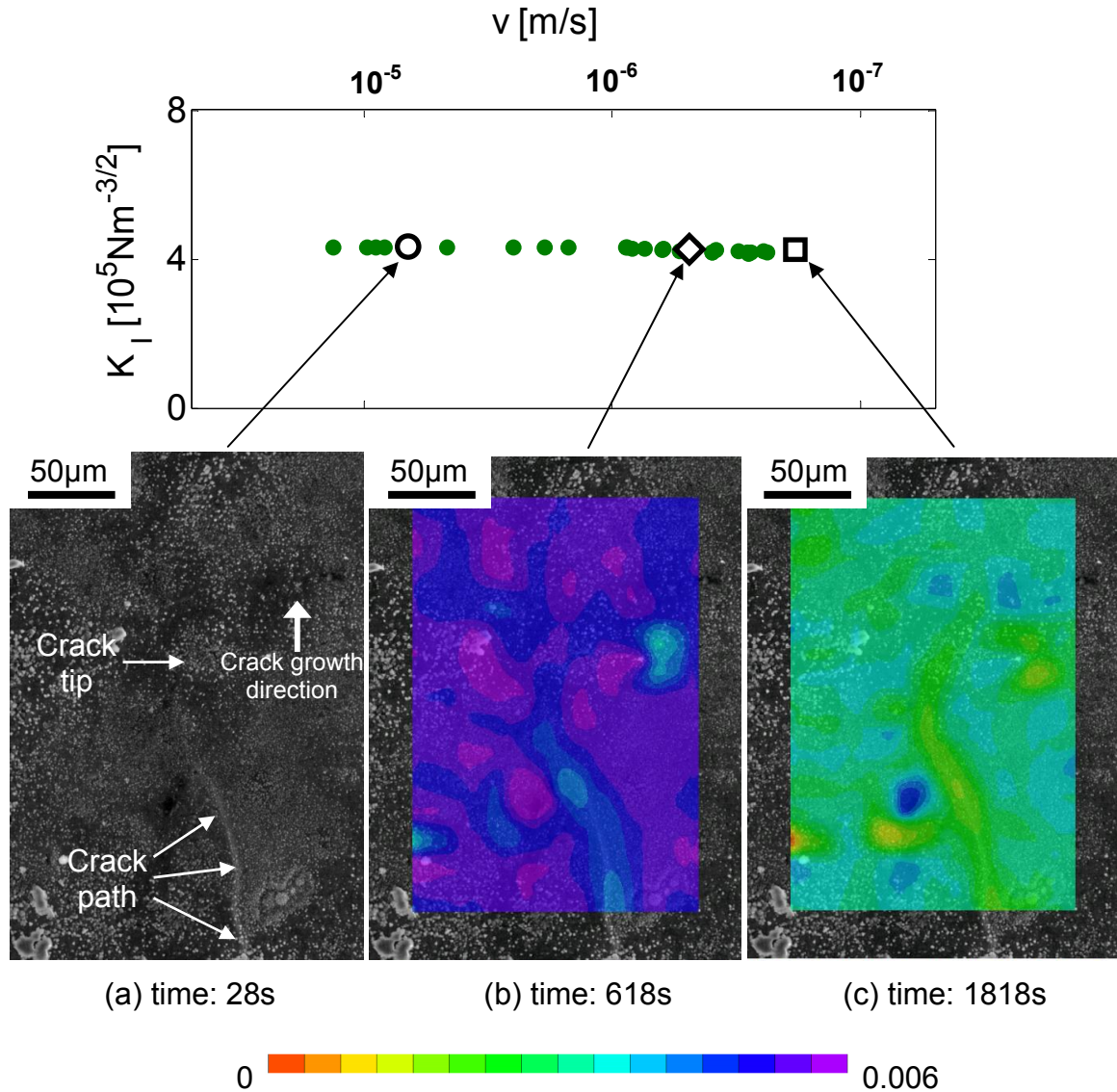
Figure 4.9. Measurements in ESEM showing no visible crack propagation in the specimen with w/c-ratio of 0.3, during DT test at 10% RH. (a) is the ESEM image recorded at 28 s after the start of the test, with the visually-identified crack tip. (b) and (c) are ESEM images recorded respectively at 618 s and 1818 s for the same crack tip region, with the DICM results referring to (a). Corresponding data points in the *K-v* curve is also presented. The color-bar denotes the scale of the pseudo strain applied in DICM to present the strain map.

Another example showing the absence of crack propagation during much of the DT test at 10% RH is shown in Figure 4.10. The crack tip and crack path were identified first

through ESEM observation during the test. With the accuracy of 5 μm at the magnification of 3200×, the crack tip was not directly observed to be moving during the test after 50 s and until 1845 s (Figure 4.10a and b). The crack tip position was also examined through the DICM analysis (see Figure 4.10c). The reference image was not the one containing uncracked surface but containing already cracked surface. The results showed that the identified crack tip was in the same region (±10 μm) as observed through the ESEM. The crack distinguished by DICM was due to the increase of the crack-opening width. According to the velocities calculated for the expected subcritical cracking, the total length of propagation should be above 180 μm (assuming 0.1 μm/s for 30 min), but this was not observed from the ESEM images. No evident crack propagation was identified during much duration of the DT test.

100μm

Crack
tip

Crack
path

Crack
growth
direction

(a) time: 50s   (b) time: 1845s   (c) time: 1845s

-0.001   0.006
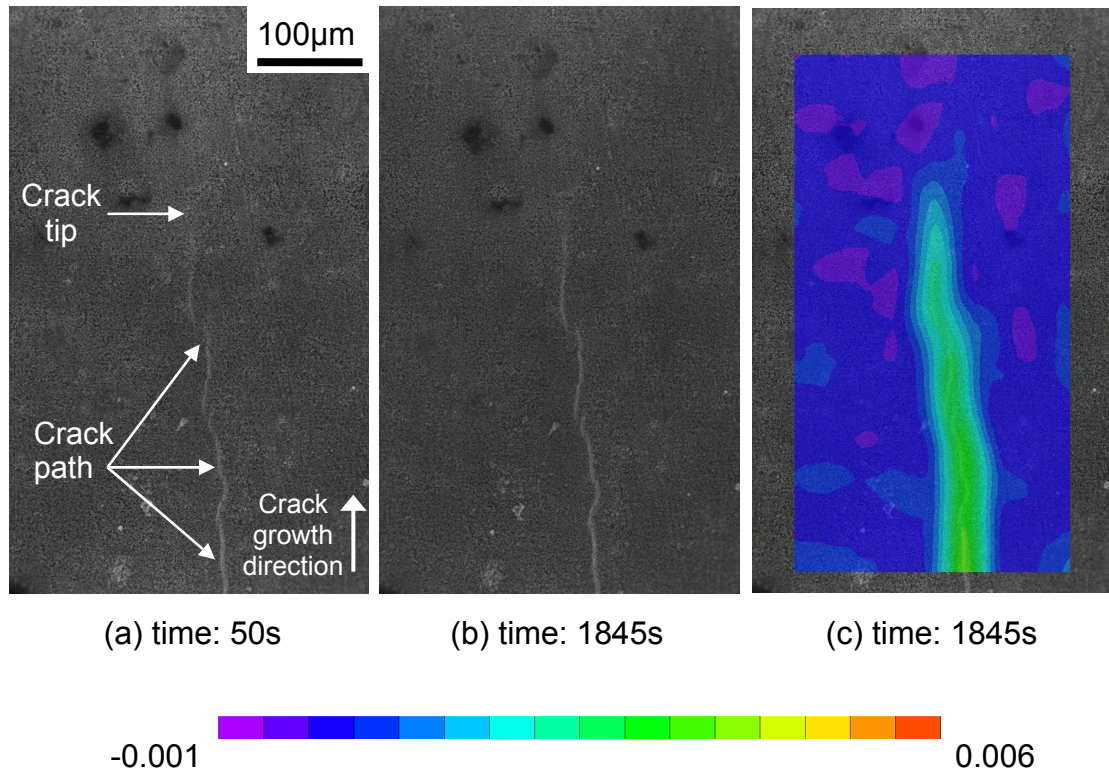
Figure 4.10. Example of DICM performed on the ESEM images showing no significant crack propagation in the specimen with w/c-ratio of 0.5, during DT test at 10% RH. (a) is the ESEM image recorded at 50 s after the start of the test, with the visually-identified crack tip. (b) is the ESEM image recorded at 1845 s. (c) is the ESEM image recorded at 1845 s with its DICM result referring to (a), in terms of pseudo-strain field. The color-bar denotes the scale of the pseudo strain applied in DICM to present the strain map.

An overview of the DT tests with no notable subcritical cracking during much of the measured relaxation is given in Figure 4.11. In about 70 relaxation tests at 10% RH, subcritical cracking stopped within the first 5 min of the test. In all these tests, the measured specimen force-relaxation was continuous during the whole period. From the relaxation measured after, e.g. 5 min, the expected crack growth according to Equation 3.2 ranged between 20 and 100 μm, which was not observed.
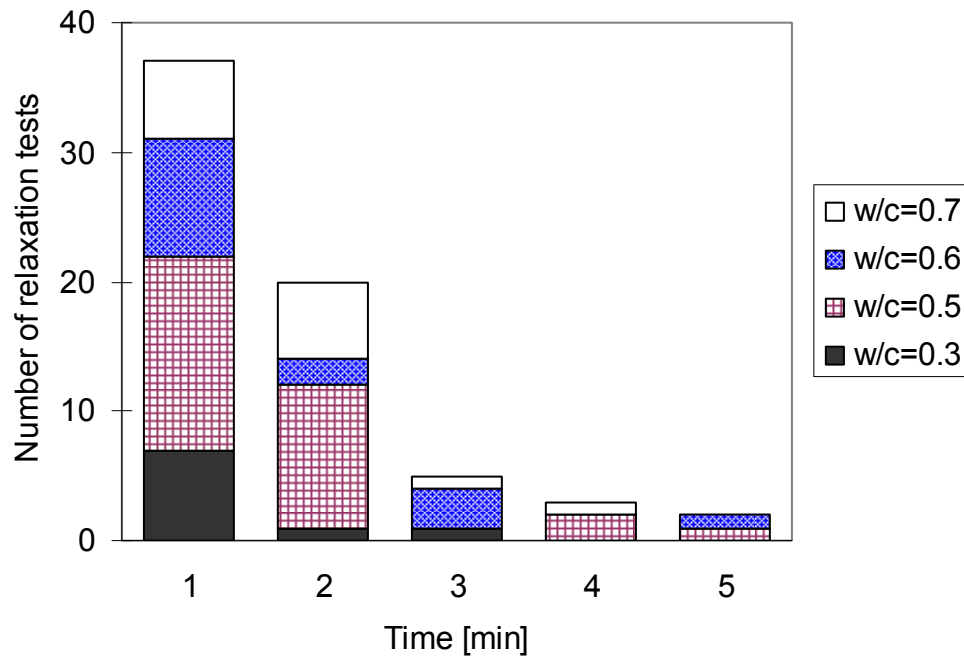
Figure 4.11. Number of the DT tests at 10% RH without measurable subcritical crack growth. The time refers to the time after which no measurable crack tip propagation was observed, which in most cases is when the second image was taken for the same region.
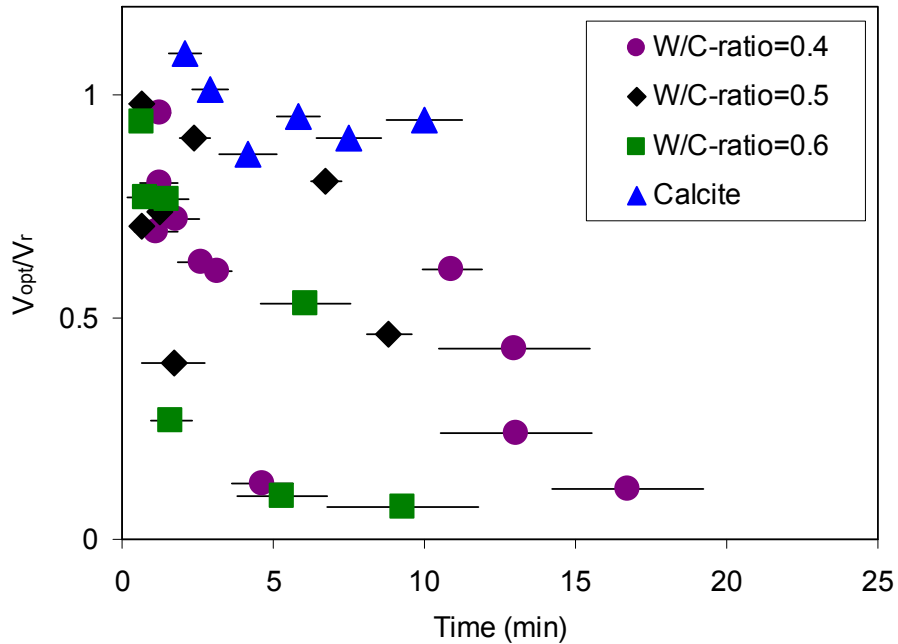
Figure 4.12. Ratio of subcritical crack velocities obtained from optical measurement (v_{opt}) and calculated from relaxation curves (v_r) as a function of time in DT tests for cement paste specimens at 10% RH, and for single-crystal calcite. *Horizontal error bar* indicates the time-span used for respective velocity calculation.

In 20 different relaxation tests at 10% RH we made 23 optical measurements of non-zero subcritical crack velocities. These velocities were compared with the average velocities calculated from the force-relaxation curve in the same test over the same time span. The ratio between these two velocities (v_{opt}/v_r) is plotted in Fig. 7b. The optically measured crack velocities for cement paste specimens at 10% RH are with no exception smaller than those calculated from the load-relaxation curves. Moreover, the ratio v_{opt}/v_r appears to decrease with increasing time. However, beyond this general statement, no regular evolution pattern can be identified. For comparison the results for subcritical cracking in calcite are plotted, showing that the ratio v_{opt}/v_r is close to unity as expected for a non-creeping material.

4.2.4. Optical studies at 90% RH (Stereomicroscope)

DT tests under wet conditions were performed on cement paste specimens under the stereomicroscope, where high-resolution ESEM imaging was not applicable. In all constant-displacement tests carried out at 90% RH, the propagation of the crack tip could be optically recorded, facilitated by DICM, at magnifications of 80 to 100×. In all tests, more significant crack propagation than at 10% RH was observed, except for w/c-0.5 series where crack tip regions were not successfully captured. An example showing the identified continuous crack propagation in cement paste specimens under optical microscope is presented in Figure 4.13. The crack and its growth can be observed through DICM as the region showing the highest pseudo-strain values (up to 0.01). The figure shows that the subcritical crack was growing after 45 s from the start of the test, propagated at relatively high velocity at the beginning and decelerated fast during the test. After 740 s (e.g. 1340 s), there was no significant movement of the crack tip being observed. The crack opening was increasing with the propagation of the crack.

The crack velocity as a function of time is given in Figure 4.13, for both optically measured values (v_{opt}) and those calculated from the relaxation curve (v_r). It can be seen that at the beginning, the difference between v_{opt} and v_r over the same time-span was not significant and was nearly equal up to about 2 min. The difference became more and more significant with increasing time, and v_r was higher than v_{opt}.
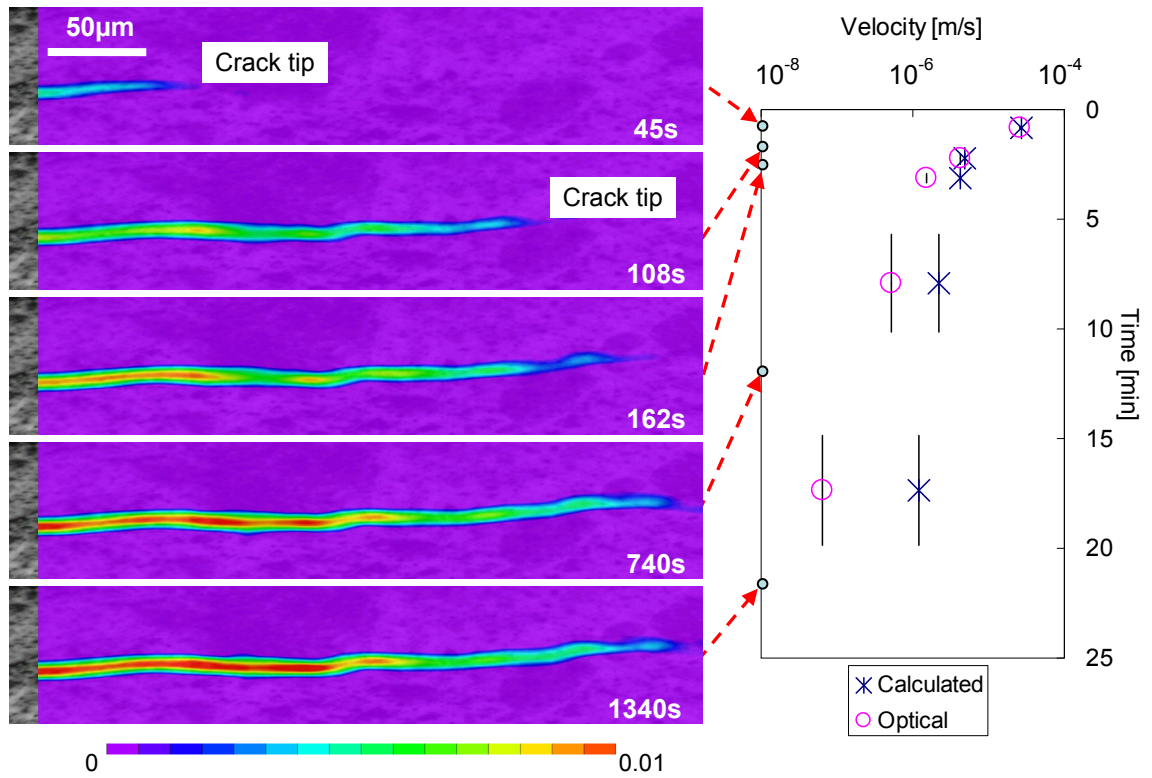
Figure 4.13. Digital image correlation (pseudo-strain field) of subcritical crack propagation (*left images*) and crack velocities (both *calculated* from relaxation curve, v_r, and *optically measured* from the DICM results, v_{opt}, from one DT test after 95 s under stereomicroscope at 90% RH. The w/c-ratio of specimen is 0.7. In *velocity-time* plot, the *vertical error bars* on each data point denotes the time-span for respective velocity calculation.
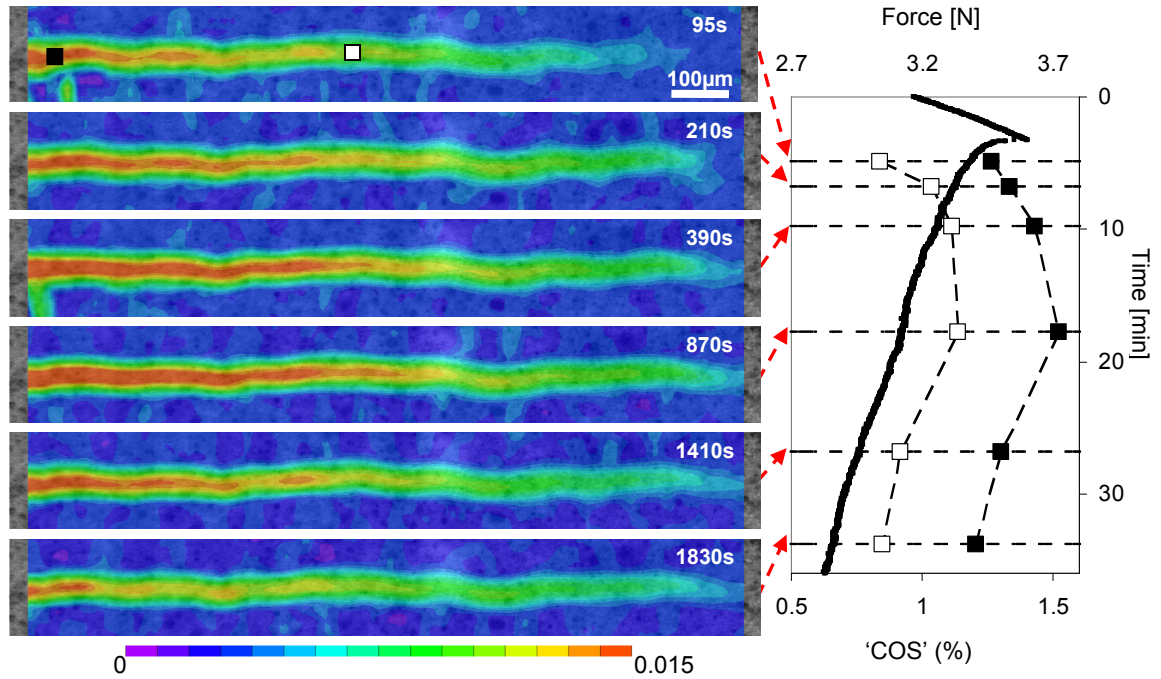
Figure 4.14. Digital image correlation (pseudo-strain field) of subcritical crack growth (*left images*) and measured load relaxation (*solid line in diagram*) from one double-torsion test under optical microscope at 90% RH. The w/c-ratio of specimen is 0.7. *Filled and open squares* show the crack opening strain (COS) at two locations along the crack as shown in the image after 95 s.

Another example of subcritical crack at 90% RH under optical microscope is shown with force-time curve in Figure 4.14. The crack tip was not propagating in the synchronous way as the measured relaxation. The crack tip decelerated rapidly and apparently stopped propagating (i.e. within the resolution limit, not able to observe distinguishable propagation) after 870 s, but the force-relaxation of the specimen continued. A COS of 0.1 corresponds to a crack width of approximately 0.6 μm in this study. And the crack opening given as the crack opening strain (COS), also increased at first but started to decrease after 870 s. At high velocities, this effect was less significant than the opening of the crack that was due to fast crack propagation.
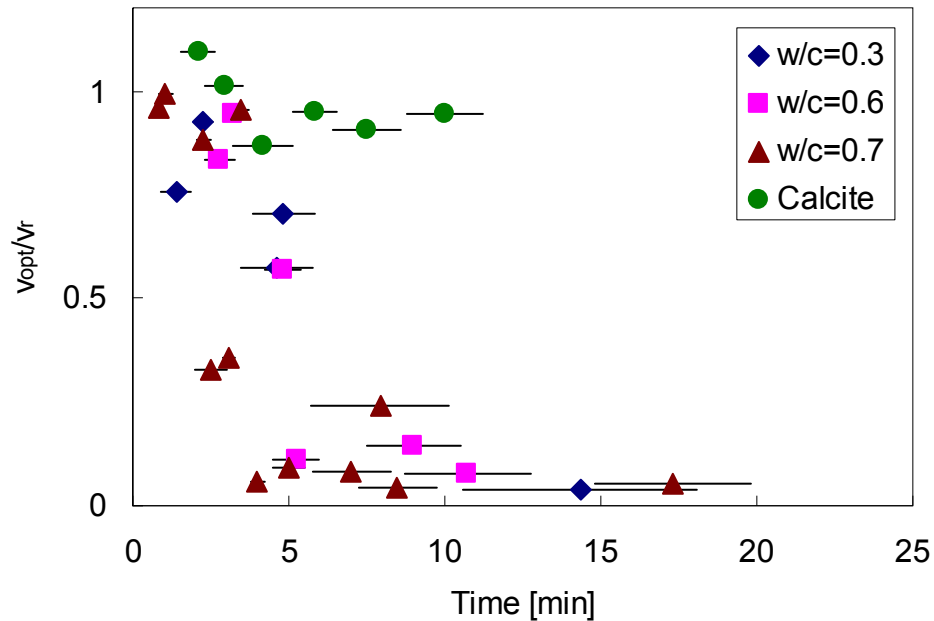
Figure 4.15. Ratio of subcritical crack velocities obtained from optical measurement (v_{opt}) and calculated from relaxation curves (v_r) as a function of time in DT tests for cement paste specimens at 90% RH, and for single-crystal calcite. *Horizontal error bar* indicates the time-span used for respective velocity calculation.

The v_{opt}/v_r ratio as a function of time for different specimens is presented in Figure 4.15. Each pair of velocities was obtained over the same time-span. Single crystal calcite showed close-to-unity ratios for two series of separately obtained velocities. As mentioned previously, this is expected for non-creeping materials. The cement paste specimens showed decreasing ratio of v_{opt} to v_r, with increasing time. Moreover, the crack tip is continuously propagating to new locations. Apart from this, the effect of w/c-ratio on the velocity ratio was not pronounced. The trend of the v_{opt}/v_r ratio appears to decrease in a similar manner over time for specimens with different w/c-ratios.

4.3. Creep-induced relaxation

4.3.1. Uncracked double-torsion specimens

The force (P) to maximum force (P_o) ratios as function of time for specimens tested at 10 and 90% RH were presented in Figure 4.16 and Figure 4.17. In general, the force decrease is smooth, for both normalized curves of apparent SCG from DT tests (denoted as DT curve) and those of creep-induced relaxation from CR tests. The decrease of P/P_o was the close to each other for specimens with different w/c-ratios at the same relative humidity, both for the DT curves and the CR curves. At 10% RH, the DT and the CR curves show small differences (within 1%) of the P/P_o ratio drop, and both decreased in an apparently exponential way.
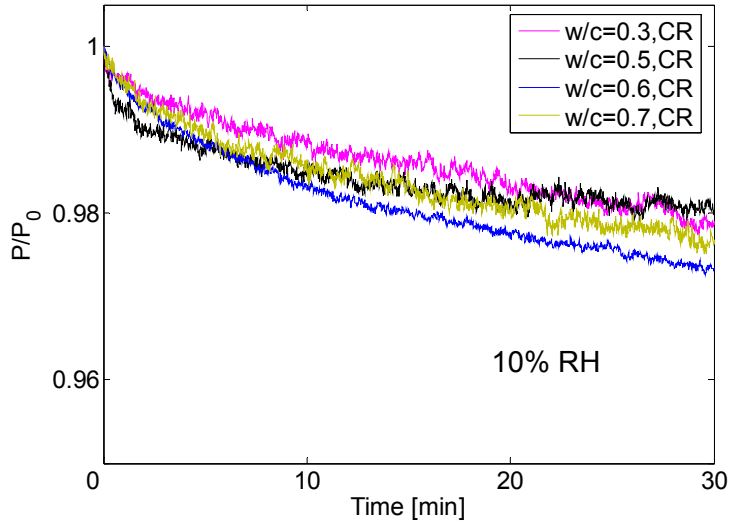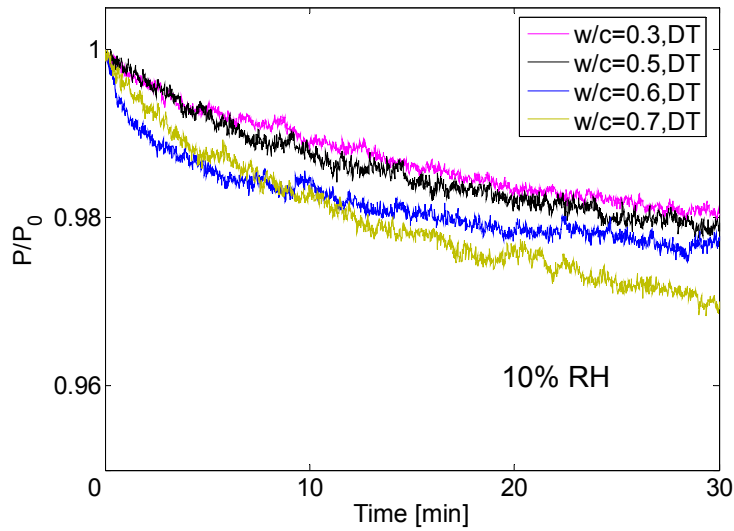
Figure 4.16. Normalized force-time curve for cement paste specimens showing (a) creep-induced relaxation (CR) tests and (b) relaxation from DT tests at 10% RH.
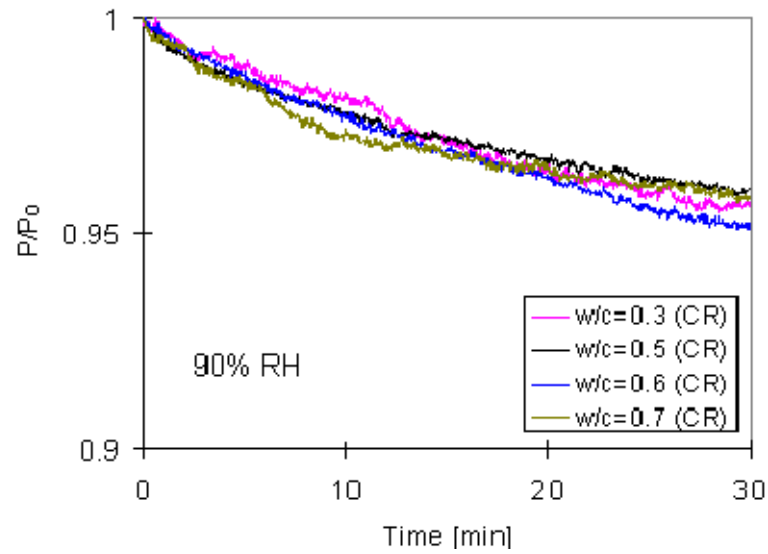
(a)
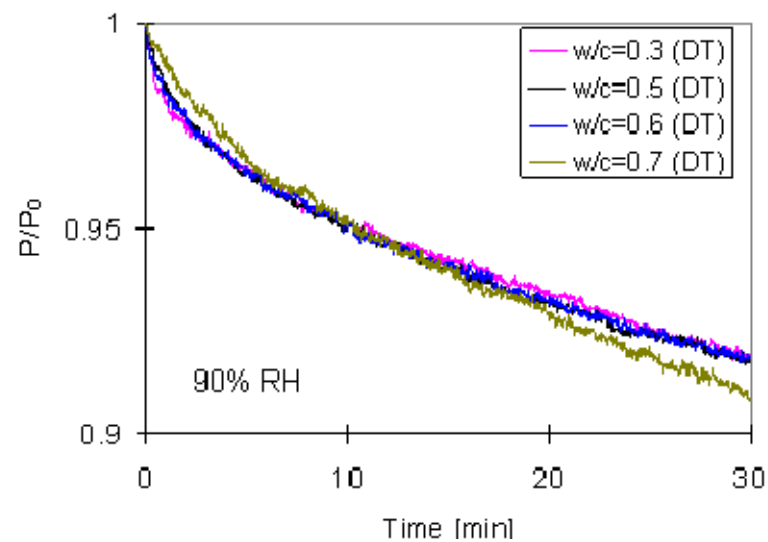
(b)

Figure 4.17. Normalized force-time curve for cement paste specimens showing (a) creep-induced relaxation (CR) tests and (b) relaxation from DT tests at 90% RH.

At 90% RH the DT and CR curves decreased faster than those at 10% RH for respective specimens, consistent with the fact that both subcritical cracking and creep are more significant at higher water content for hardened cement pastes. Apart from this, there is a clear difference between the DT and CR curves. The DT curves decreased faster, with a final cumulated decrease approximately double that of the CR curves.

106

4.3.2. Beam-bending tests

The creep behavior was also examined through three-point bending test on cementitious materials. The ratio of force (P) to maximum force (P_{max}) is presented as a function of time and the residual forces (P_{fr}) at fracture are listed in Figure 4.18. The relaxation curves show a generally smooth decrease of force, consistent with creep-induced relaxation and also resembling that of subcritical crack propagation (e.g. the force-time curve in Figure 4.1) as well. The residual peak forces for the specimens equilibrated and tested at 10% RH were 30 to 40% higher than those equilibrated at 95% RH (see table in Figure 4.18). Considering the load level (P/P_{fr}), that was 0.46 ± 0.02 and 0.34 ± 0.02 for specimens at 10 and 95% RH, respectively. The results show that cement paste specimens with the thickness of 2 mm exhibited significant relaxation without cracking under the given conditions. The degree of relaxation (creep-induced) was higher when the relative humidity was higher. In addition, no significant effect of w/c-ratio on the relative relaxation (i.e. P/P_{max}) in the bending tests was observed.

The creep-induced relaxation tests on uncracked DT specimens and beam specimens generally show the same trend: the effect of relative humidity was pronounced with the degree of the relaxation increasing with RH. The effect of w/c-ratio on the relaxation was not evident, compared to that of RH.
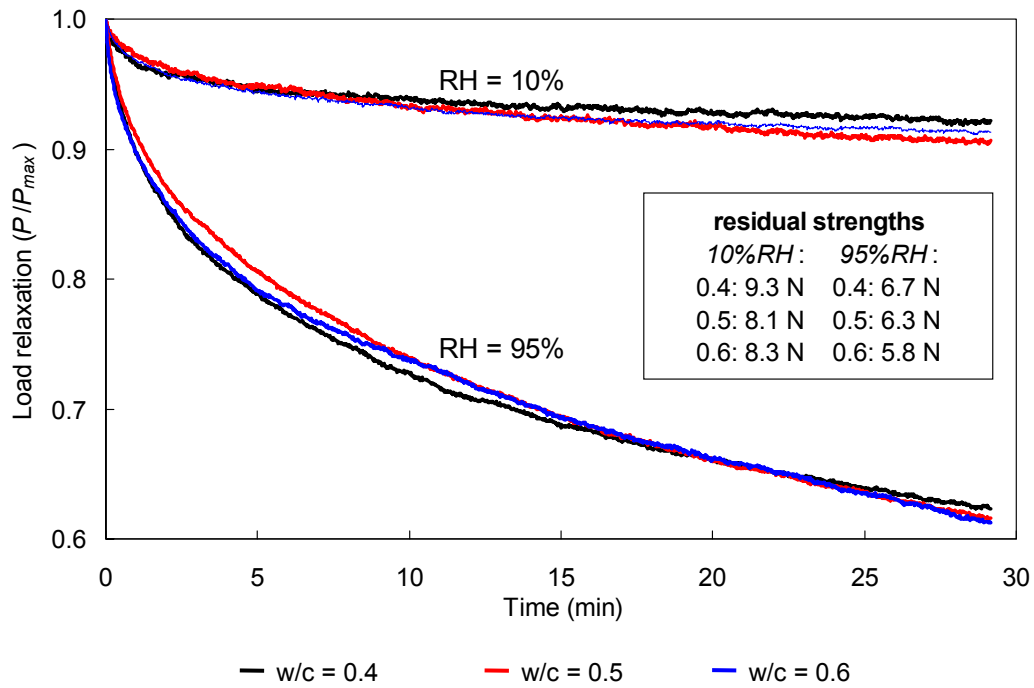
Figure 4.18. Normalized creep-induced relaxation curves and residual forces at fracture of uncracked, unnotched specimens from three-point bending test.

4.4. Self-healing tests

The healing occurred in the subcritically formed cracks in hardened cement pastes result from precipitates from the environment or the hydration productions from internal anhydrates. The example of these two products is presented in Figure 4.19. The subcritical crack width of about 10 μm here allowed the healing to take place. The chemical substances (e.g. $Ca(OH)_2$ or $CaCO_3$) from the environment formed layers of precipitates covering the crack surfaces, and led to a certain degree of crack closure as shown in Figure 4.19a. The precipitates are identified in BSE images as layers showing different grey level from the matrix materials and the crack was closed from two sides at that part. Apart from this, unhydrated cement particles can also lie in the way of the crack path as shown in Figure 4.19b.
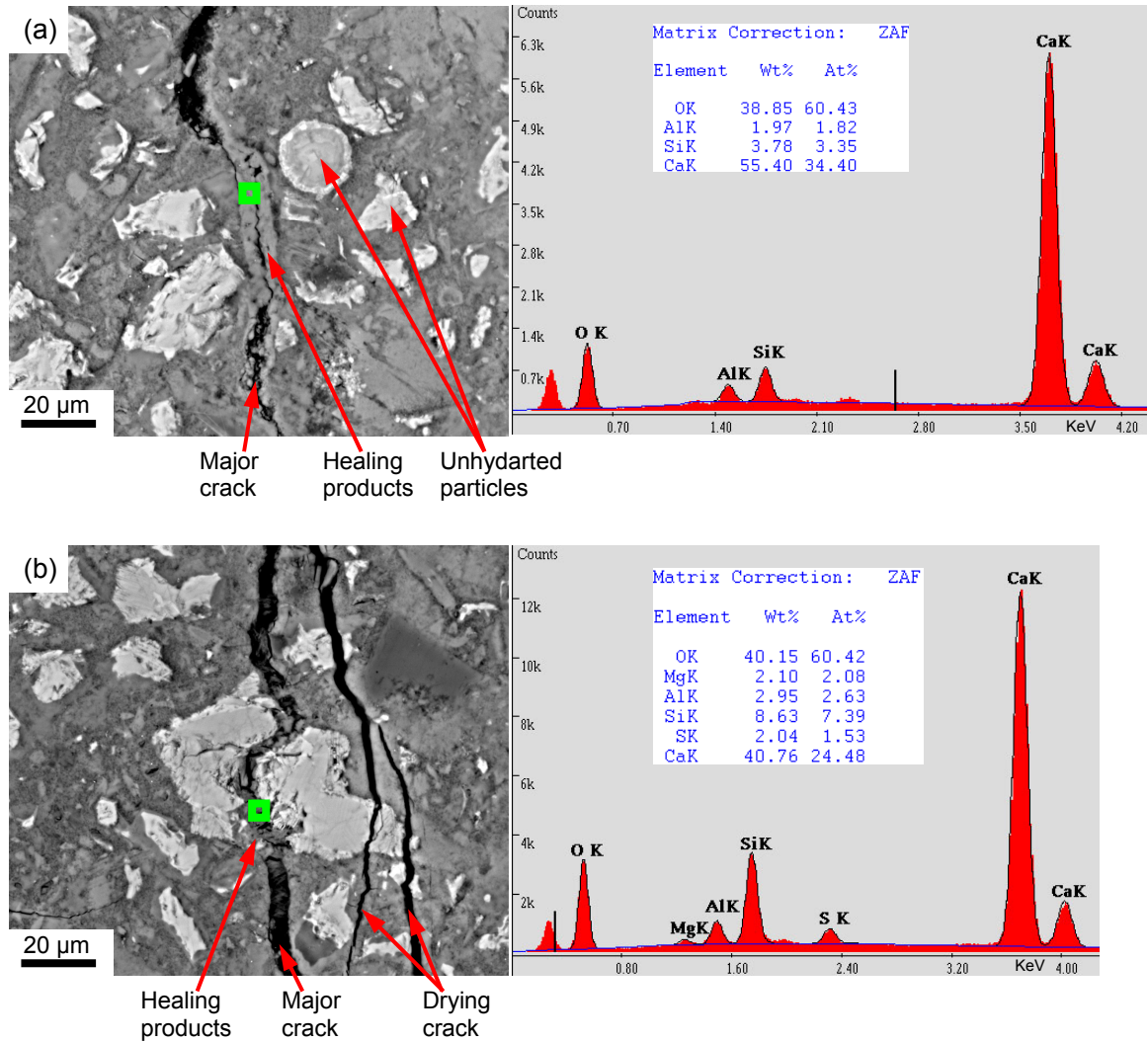
Figure 4.19. Backscattered electron images showing different types of healing for subcritical cracks: (a) healing through precipitates (e.g. $Ca(OH)_2$) or $CaCO_3$ from surrounding environment and Energy-dispersive X-ray spectroscopy (EDX) element analysis of the precipitates; (b) healing through hydration of unhydrated particles in the cement paste specimen with w/c-ratio of 0.3 and EDX element analysis of the hydration products. The healing period is 1 month of wet-and-dry cycles.

The cracked unhydrated cement particle was healed by the reaction products of its own, while other part of the crack that was without unhydrated particles stayed unhealed. As a comparison, the side cracks (e.g. drying cracks) introduced after the healing period, as

shown in Figure 4.19b, also intersected unhydrated particles but had no precipitates or hydration products inside.

The re-tested specimens with w/c-ratio of 0.7 showed self-healing of the subcritical cracks mainly through precipitates. The healing was more significant (i.e. closure of the crack) where the crack opening width is smaller. Examples of the ESEM images are presented in Figure 4.20 and Figure 4.21. The previously-formed subcritical crack, where the crack opening width was not above 20 μm, was healed by precipitates (e.g. $Ca(OH)_2$ or $CaCO_3$, see Figure 4.20a, c, d and Figure 4.21). And the structure of the filling precipitates was more porous than the matrix materials. The previously-formed crack surfaces were covered with the precipitates, while the boundaries between them can still be observed (see Figure 4.20d). After being re-cracked in DT test, the newly-appeared subcritical cracking followed the already-existed crack path and propagated through the healing materials (Figure 4.20a and c). The subcritical crack showed lower degree of healing and the crack surfaces remained separated from each other, where its crack opening width was above 50 μm.
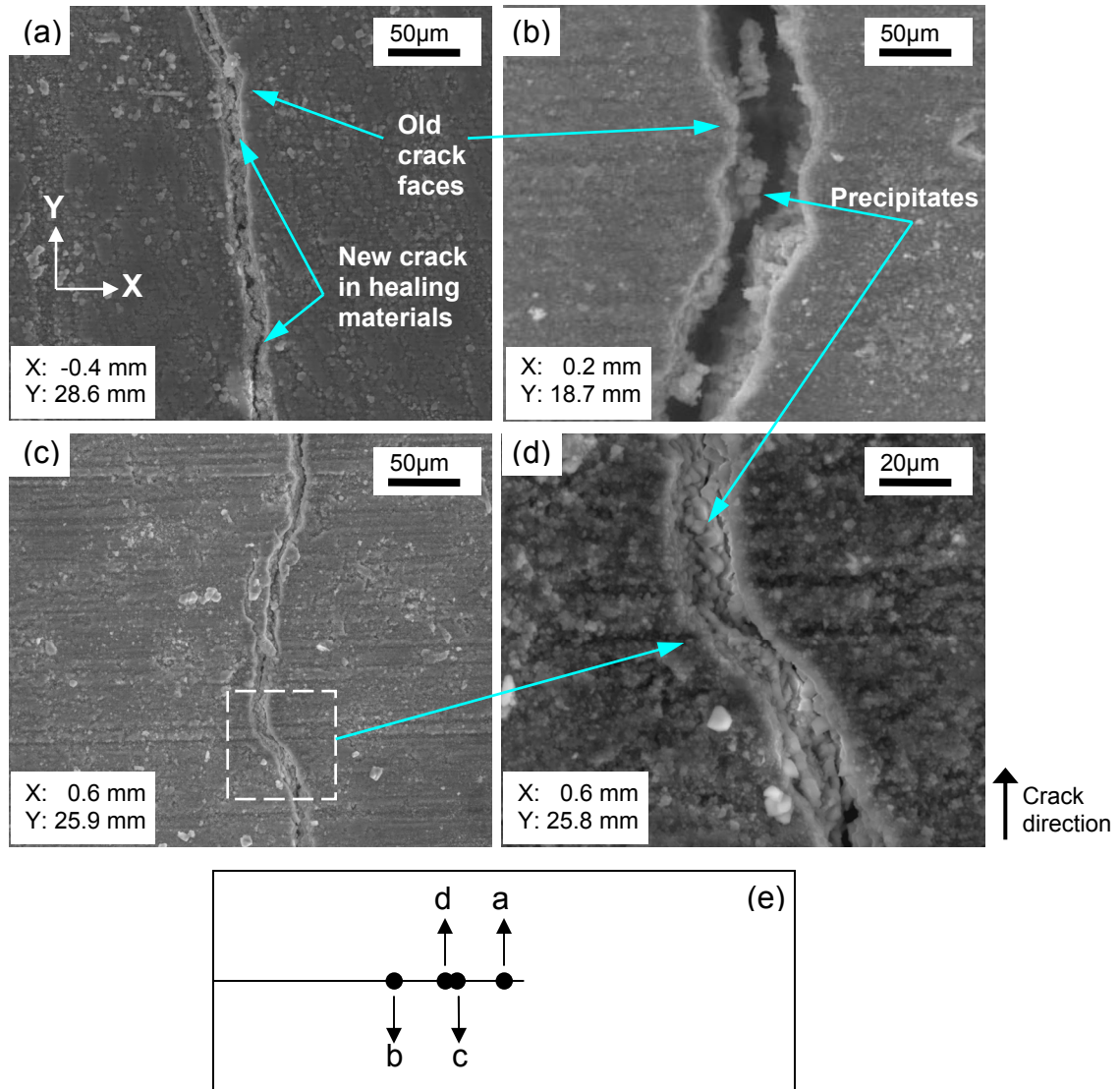
Figure 4.20. ESEM images (SE) showing the healing effect on subcritical cracks in specimens with w/c-ratio of 0.7. (a), (c) and (d) shows the small crack-width original subcritical cracks with new subcritical cracks formed during DT test after the healing period. (b) shows a crack with large opening with precipitates inside. X and Y denote the coordinates of the image center (for the loading point: X = 0 mm, Y = 0 mm). (e) is the schematic illustration of the relative position of each imaging area in the DT specimen along the old subcritical crack. The images were taken during or immediately after DT tests and the specimens were not subjected to any subsequent treatment (e.g. grinding or polishing).
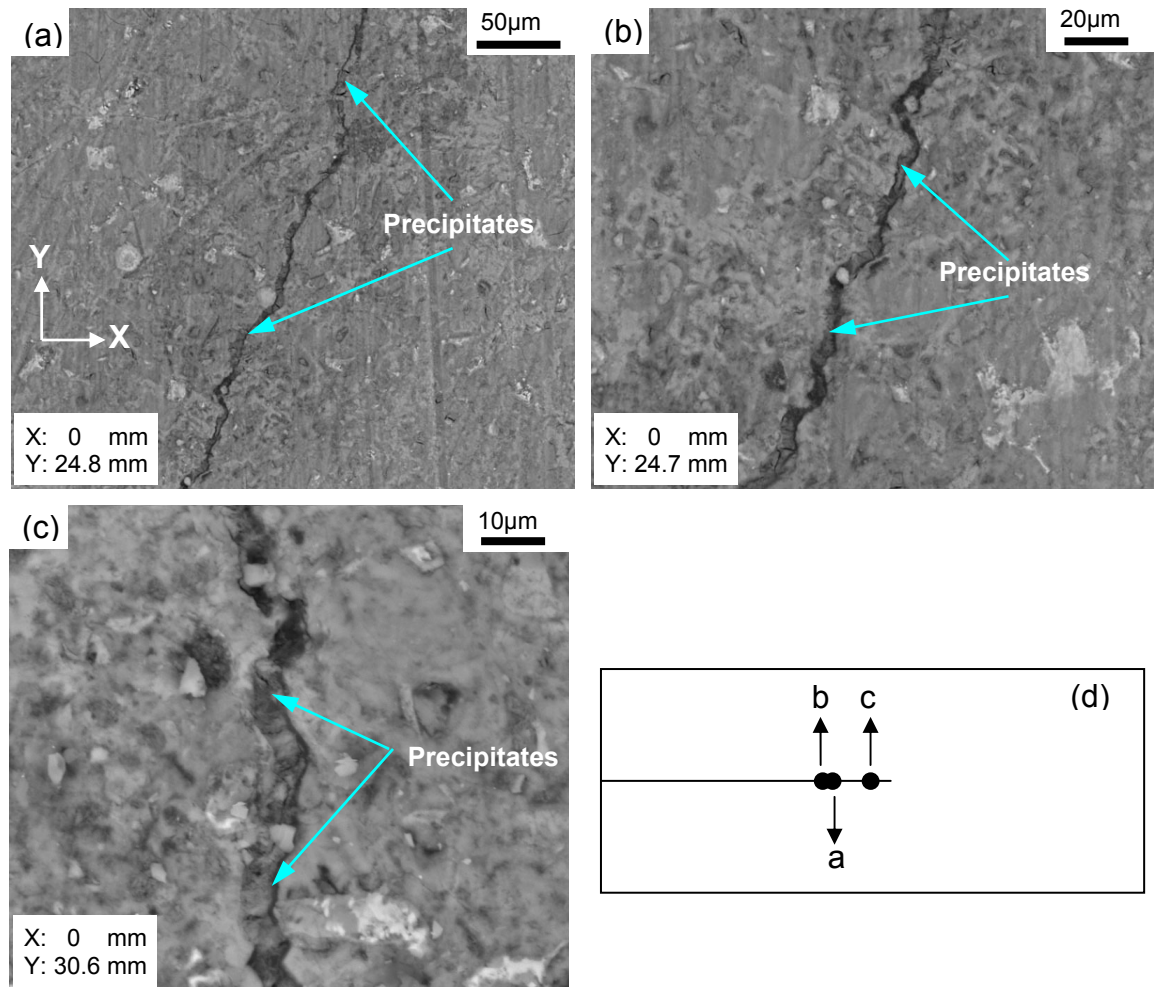
Figure 4.21. ESEM images (BSE) showing the healing effect through precipitates on the subcritical cracks in specimens with w/c-ratio of 0.7. (a), (b) and (c) are ESEM images. X and Y denote the coordinates of the image center (for the loading point: X = 0 mm, Y = 0 mm). (d) is the schematic illustration of the relative position of each imaging area in the DT specimen along the old subcritical crack. The specimens were impregnated with epoxy.

The re-tested specimens with w/c-ratio of 0.3 showed the self-healing of the subcritical cracks. The ESEM images for a re-tested DT specimen with w/c-ratio of 0.3 are presented in Figure 4.22 and Figure 4.23. The existed subcritical crack propagated along the centerline of the specimen (i.e. with the X-coordinate close to 0), to a distance of

about 17 mm (see Figure 4.22a). For most part the crack width was less than 5 μm and this width is smaller than that of specimens with w/-ratio of 0.7.

Being re-tested after the healing period, the specimen showed newly-formed subcritical crack that deviated from the original crack path (Figure 4.22b and c, note that not all newly-formed cracks deviated from old crack paths). The old crack path was not visible on the specimen surface, e.g. due to tight crack opening and healing. The new subcritical crack deviated significantly from the centerline to the new location with X-coordinate of -1.2 mm (Figure 4.22b). In BSE images, with the surface layer (about 0.1 mm) of the specimen being removed, the healed subcritical crack (Figure 4.23a and b) and the newly-formed one can both be observed (Figure 4.23b).
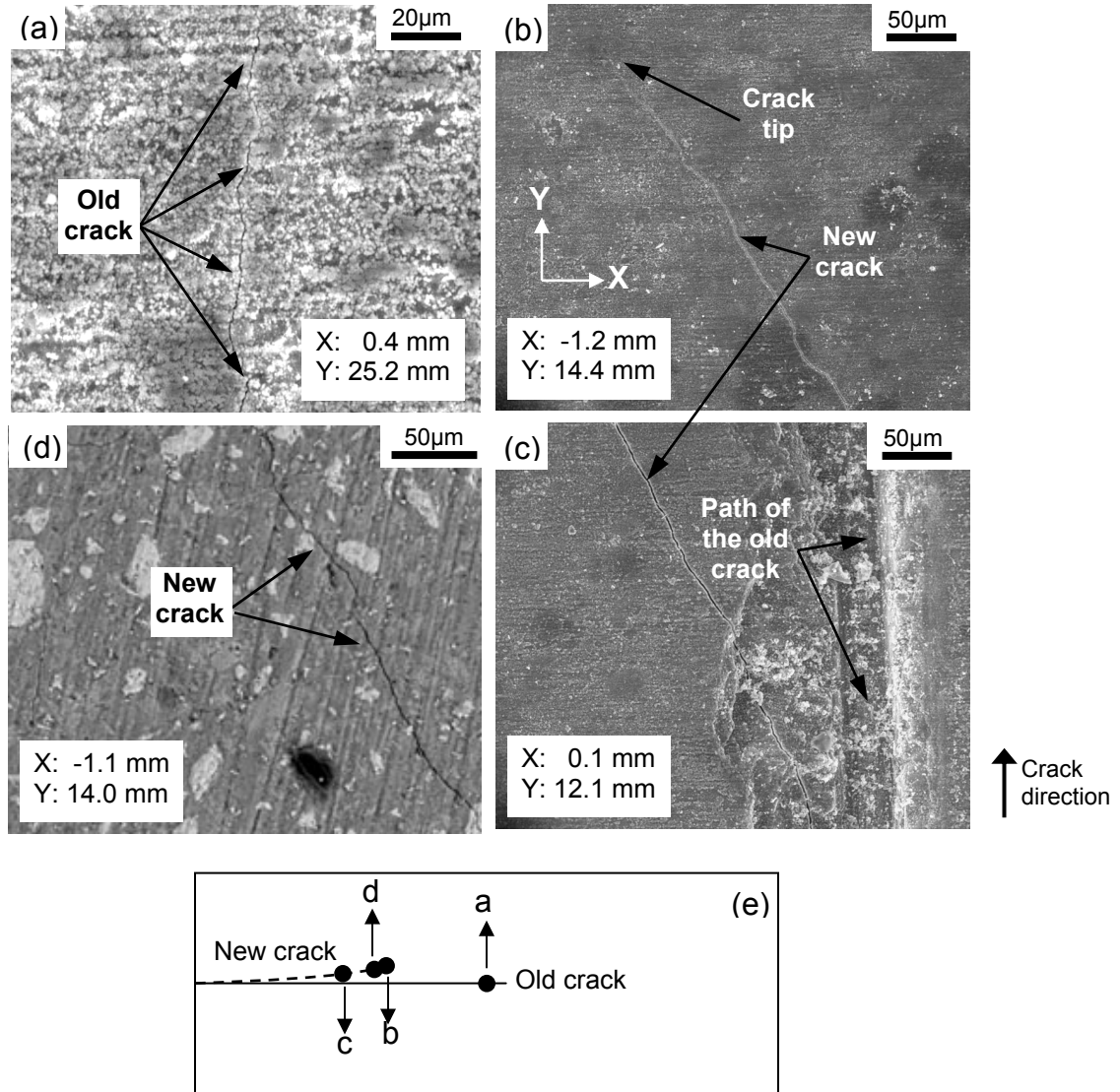
Figure 4.22. ESEM images (SE and BSE) showing the healing effect on subcritical crack in specimens with w/c-ratio of 0.3. (a) shows the original image of the old subcritical crack along the centerline of the specimen. (b) and (c) show the SE images for the newly formed subcritical crack during DT test after the healing period. (d) shows the BSE image for the newly formed crack. X and Y denote the coordinates of the image center (for the loading point: X = 0 mm, Y = 0 mm). (e) is the schematic illustration of the relative position of each imaging area in the DT specimen along the old/new subcritical crack. The ESEM images were taken during or immediately after DT tests and the specimens were not subjected to any subsequent treatment (e.g. grinding or polishing).
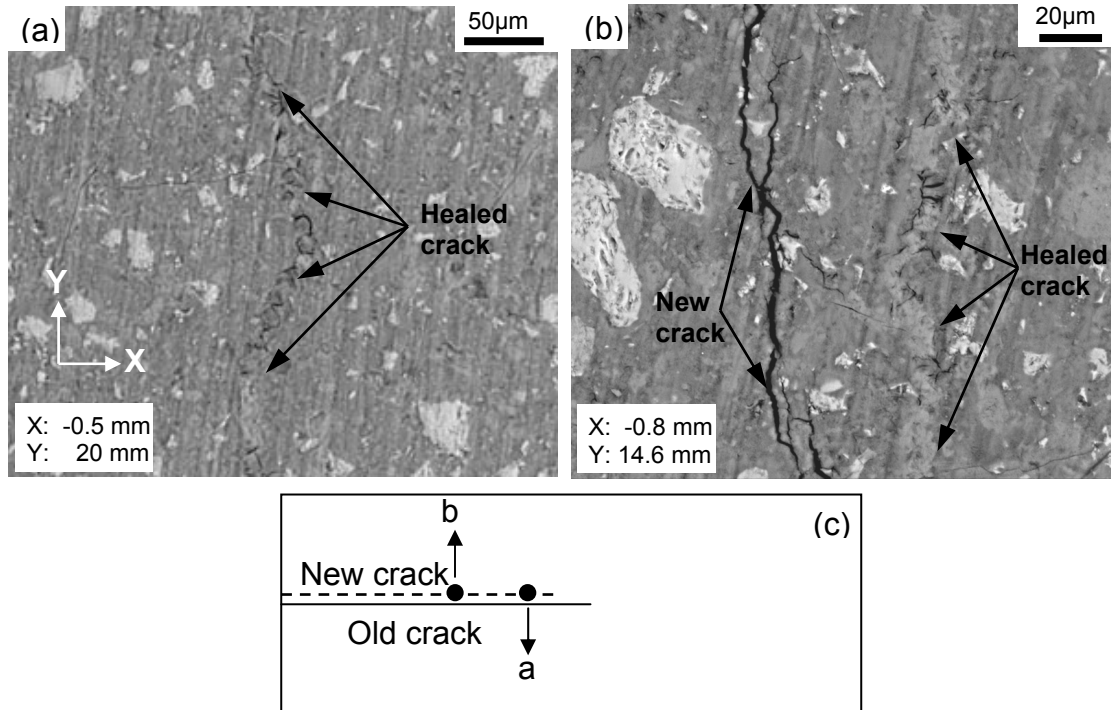
Figure 4.23. ESEM images (BSE) showing the healing effect on subcritical crack in specimens with w/c-ratio of 0.3. (a) and (b) are ESEM images. X and Y denote the coordinates of the image center (for the loading point: X = 0 mm, Y = 0 mm). (c) is the schematic illustration of the relative position of each imaging area in the DT specimen along the old/new subcritical crack. The specimens were impregnated with epoxy.

The *K-v* diagram for the specimens tested at 10% RH, before and after healing, is presented in Figure 4.24. The crack regions were examined inside ESEM by tracking the crack growth and compared with previous recordings, to confirm if new crack path occurred or not. With w/c-ratio of 0.7, the specimens tested before healing showed lower range of K_I, but the decrease was relatively small. For specimens with w/c-ratio of 0.3, the results were consistent with the optical observation. The self-healed specimens showed identical capability to resist subcritical cracking. The *K-v* curves showed even higher K_I range than when the specimens were uncracked. Specifically, the *K-v* curve with K_I range close to 6×10^5 Nm$^{-3/2}$ was corresponding to the example shown in Figure

4.22b and c. The significantly higher (nearly 20% higher) K_I did not lead to cracking through the previous crack path, but a new crack path that deviated from the centerline.
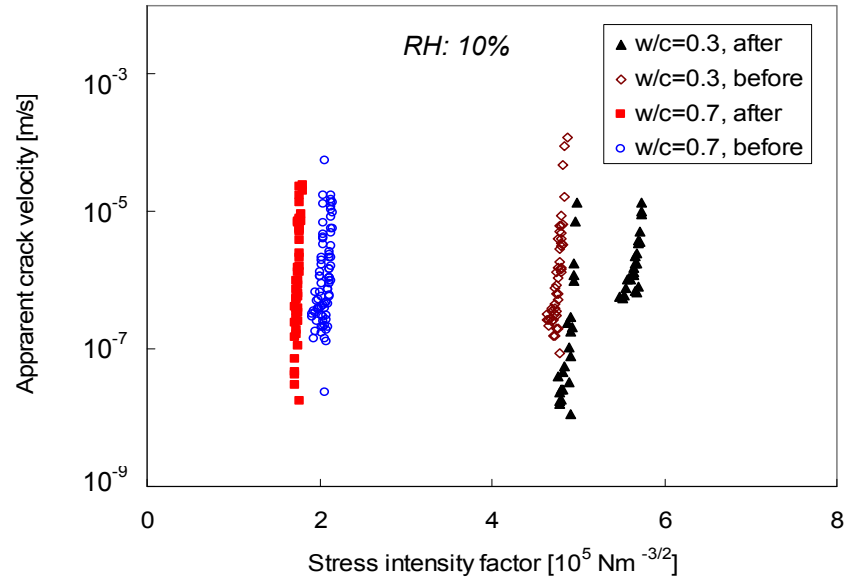
Figure 4.24. The *K-v* diagram for cement paste specimens tested at 10% RH. "before" means the tests before submersion in limewater. "after" means the tests after submersion. Each of the 4 data series comprises 3 individual test results.

CHAPTER 5 Data analysis and Discussion

5.1. Single-crystal calcite

Through the DT test, the micro-testing device has been demonstrated to able to produce calculated subcritical velocities that are in general agreement with the optically measured ones for single-crystal calcite specimens. There are very small differences between these values mainly due to the inaccuracies in measurement (e.g. force readings). The consistency between the two sets of measurements also indicates that other possible time-dependent phenomena such as creep did not played a significant role in the measured relaxations of calcite. Moreover, no evident erroneous relaxation resulting from the testing device can be identified. Thus, for materials behaving linear-elastically or for those exhibiting negligible viscoelasticity when stressed, the constant-displacement test performed on the micro-testing device can be used to study the subcritical crack growth by the DT method.

For calcite specimens, the subcritical crack growth was observed at conditions of low water content (e.g. 1% RH as in this test). Under such conditions, the reactive species (i.e. water molecules) were very low in the environment. The materials that still undergo subcritical cracking can be explained by 'atomistic' mechanisms, involving thermally-activated processes as suggested by early studies (Atkinson and Meredith, 1987). In such cases, the atomic bonds at the tips of cracks are highly stressed and can be displaced or ruptured by thermal fluctuations. The resulting crack growth proceeds in a subcritical way (Wiederhorn et al., 1974). The governing mechanism was, at early times, proposed to be due to dissolution (Atkinson, 1984). However, in my study it is suggested that the

subcritical cracking in calcite is not necessarily governed by moisture-assisted processes. Under the condition of high water content (e.g. 100% RH) calcite crystals become much more susceptible to subcritical cracking (Røyne et al., 2011). The measured crack velocities in calcite can be predicted by reaction rate theory, but the specific subcritical crack growth mechanisms at low or high water content were not identified (Røyne et al., 2011).

5.2. Creep-induced relaxation in cement paste

Significant relaxation has been observed in the beam-bending tests and in the experiments on DT specimens, without cracking-induced relaxation (see Chapter 4.3). The degree of relaxation (creep-induced) increased with higher relative humidity. This is in agreement with previous studies for the effect of relative humidity on creep in cementitious materials (Bažant et al., 1976; Wittmann, 1973; Neville et al., 1983). The diffusion of water molecules in the cement pastes contributes to the mobility of the solid phase materials. Higher water content makes the solid phases more mobile and therefore leads to higher degree of creep (Bažant and Chern, 1985). Alternatively, models for creep in cementitious materials have also been proposed, such as dispersed nano/microcracking at higher stress-levels (see Chapter 2.3.5). This influence of microcracking was observed in concrete specimens from tensile creep tests when stress/strength level was higher than 50% (Kamen et al., 2009). One could therefore speculate that these microcracks grow subcritically and contribute to the material rearrangement that macroscopically is measured as creep.

In these experiments no significant effect of w/c-ratio on the relative relaxation (i.e. P/P_0) in the beam-bending tests was observed. In fact, a weak dependence of w/c ratio on the magnitude of creep was observed in concrete materials after a relatively long period (i.e. in terms of days) of loading (e.g. Østergaard et al., 2001). However, with the test time only being about 30 min in this study, the relative influence of w/c-ratio on the relaxation is too small to be identifiable. It therefore indicates that the relative effect of material density on creep-induced relaxation is not significant in short-term tests but care should be taken on this effect for long-term tests.

5.3. Fracture toughness

In general, for hardened cement paste, the fracture toughness is higher when the w/c-ratio is lower (see Figure 4.6). In HCP of the same age, the w/c-ratio determines the porosity of the paste. Higher porosity, as inherent flaws in hardened cement paste, tends to weaken the strength of the material (e.g. function as stress raisers) and in turn lower K_{Ic}. This is consistent with other studies (Prokopski and Langier, 2000; Brown and Pomeroy, 1973). Moreover, the specimens at 10% RH show higher values of K_{Ic} than those at 90% RH with the same w/c-ratio, indicating that water content not only affects the subcritical cracking but also the fracture toughness. This behavior is also suggested by previous studies performed through fast loading experiments (Beaudoin, 1982; Rossi and Boulay, 1990; Bažant and Prat, 1999) and the table in Figure 4.18. Specifically, this may be due to the stress of adsorbed water exerted to the C-S-H layers, leading to disjoining pressures. The pressure increases with higher internal water content and

weakens the molecular bonding between C-S-H layers. The fracture energy of the cement paste is consequently lowered through the weakening of the C-S-H phase.

5.4. Effect of creep in double-torsion cracking experiments

5.4.1. Observations

The DT tests carried out at both 10% and 90% RH show that the measured specimen relaxation was not resulting purely from the subcritical cracking in the specimens. Optically it was observed that the crack growth stopped, while the specimen relaxation continued. This is strong evidence that creep-induced relaxation played an important role in the DT-test. The question is now, how significant was the contribution of creep in the measured stress-relaxation at 10% and 90% RH. Creep-induced relaxation was shown to increase significantly with increasing RH. However, since these relaxation tests were not carried out at exactly the same stress-level (i.e., load level (P/P_{fr}), that was 0.46 ± 0.02 and 0.34 ± 0.02 for specimens at 10 and 95% RH, respectively.), it is not directly clear how much difference in creep there was at 10 and 95% RH. Also, as has been shown in many other materials, the degree/velocity of subcritical cracking is also expected to be strongly dependent on the relative humidity. It is therefore not directly obvious in the traditional K-v diagrams that how significant the relative humidity influences creep and subcritical cracking.

The normalized double-torsion (DT) and creep-induced relaxation (CR) curves show small differences (within 1%) at low water content of 10% RH, and both decreased in an apparently exponential way. However, it should be noted that creep-induced relaxation occurs when the samples are subjected to external forces. In contrast, subcritical cracking

120

depends on the threshold stress intensity factor (i.e. minimum requirement for SCG to occur) for the materials at crack tips. Moreover, due to high heterogeneity (e.g. unhydrated cement grains) of the hardened cement pastes, crack arrest could inhibit subcritical cracking. Therefore, the measured relaxations from DT tests should always contain a creep-induced part and, conditionally, also an SCG-induced part (denoted as SCGR) in various proportions. Consequently, the small differences between DT and CR curves indicate that at 10% RH the measured relaxation could be mainly due to creep, not SCG. This is consistent with the ESEM observations in this study which shows that the SCG was hardly observed during much of the duration of each DT test, for specimens with different w/c-ratios at 10% RH. The high apparent subcritical crack indices (n-values) obtained for the specimens (see Figure 4.7) also suggest a rapid deceleration of the subcritical cracking and consequently the possible crack arrest. The remaining relaxation is therefore resulting from creep. The creep also helps to suppress the subcritical cracking by relieving the stresses in the materials around the crack tip, leading to a more rapid decrease of subcritical crack velocity.

At high water content of 90% RH, the difference between normalized double-torsion and the creep-induced relaxation curves indicates that, besides the creep-induced process which contributed to part of the relaxation, cracking (i.e. subcritical) also contributes to the force drop in DT curves. We may add that the existence of subcritical cracking is supported by the DT tests at 90% RH under optical microscope in this study (see Chapter 4.2.5), which show slow crack growth in the cement paste specimens. Therefore, for hardened cement pastes at 90% RH, the subcritical cracking and creep-induced relaxation both contribute to the measured relaxation curves from DT tests.

121

Moreover, in short-term tests (i.e. relative to long-term tests that last for days) the decrease of P/P_o does not depend much on the w/c-ratio, both for the DT curves and the CR curves (also see Chapter 5.2). However, as shown in Figure 4.18, the relative humidity plays a much more significant role in the relaxation (creep-induced) of the stressed materials. This is compatible with the claim that relaxation takes place mainly through displacement of C-S-H sheets (as the binding phase), which is dependent on the interlayer water content (Tamtsia and Beaudoin, 2000; Alizadeh et al., 2010).

5.4.2. Empirical separation of creep and cracking in DT-test

In order to study the effect that is due to subcritical cracking in the specimens, an empirical approximation was made to try to separate the SCG-induced relaxation and creep-induced relaxation from the DT measurements. The recorded P/P_0 drop in DT curve is assumed to be the addition of those of the SCGR and CR curves. This treatment renders the idea of the superposition principle proposed for calculating creep at variable stresses, which states that different mechanical responses of a viscoelastic material are independent of each other (Bažant, 1998). The approximation is expressed as following:

$$1-(\frac{P(t)}{P_0})_{DT} = (1-\frac{P^{'}(t)}{P^{'}_0})_{CR} + (1-\frac{P^{''}(t)}{P^{''}_0})_{SCG} \qquad (5.1)$$

where P/P_0, $P^{'}/P^{'}_0$ and $P^{''}/P^{''}_0$ are the *force to peak force* ratios in DT, CR and SCG force-time curves, respectively. In this approximation the possible term for the interaction between the SCGR and CR was not considered in order to simplify the calculation. Although this treatment is empirical, it is expected to approximate the SCGR curves well. An example showing the procedures for separating the CR from the DT curve is

122

presented in Figure 5.1. The DT curve and CR curve are best-fitted first. The fitting

curves are then used to obtain the SCGR curve according to Equation 5.1. The

normalized SCGR curve is then transformed back to force-time curve, using the peak

force in the DT curve as P_0. Note that the SCGR curves continue decreasing over time

(e.g. subtracted SCG curve in Figure 5.1b), even after when the subcritical cracking

apparently stopped later (e.g. from about 20 to 30 min). This might be explained as the

difference between the specimens used in DT tests and creep-induced relaxation tests.

For DT specimens with sharp cracks, the degree of creep is expected to be higher (higher

stress concentration around a crack tip with smaller curvature radius) than in creep tests,

therefore cannot be subtracted completely from the total relaxation curves. The SCGR

force-time curve is then used to derive $K\text{-}v$ diagram and obtain subcritical crack index,

which functioned as the real SCG approximates. The approximation is performed only on

tests at 90% RH. At 10% RH, the CR curves could not be distinguished from the DT

curves, so that all of the relaxation is attributed to the effect of creep.
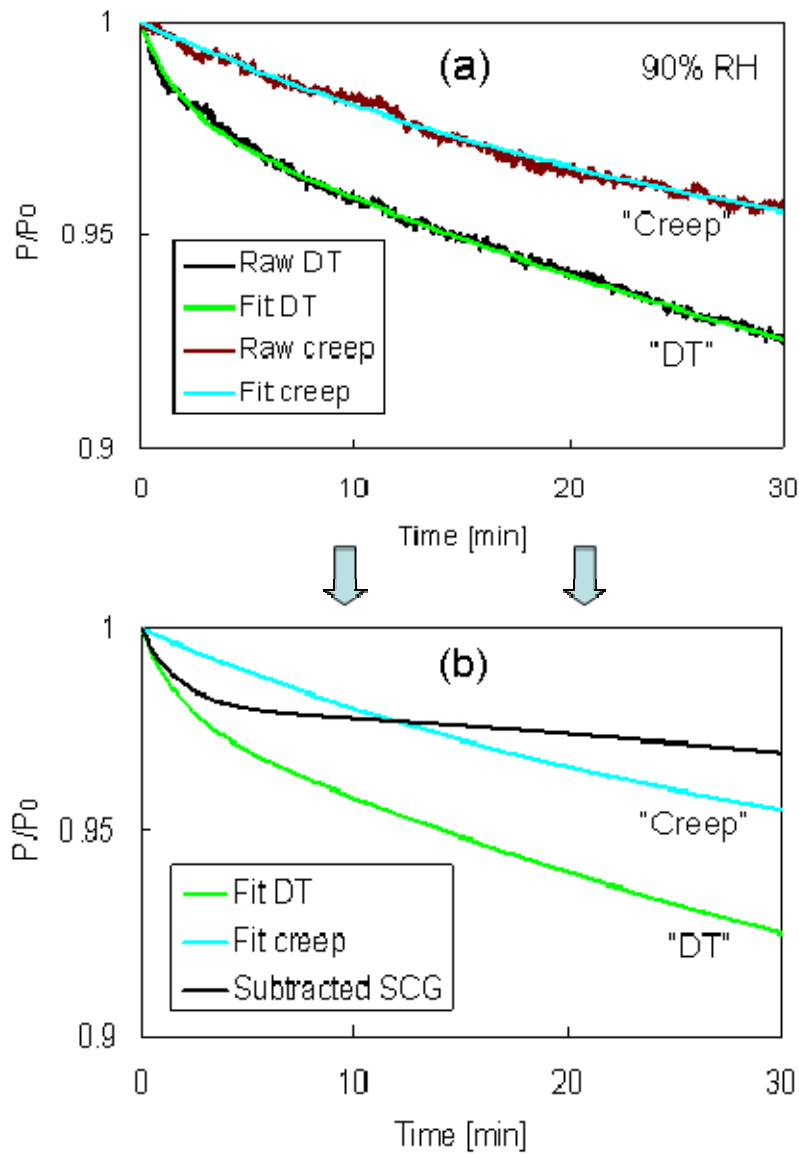
Figure 5.1. Illustration of the separation of creep-induced relaxation from the measured total relaxation curve. 'Raw' denotes raw data, 'Fit' denotes fitting curve, 'DT' denotes DT measurement, 'creep' denotes creep-induced relaxation and 'subtracted SCG' denotes the subtracted relaxation part. Test performed at 90% RH.

5.4.3. Adjusted *n*-values

After the approximation for obtaining adjusted SCG curves, the *n*-values for DT tests

at 90% RH are re-calculated. The crack velocities in Figure 4.4 and Figure 4.5 are based

on those obtained from optical measurements to extract the adjusted *n*-values. The *n*-values from original DT tests (original), optical measurements (optical) and creep-induced relaxation separation (adjusted) are presented in Figure 5.2. As shown, the *n*-values form the optical measurements and creep-separated approximations are both higher than the values obtained from original DT curves. More importantly, the adjusted values are quantitatively in close agreement with the optical results. This suggests that in the studies only based on constant-displacement tests, the resistance against subcritical cracking for cement paste specimens was underestimated when the water content is high. This also implies that most of the earlier studies may have overevaluated the role of SCG in the relaxation if creep effect is not considered, at least at high relative humidity.
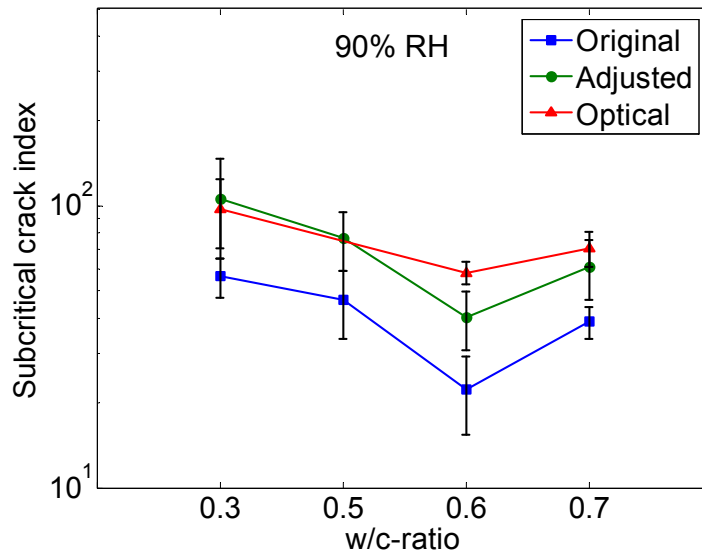
Figure 5.2. The diagram showing subcritical crack index (*n*) obtained from original DT tests (original), optical measurements (optical) and creep-induced relaxation separation (adjusted), for cement paste specimens as a function of w/c-ratio at 90% RH. The *vertical error bars* on each data point denotes the respective standard deviation.

5.5. Subcritical crack growth in cement pastes

5.5.1. General

For highly heterogeneous materials like cement pastes, the microstructural properties (e.g. porosity, density and etc.) along the crack path can differ for the same type of specimens, leading to the difference of the *K-v* curves. This difference was also observed in previous studies in various other materials (e.g. Wiederhorn, 1982; Atkinson, 1984; Beaudoin, 1985; Nadeau et al., 1974) and the dependence of *K-v* diagrams on relative humidity or w/c-ratio was not clearly identified due to large scattering of the experimental data. Because the heterogeneity can lead to crack-tortuosity, crack-branching and crack-bridging (Diamond and Bentur, 1985; Van Mier, 1991; Van Mier, 1997; Bisschop and Van Mier, 2002b), the crack path could deviate from the centerline even with the presence of guiding groove. The deviation then leads to stress concentration during the cracking and consequently difference between actual and expected results. The scattering of *K-v* curves in previous studies could therefore be due to the lack of optical access to the crack propagation and inclusion of erroneous measurements. In my study, such erroneous measurements were excluded under optical scrutiny (i.e. ensuring that the direction of the crack propagation is along the centerline).

For cement pastes, the fracture toughness, which is directly related to strength, is affected by factors such as density, moisture content and age etc. (Mindess and Young, 1981). Accordingly, the strength increases with the density of the cement paste, which in turn is primarily determined by the w/c-ratio. The relative range (X-axis) of each curve in the *K-v* diagram is therefore expected to be dependent on the fracture toughness (i.e. as

the upper limit) of the material under the selected environmental conditions (e.g. relative humidity, temperature).

However, as shown in Chapter 5.4, if the relaxation process in each DT test is not only due to subcritical crack growth, but also partly due to creep-induced relaxation in the DT specimens. Therefore, the interpretation of the traditional *K-v* results for cement paste in terms of subcritical crack needs to be done with much care. This is also an important added value of this study.

5.5.2. Low water content

At low water content (e.g. 10% RH), the subcritical crack growth in hardened cement paste is found to decelerate rapidly to an arrest and might be reactivated at later time. This is expected for cement paste with a heterogeneous microstructure because of crack arrest by discontinuities in the microstructure, such as unhydrated cement grains or portlandite crystals. The susceptibility to subcritical cracking is expected to vary from location to location with strong discontinuities. This can also explain the scattering of the *K-v* curves within the same test series results observed in Figure 4.4 and Figure 4.5. Because crack tip detection in ESEM is accurate within several micrometers, the force relaxation recorded without measurable crack propagation must be due to creep effect.

The ratio v_{opt}/v_r decreases over time, indicating that the relative contribution of creep in the DT-tests increased with time. Also compared to calcite for which the ratio v_{opt}/v_r is clearly close to unity as expected for non-creeping material, the cementitious materials exhibits significant creep-induced effects together with subcritical cracking. However,

the onset of the recorded cracking was occasional and the growth was not continuous at micro scales, indicating the strong influence of the material heterogeneity on the subcritical crack arrest. Such occasional subcritical cracking at later time was likely to have been assisted by thermal fluctuations at the crack-tip bonds in local heterogeneities, to overcome various energy barriers for bond rupture.

5.5.3. High water content

Unlike at dry conditions, continuous subcritical crack growth at high relative humidity occurred in cement paste specimens, and apparently decreased in an exponential way. This was suggested by previous SCG studies in other materials (e.g. Pletka et al, 1979; Atkinson, 1984).

The cement paste specimens showed decreasing ratio of v_{opt} to v_r, with the increase of time. This difference indicates that the calculated velocities are overestimated. During the initial period, subcritical cracking contributes to most of the measured relaxation, while during the later period creep contributes most. Due to their heterogeneous nature, cement pastes are expected to show a relatively high local variation of resistance against subcritical cracking and of subcritical crack arrest (see Chapter 4.2.2). The creep-induced relaxation, though decreasing with time as well, always exists in hardened cement pastes when under stress. Moreover, the crack tip is continuously propagating to new locations, and each occurrence of a new location functions as a starting point of creep-induced relaxation at that location, approximately. And due to the special geometry of the specimen, the creep-induced relaxation is expected to come mostly from the materials around the crack tip. Therefore, at each new location the creep-induced relaxation is at its

128

respective maximum until the crack tip moves to the next position. And its proportion in the total force-relaxation is expected to increase with time, as compared with subcritical cracking. The effect of w/c-ratio on the evolution of velocity-ratio has not been found to be pronounced.

5.5.4. Effect of w/c-ratio on subcritical crack growth

For cement pastes, the fracture toughness, which is directly related to strength, is affected by factors such as density, moisture content and age etc. (Mindess and Young, 1981). Accordingly, the strength increases with the density of the cement paste, which in turn is primarily determined by the w/c-ratio. The relative position (X-axis) of each curve in the K-v diagram is therefore expected to be dependent on the fracture toughness (i.e. as the upper limit) of the material under the selected environmental conditions (e.g. relative humidity, temperature). This is shown by plotting K_I/K_{Ic} vs. v in Figure 5.3, according to Figure 4.4 and Figure 4.5. The K_I/K_{Ic} range of each curve appears to be higher for specimens with higher w/c ratio, with exception of w/c-0.7 specimens (possibly due to local material heterogeneity). This is consistent with the fact that the susceptibility to cracking (both subcritical and mechanical) increases with w/c-ratio in cement paste. At high water content (i.e. 90% RH), this trend is less pronounced than at low water content (i.e. 10% RH). The effect of creep does not influence the relative position of the K-v diagrams (i.e. it mainly leads to an overestimation of measured v-values) and can therefore be considered as insignificant. Nevertheless, the inaccuracy induced by the scatter of K-v curves (i.e. the maximum variation of K_I is about ±20% with respect to the average K_I for each test series) can also influence this trend. Therefore the effect of w/c-

ratio on subcritical crack growth could also be not as significant as shown in Figure 5.3. The interpretation of the raw diagrams should then be done with caution.
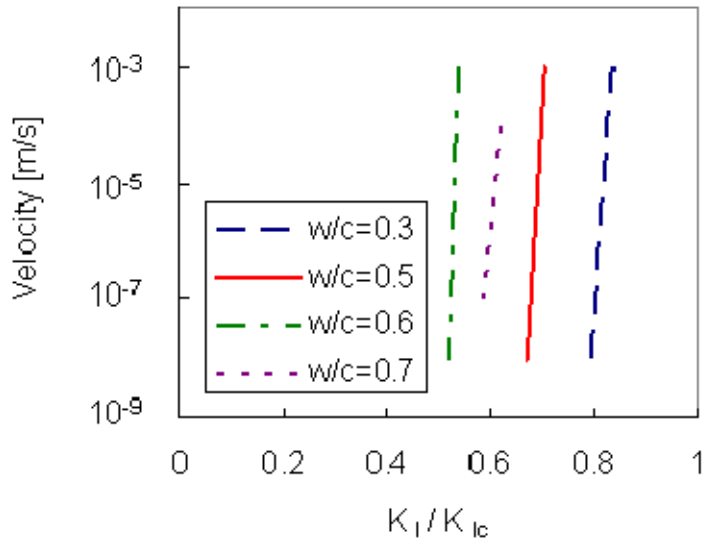
(a) at 10% RH
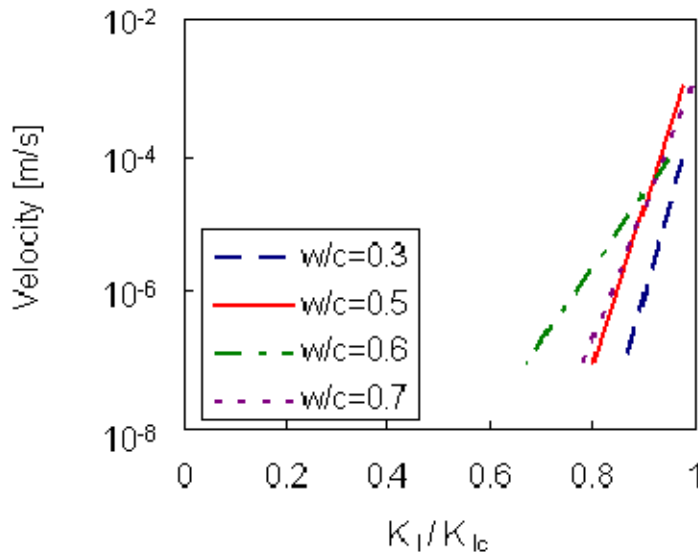
(b) at 90% RH

Figure 5.3. Normalized traditional *K-v* diagrams at (a) 10% RH and (b) 90% RH. The stress intensity factors (K_I) are normalized by respective critical stress intensity factor (K_{Ic}) values. The curves are based on Figure 4.4 and Figure 4.5, using the averaged K_I and *n*-values. Velocities are apparent values.

Furthermore, a typical *K-v* diagram can be divided into three regions (see Chapter 2.4.1). When the crack velocity is relatively low, then stress-corrosion process becomes rate-determining (region I cracking). When the crack growth is fast, then the transport of water molecules to the crack tip becomes rate-determining. This transport rate does not change much during the cracking and thus causes a plateau in the *K-v* diagram, i.e., region II cracking (see also Chapter 2.4.1). The *K-v* diagrams for the cement pastes in his study show the absence of the plateau (region II). Hydrated cement paste contains water molecules as intrinsic components. Part of this water is bound in the layered structures of C-S-H and the amount of it depends on the environmental moisture content (Mindess et al., 1974). In this study, the specimens were pre-equilibrated at a low or a high relative humidity. Thus, at specific RH (e.g. 90% RH), subcritical cracking may be induced by moisture that is already present in the capillary or gel pores of cement paste. Water diffusion from the environment to the crack tip is therefore not expected to be rate-limiting as in glass or other non-hydrated materials. The disappearance of the region II in *K-v* diagrams is therefore an expected outcome. This absence has also been observed in previous studies on SCG in cementitious materials (e.g. Beaudoin, 1985a; Beaudoin, 1985b; Mindess et al., 1974).

5.6. Lifetime analysis

5.6.1. Introduction

For most brittle or quasi-brittle materials, SCG takes place under some static load, before the materials' fracture toughness requirements are satisfied. The subcritical crack growth, in which the K_I values at crack tips are well below the K_{Ic}, is largely within the

linear range of materials' fracture behavior (Hu et al., 1988). This applies even for quasi-brittle materials that exhibit nonlinearity, since significant nonlinearity only occurs under relatively high loads (when K_I at specific tip nears K_{Ic}). At relatively high loading rates, nonlinear behaviors are also less significant than at low rates (see Chapter 2.3.3), quasi-brittle materials can therefore be considered as behaving linear elastically. At ambient temperatures, some of materials' fracture behaviors exhibiting negligible nonlinearity can therefore be approximated by linear elastic fracture mechanics (LEFM) (Beer et al., 1986). In this thesis work, the cement paste specimens were found to behave non-linear elastically (i.e. creeping). However, after empirical creep subtraction (see Chapter 5.4.2), the specimens were assumed to be linear elastic (i.e. undergoing SCG but without creeping). This approximation then renders the possibility of making time-to-failure predictions on cement paste specimens undergoing SCG, based on LEFM.

5.6.2. Models

The total time of fracture process (t_f) is composed of two key parts: time for crack initiation (t_i) and time from initiation to failure through propagation (t_p), thus

$$t_f = t_i + t_p \tag{5.2}$$

, if the specimen is notched or has a pre-existing crack, then the initiation time t_i will be negligible thus the total time-to-failure t_f is approximately the same as the time spent on propagation t_p (Young and Beaumont, 1976). However such estimation is then, to some extent, conservative. The K_I and v can be extracted from typical K-v diagrams through experiments under static load. The determination of the time-to-failure is obtained by

132

incorporating Equation 2.2 into Equation 2.9 and then integrating between limits of K_{Ii}

and K_{Ic} to arrive at an easy-to-calculate expression as (Evans, 1972):

$$t_f = \frac{2}{\sigma_a^2 Y^2} \int_{K_{Ii}}^{K_{Ic}} \frac{K_I}{v} dK_I \tag{5.3}$$

$$= \frac{2(K_{Ii}^{2-n} - K_{Ic}^{2-n})}{(n-2)A_0 Y^2 \sigma_a^2}. \tag{5.4}$$

where t_f is the time-to-failure, K_{Ii} is the initial stress intensity factor, K_{Ic} is the critical

stress intensity factor, n is the subcritical crack index, σ_a is the applied stress at the crack

tip, Y is a geometric constant and A_0 is from the constant part in Equation 2.9. Equation

5.3 can be applied for region I and II, while Equation 5.4 is obtained for region I, and is a

function of the applied stress. If n is large (e.g. $50 > n > 9$ for ceramics) and $K_{Ii} \ll K_{Ic}$

(only if $K_{Ii} < 90\% K_{Ic}$), then Equation 5.4 can be further approximated as (Beaumont and

Young, 1975)

$$t_f \cong \frac{2K_{Ii}^{2-n}}{(n-2)A_0 Y^2 \sigma_a^2} \tag{5.5}$$

For SCG showing a complete three-region K-v behavior, in each region the

mathematical relation between K and v (as a function of K) is different from each other,

thus the time for each region needs to be calculated separately. However, since in practice

the time spent in region I accounts for most of the time-to-failure, region II and especially

region III are normally not taken into account (Watchman, 1974).

By incorporating statistical fracture theory, a statistical time-dependent crack growth

model is derived as (Munz and Fett, 1999)

$$ln\,ln\frac{1}{1-Pr} = \frac{m_w}{n-2}ln\,t_f + \frac{m_w}{n-2}(\frac{1}{2}A_0 Y^2 K_{Ic}^{n-2}\sigma^n(n-2)) - m_w\,ln\,\sigma_c \tag{5.6}$$

133

where Pr is the probability of fracture, m_w is the Weibull modulus, σ is the applied stress and $σ_c$ is the characteristic strength of the material. With these parameters, the plot of fracture probability at given applied stress can be obtained. However, there exists inaccuracy in the extraction of constants (i.e. n, A_0), leading to the fluctuation of the values for lifetime predictions in studies of some specimens, e.g. rocks (Atkinson, 1984).

5.6.3. Failure probability for cement paste

It has been found that the resistance to subcritical cracking for HCP increases at lower relative humidity and that no conclusive influence of w/c-ratio (or porosity as well) can be identified (see Chapter 4.2). Optical measurement of the crack velocities can provide a way to justify the K-v diagrams for true subcritical cracking. The slope can be further used in lifetime analysis for making failure predictions for cementitious materials (Nadeau et al., 1974; Evans and Wiederhorn, 1984).

Failure probability studies were performed for cement paste at 90% RH, based on Equation 5.6. The values of K_{Ic}, n and A are obtained from the DT test results. The value of Y was chosen to be $\sqrt{\pi}$, assuming that a shallow crack in rectangular plate with large aspect ratio subjected to uniform tensile stress (Nara et al., 2010). The Weibull modulus m_w is taken equal to 10 for cement paste, according to previous studies (Hu et al., 1985). The normalizing constant σ* is calculated from 50% failure probability modulus of rupture (12.7 MPa) to be 13.17 MPa for cement paste (Hu et al., 1988).

For specimens at 10% RH, the failure probability studies were not applicable, due to the lack of SCG and high n-values (higher than 150). This leads to extremely large

lifetimes (e.g. 10 to the power of hundreds of years), which shows that SCG is unimportant under these conditions.
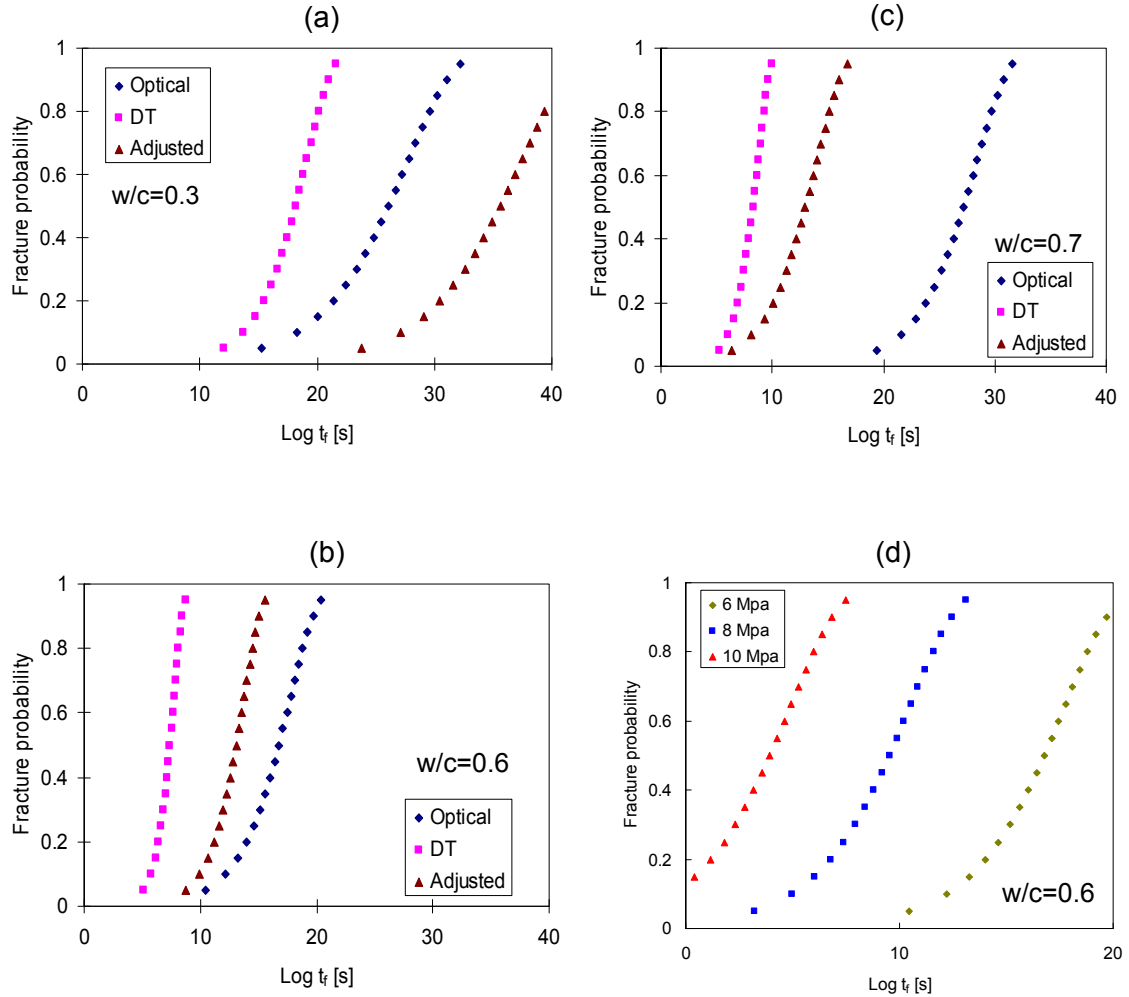
Figure 5.4. Diagrams showing the failure probability as a function of time-failure (t_f, in logarithmic scale with the unit of sec.) for specimens at 90% RH, based on measurements of original DT tests (original), optical measurements (optical) and creep-induced relaxation separation (adjusted). (a), (b) and (c) are for cement paste specimens (w/c-ratio of 0.3, 0.6 and 0.7) under applied stress of 6 MPa. (d) is under applied stress of 6, 8 and 10 MPa for cement pastes (w/c-ratio of 0.6).

The fracture probabilities for tests at 90% RH are presented as a function of time-to-failure (t_f) in Figure 5.4. At the applied stress of 6 MPa, the failure probabilities based on

the original DT measurements are at least 4 times higher than those of optical measurements and adjusted DT measurements (Figure 5.4a, b and c), which is consistent with the trend shown in Figure 5.2. The real effect of subcritical crack is less than expected from DT tests. In Figure 5.4d, an example, for cement paste (w/c-ratio of 0.6) specimens, shows that given the same failure probability the t_f is decreasing with the increasing applied stress. This is expected because the rate of the environment-assisted deterioration at the crack tip increases with higher applied stress. And this increase in turn facilitates the subcritical cracking at the crack tip and leads to lower resistance against failure, therefore resulting in lower lifetime until failure.

5.7. Healing effect of subcritical cracks in cement paste

5.7.1. General

It has been shown that cracks can grow subcritically in cement paste in humid environment (see Chapter 4.2.5), therefore able to deteriorate the long-term durability of cement-based structures. However, possible healing of the slowly-propagating cracks can also happen over long durations. Even after a long period of time, there are still unreacted cement particles in cementitious materials. When cracks occur, water from outside or other internal pores may gain access to these particles and restart hydration reactions locally. The cracks can then be partially or entirely filled by the hydration products. Therefore, cracks inside cementitious materials can, to a certain degree, heal automatically in certain environmental conditions such as underwater, wet-dry or freeze-thaw cycles as exist in nature (Edvardsen, 1999, Jacobsen and Sellevold, 1996). Different from sealing of cracks which shares similar crack-closing patterns, self-healing can lead

136

to various degrees of strength recovery, depending on specific situations (Hearn, 1998). However, this mechanism tends to be more effective for early-age materials or low water/cement-ratio materials, where there is still a significant portion of cement unreacted as well as along crack paths.

In this study, the self-healing effect was found to be present in the subcritical cracks in the cementitious matrix, assisted by environmental precipitates or the unhydrated cement particles. The healing may even be a parallel process alongside of the subcritical cracking, especially for situations of early age materials, slow crack growth or crack arrest, and lead to recovery of the material's resistance against SCG as well as strength. The long-term fracture behavior of a cementitious material should therefore take into account the self-healing as a counter effect.

5.7.2. High w/c-ratio

At high w/c-ratio of 0.7, it has been found that the subcritically-formed cracks were partly healed by the precipitates from the surrounding environment (i.e. $Ca(OH)_2$), after 1 month' wet-and-dry cycling and 5 months' submersion in limewater (enhanced experimental conditions to show the maximum achievable upper bound effect). The calcium ions in the pore solutions in cementitious materials can also react with carbonate ions to form calcite ($CaCO_3$). Precipitation of calcite on the crack surfaces can lead to closing of cracks, thus result in crack healing as well. DT tests on the specimens showed slightly weaker resistance of the sealed cracks against SCG than the cementitious matrix (see Figure 4.24). Healing from the unhydrated cement particles cannot be evidently observed, due to the high degree of hydration leading to insufficient amount of these

reactive particles along the crack path. It has been stated that the precipitate-rate depends on crack width and pressure of water (Edvardsen, 1999), and in this study it is mainly determined by crack width. In such a way, the precipitations can block the crack path and possibly recover some of the lost stiffness and strength. This mechanism is believed to be the one responsible for self-healing of mature cementitious materials (Yang et al, 2005). However, the relaxation measurement also could be due to the cracking of the lower part of each specimen (i.e. uncracked part below the surface crack), therefore the mechanical recovery effect might not result from the environmental precipitates.

At the sites where crack opening width is relatively large (e.g. larger than 50 μm), the subcritical crack showed a lower degree of healing (or sealing) and the crack surfaces remained visibly separated from each other. Therefore for crack (or part of the crack) with large opening, healing from the environmental precipitates was not sufficient to heal it completely and consequently not able to recover the full strength of it. At the places where crack opening width is relatively small (e.g. smaller than 50 μm), the subcritical crack showed higher degree of healing (or sealing) with the crack sealed by environmental precipitates. New subcritical cracks form and propagate in between the precipitates, indicating their weaker nature in terms of resisting SCG. This is consistent with the more porous structure (therefore more susceptible to cracking) of the precipitates, as compared with the cementitious matrix.

Compared with the cracks in most concrete materials where the self-healing requirement of narrow crack width (e.g. below 50 μm) is difficult to meet (Li and Yang, 2007), most part of the subcritically formed cracks are narrow and therefore suitable to be self-healed by environmental chemicals (e.g. $Ca(OH)_2$ and $CaCO_3$).

138

5.7.3. Low w/c-ratio

At low w/c-ratio of 0.3, it has been found that the subcritically-formed cracks can be healed by reaction products from unhydrated grains. Environmental precipitates are also expected to form during the healing (e.g. the brighter part of the healing materials in Figure 4.23). The formation of the new subcritical crack (e.g. Figure 4.22b and Figure 4.23b) indicates that the healing of the previously-formed crack is complete (both optically and mechanically). This is not surprising for a self-healed crack to exhibit full recovery of SCG resistance or even higher. Because the direct contact with sufficient water enabled the unhydrated cement particles that existed at the crack surfaces to react fully and form hydration products. This can lead to high degree of hydration, the new hydration products were then expected to possess higher strength (or higher fracture toughness) than other part of the matrix materials in the bulk. This is also consistent with previous studies on concrete materials that showed higher strength for the self-healing hydration products in early-age cracks (Hearn, 1998).

The healed crack does not show weaker resistance against SCG than the cementitious matrix (see Figure 4.24). This higher degree of healing (compared to that of w/c-0.7 specimens) was expected, because the contribution can come from both hydration and environmental precipitates. Indeed, the w/c-0.3 specimens were still in early age (1 month) when cracked and therefore contained certain amount of unhydrated cement. The unhydrated particles were able to react with the surrounding water, forming hydration products or $CaCO_3$ at the crack surfaces with access to water. The combining effects of

hydration and environmental precipitates tended to seal the cracks more effectively than when with only environmental precipitates.

Furthermore, cement pastes with higher w/c-ratio show higher degree of viscoelastic deformation (e.g. creep) during cracking (see Chapter 2.3.5). Indeed, this implies that the irreversible part of the deformation is then higher, which leads to larger opening of the crack upon unloading. The upper-limit criterion of the crack opening width (Li and Yang, 2007) is therefore more difficult to meet. Apart from this, healing due to environmental precipitates is also expected to be more pronounced when w/c-ratio is lower, if the crack opening is tighter. Conversely, the healing effect in w/c-0.3 specimens is stronger than in w/c-0.7 specimens, where only precipitates from environment participated in the recovery of the crack.

5.8. Implications on expected size-effect

Size differences often exist between specimens tested in laboratory and those applied in practice, especially for concrete materials. It is well known that the fracture of concrete structures is size-dependent (Bažant, 1984; Mindess, 1984; Nallathambi et al., 1985; Nallathambi et al., 1984). For example, the fracture toughness increases for larger concrete specimens. This can be explained as following: in a larger structure, a larger process zone (distributed with microcracks and defects) exists and absorbs a higher amount of energy that is needed for crack extension. Also the energy required for unit-crack extension is generally size-independent. The total energy needed for fracture is consequently higher, leading to higher fracture toughness. Similarly, the subcritical crack growth is also sustained by the supply of external energies, which come from the applied

140

stresses and environment-assisted chemical processes at the crack tip. In larger concrete specimens, the larger process zone needs to absorb a larger part of the energy needed for SCG. This effect can then cause the measured K-v diagrams to shift to regions with higher K_I values, meaning that the SCG would occur at higher K_I for larger specimens.

The fracture properties of cementitious materials are also known to be dependent on the ratio of specimen size to the maximum inclusion (grains, sands or aggregates) size (Duan et al., 2002). This dependence becomes insignificant if the former is much larger than the latter (Mindess and Nadeau, 1976), as the material becomes macroscopically more homogeneous. Therefore, it can be expected that, during subcritical cracking, the crack-arrest due to the heterogeneities in the cementitious matrix will be less pronounced for larger concrete specimens of the same type or same-size specimens using smaller aggregates. This would also mean that the susceptibility to SCG increases, corresponding to lower n-values. Accordingly, the lifetime of the material at a given stress will decrease.

CHAPTER 6 Conclusions

The main goal of this thesis work was to gain new fundamental knowledge about subcritical crack growth and improve our understanding of the subsequent static fatigue in concrete materials. To reach this goal, a series of questions need to be answered and the prime ones focused in this study are: what is the effect of stress (at crack tip) on the subcritical cracking in hardened cement paste (HCP)? What are the major factors that influence the subcritical cracking in HCP? And what is the importance of other time-dependent effects (e.g. creep, self-healing) in the slow crack growth processes in cementitious materials. Knowing these, the performance lifetime of concrete can be better predicted for evaluating the durability of concrete structures. To deal with these questions, double-torsion (DT) tests were carried out on HCP specimens, facilitated by ESEM or optical microscopes.

For the experiments, a micro-testing device was designed and constructed to perform DT tests inside ESEM or under optical microscopes. This testing device was supplemented with novel measuring device for monitoring the force and displacement at the loading point, and cooling stage for controlling the specimen temperature. The whole test set-up enables direct optical access for measuring the subcritical cracking velocities in DT specimens under various conditions (e.g. stress intensity factor, relative humidity) over time. By performing DT tests on single-crystal calcite using the test set-up, optically measured subcritical crack velocities was consistent with the calculated values for a non-creeping material. It was then used for studying the real subcritical cracking processes that have not been achieved for cementitious materials. The experimental parameters obtained were used as input in the fracture probability analysis for cement paste. The test

142

set-up was also employed in studying the creep-induced effect and self-healing in HCP specimens with the same geometries as the DT specimens.

6.1. Subcritical crack growth

An optical method is developed to measure the subcritical crack velocities in HCP DT specimens. In this method, the crack velocities obtained from optical measurements are used to correct the velocities calculated from force-relaxation curves during constant-displacement tests, by taking into account the creep-induced relaxation that is included in the subcritical cracking process.

Subcritical crack growth in cement paste is mainly dependent on the amount of water in the surrounding environment, w/c-ratio (or density) of the material and the applied stress intensity factor (as the driving force). At dry condition (10% RH), subcritical cracks decelerate rapidly and move in a step-wise manner in cement paste. Slowly propagating cracks are easily arrested in the DT-test by discontinuities in the microstructure. After being arrested, subcritical cracks still can grow occasionally, in a discrete manner. At wet condition (90% RH), subcritical crack is growing continuously in cement paste. At lower relative humidity, the susceptibility of the cement paste to subcritical cracking appears to be lower and the lifetime prediction tends to be substantially higher, under sustained load. The w/c-ratio does not have significant influence over the relative susceptibility (subcritical crack index) of different cement pastes to subcritical cracking. When the w/c-ratio is the higher, the subcritical cracking

can take place at lower stress intensity factors at the crack tip, with the fracture toughness of the cement paste being lower.

With these findings from this study, some practical implications can be obtained. In order to reduce the impact of subcritical cracking for load-bearing concrete structures, the following suggestions could be adopted: (a) Reduce the w/c-ratio of the cementitious matrix; (b) Use aggregates with large dispersion of particle sizes; (c) Minimize the contact with aqueous environments; (d) Sustain load at a level as low as possible, ideally lower than that of the threshold stress intensity factor.

6.2. Creep-induced effects in subcritical crack growth

Significant creep-induced deformation is present in HCP specimens during subcritical cracking. Subcritical crack velocities calculated from the force-relaxation curves are therefore overestimated. And this produces underestimated subcritical crack indices (n-value) and leads to less accurate lifetime predictions for cement paste under sustained load. The creep-induced relaxation in the cement paste is more pronounced at higher relative humidity and, for a short period, the relative degree of relaxation is not significantly dependent on the w/c-ratio. At dry condition (10% RH), the creep-induced relaxation is more pronounced than subcritical cracking, due to the easy crack-arrest. At wet condition (90% RH), the proportional contribution of creep to the total relaxation is increasing over time, compared to that of the subcritical cracking. As a time-dependent phenomenon, creep can lead to unloading effect in the materials around the crack tip and consequently retarding the subcritical cracking over time.

144

6.3. Self-healing

In HCP specimens that are submerged in lime water, self-healing was observed in subcritical cracks with narrow crack opening width. The healing agents can originate from either the ions (e.g. $Ca(OH)_2$ or $CaCO_3$ precipitates) in the aqueous environment or the unhydrated particles in the cement paste. The healing effect is dependent on the crack opening width and the degree of hydration (i.e. the amount of unhydrated particles that are exposed to water along the crack path) of the cement paste. The self-healing is more pronounced when the crack opening width is smaller or the degree of hydration is lower. For cement paste with low degree of hydration, full closing of the subcritical cracks can be reached and the resistance against subcritical cracking can also be restored. Self-healing, as another time-dependent phenomenon, is expected to counteract the subcritical cracking over long period of time.

6.4. Future perspectives

It has been shown that the time-dependent phenomena such as subcritical crack growth and creep in cementitious materials can coexist and proceed simultaneously over long period of time. While, self-healing can potentially also play an important role during SCG. Several aspects of these phenomena can be further investigated:

- Understanding of the various physical aspects involved in the SCG process in concrete is not yet available. The reason is that there is incomplete and inaccurate knowledge of the SCG behavior in concrete. Further efforts should be made to deepen the understanding through experimental studies on different factors. This possibly includes the influence of particle/aggregate sizes and

145

types, the water-to-binder ratio and the specimen preparation (e.g. curing time, with/without shrinkage cracks).

- The results of my studies on SCG in cement paste can be further used for modeling purposes. The experimental data can function as a basis for developing or tuning SCG models to work better for cementitious materials, especially for concrete. The durability of concrete structures will then be easier to evaluate in long-term services.

- The size effect on the SCG behavior in cementitious materials is not known. This is due to the limited experimental tools (e.g. optical access to the crack tip) available for accurately studying the SCG in cementitious materials of various sizes (especially of larger sizes). Also previous studies based on indirect measurement of crack velocities have not considered the erroneous influence of creep, therefore cannot be used for studying size effects. Investigations on large specimens can possibly be conducted with the help of digital image correlation method and specially-assembled testing devices, under different conditions. Furthermore, if the SCG in concrete (through DT test) can be modeled accurately, then simple change of dimensions in the modeling studies can make size-effect predictions easier to implement.

- In this study, SCG in cement paste is found to be associated with creep. It is also interesting if the influence of creep can be minimized (or ideally excluded) during SCG, so that the two effects can be elucidated separately and accurately. For example, whether the increase of the specimen thickness can reduce the creep-induced relaxation in DT specimens or not.

- In order to understand the dynamic effect of self-healing on SCG in cementitious materials, specimens with ongoing SCG under various conditions can be studied over a long period of time. These conditions possibly include aqueous environments with different chemicals dissolved inside or wet-and-dry cycling of the specimens. Constant displacement or constant load tests can be employed to maintain SCG in specimens under these conditions during long term.

REFERENCES

Alexander MG, Davis DE (1989), Properties of aggregates in concrete, Hippo Quarries Technical Publication, South Africa.

Alizadeh R., Beaudoin JJ., Raki L. (2010) Viscoelastic nature of calcium silicate hydrate, Cement and Concrete Composites, 32 [5], pp. 369-375.

Alizadeh R, Beaudoin JJ, Raki L (2011), Mechanical properties of calcium silicate hydrates, Materials and Structures, 44, pp. 13–28.

Anderson OL, Grew PC (1977), Stress corrosion theory of crack propagation with applications to geophysics, Rev. Geophys., 15(1), pp.77–104.

Arsenault RJ (1964), Arsenault Low-temperature creep of alpha iron, Acta Met., 12, pp. 547.

Ashby MF, Gandhi C, Taplin DMR (1979), Fracture-mechanism maps and their construction for F.C.C. metals and alloys, Acta Metall., 27, pp. 699–729.

Atkinson BK (1982), Subcritical crack propagation in rocks: theory, experimental results and application, Journal of Structural Geology, 4, pp. 41 -56.

Atkinson BK (1984), Sub-critical crack growth in geological materials, J. geophys. Res. 89, pp. 4077–4114.

Baalbaki W, Benmokrane B, Challal O, Aitcin PC (1991), Influence of coarse aggregate on elastic properties of high performance concrete, ACI Mater J, 88 (5), pp. 499–503.

Barrick JE II, Krokosky EM (1976), Effects of Temperature and Relative Humidity on Static Strength of Hydrated Portland Cement, J. Test Eval. 4, No. 1, pp. 61-73.

Bažant ZP (1972), Thermodynamics of hindered adsorption and its implications for hardened cement paste and concrete, Cem. and Conc. Research, 2 (1), pp. 1-16.

Bažant ZP (1984), Size effect in blunt fracture: concrete, rock, metal. J. Engng Mech. (ASCE) 110, pp. 518-535.

Bažant ZP, Asghari AA, Schmidt J (1976), Experimental study of creep of hardened Portland cement paste at variable water content, Mater. Struct., 9, pp. 279-290.

Bažant ZP, Chern JC (1985), Concrete creep at variable humidity: constitutive law and mechanisms, Mater. Struct., 18 (103), pp. 1-20.

Bažant ZP (1993), Current status and advances in the theory of creep and the interaction with fracture. Proc. 5 Int. RILEM Symp. on Creep and Shrinkage of Concrete, Barcelona, Spain, pp. 291-307.

Bažant ZP, Bai SP and Gettu R (1993), Fracture of rock: effect of loading rate, Eng Fract Mech, 45, pp. 393-398.

Bažant ZP, Gettu R (1992), Rate effects of and load relaxation in static fracture of concrete. ACI Mat. J. 89, pp. 456-468

Bažant ZP, Prat PC (1988), Effect of temperature and humidity on fracture energy of concrete. ACl Materials Journal, 87(4), pp. 262-271.

Bažant ZP, Schell WF (1993) Fatigue fracture of high strength concrete and size effect. ACI materials J. 90(5), pp. 472–478.

Bažant ZP (1998), Material models for structural creep analysis, Chaper 2 Edited in Mathematical modeling of creep and shrinkage of concrete. Edited by Z.P. Bazant. Wiley & Sons, New York.

Bažant ZP, Prat PC (1999), Effect of temperature and humidity on fracture energy of concrete, ACI Mat. J., 85, pp. 262-271.

Beaudoin JJ (1985a), Effect of humidity on subcritical crack growth in cement paste, Cement and Concrete Research 15, pp. 871-878.

Beaudoin JJ. (1985b), Effect of water and other dielectrics on subcritical crack growth in Portland cement paste. Cement and Concrete Research 15, pp. 988-994.

Beaumont PWR, Young RJ (1975), Failure of brittle polymers by slow crack growth (part 1). Journal of Materials Science, 10, pp. 1334-1342.

Beer HR, Kaiser T, Moloney AC, Kauschm HH (1986), Static Fatigue and Time to Failure Predictions of Particulate Filled, Epoxide Resin Composites, J. Material Sci., 21, pp. 3661-3667.

Bentur A, Berger RL, Lawrence FV, Milestone NB, Mindess S, Young JF (1979), Creep and Drying Shrinkage of Calcium Silicate Pastes III. A Hypothesis of Irreversible Strains, Cem. Concr. Res., 9, pp. 83–96.

Bentz DP, Garboczi EJ (1992), Modelling the Leaching of Calcium Hydroxide from Cement Paste: Effects on Pore Space Percolation and Diffusivity, Mater. Struct, 25, pp. 523-533.

Bieniawski ZT (1967), Mechanism of brittle fracture of rock, Part I—Theory of the fracture process, Int. J. Rock Mech. Min. Sci. 4, pp. 395–406.

Bisschop J (2002), Drying Shrinkage Microcracking in Cement-Based Materials, Ph.D. Thesis, Delft University Press, Netherlands.

Bisschop J., Van Mie JGM. (2002b), Effect of aggregates on drying shrinkage microcracking in cement-based materials, Materials and Structures, 35, pp. 453-461.

Blum W, Eisenlohr P, and Breutinger F (2002), Understanding Creep—a Review, Metall. Mater. Trans. A, vol. 33A, pp. 291–303.

Brian R. Lawn (2001), Fracture Growth (subcritical) in brittle materials, Encyclopedia of Materials: Science and Technology, pp. 3286-3290.

Broberg KB (1989), The near-tip field at high crack velocities, Int. J. Fract., 39, pp. 1–13.

Brown JH, Pomeroy CD (1973), Fracture toughness of cement paste and mortar, Cem. Concr. Res., 3, pp. 475–480.

Buck AL (1996), Buck Research Manual.

Card JC, Cannon RM, Saiz E, Tomsia AP, Ritchie RO (2007), On the Physics of Moisture-Induced Cracking in Metal-Glass (Copper-Silica) Interfaces, Journal of Applied Physics 102 (5), 053516 .

Charles RJ (1958), Static fatigue of glass, J. Appl. Phys. 29 11, pp. 1549–1560.

Cho T (2007), Prediction of cyclic freeze-thaw damage in concrete structures based on response surface method. Constr. Build. Mater, 21(12), pp. 2031–2040.

Ciccotti M, Gonzato G, Mulargia F (2000), The double torsion loading configuration for fracture propagation: an improved methodology for the load-relaxation at constant displacement. Int. J. Rock Mech. Min. Sci., 37, pp.1103-1113.

Cordon WA, Gillespie HA (1963), Variables in concrete aggregates and Portland cement paste which influence the strength of concrete, ACI J., 60(51), pp.1029–1051.

Day RL (1981), Reactions Between Methanol and Portland Cement Paste, Cem. Concr. Res., 11, pp. 341-349.

Diamond S (1996), Delayed ettringite formation — processes and problems. Cem. Concr. Compos. 18, pp. 205–215.

Diamond S, Bentur A. (1985), On the cracking in concrete and fiber-reinforced cements. In: Application of fracture mechanics to cementitious composites, S.P., Shah, ed. Martinus Nijhoff, The Netherlands, pp. 87-140.

Duan K, Hu XZ, Wittmann FH (2002), Explanation of Size Effect in Concrete Fracture Using Non-Uniform Energy Distribution, Mater. Struct., 35, pp. 326-331.

Dunning JD, Lewis WL, Dunn DE (1980), Chemo- mechanical weakening in the presence of surfactants. Journal of Geophysical Research, 85, pp. 5344-5354.

Dutton R (1974), The propagation of cracks by diffusion, Bradt RC, Hasselman DPH, Lange FF (Eds.), Fracture Mechanics of Ceramics (13th edn), Vol. 2Plenum Press, New York, pp. 647–657.

Edvardsen C (1999), Water Permeability and Autogenous Healing of Cracks in Concrete, ACI Mater. J., 96, pp. 448–454.

Evans AG (1972), A method for evaluating the time-dependent failure characteristics of brittle materials—and its application to polycrystalline alumina, J. Mater. Sci. 7, pp. 1137–1146.

Evans AG (1974), Slow crack growth in brittle materials under dynamic loading conditions, Int. J. Fract. 10, pp. 251–259.

Evans AG, Clifton JR, Anderson E (1976), The fracture mechanics of mortars, Cement and Concrete Research 6, pp.535-548.

Evans AG, Johnson H (1975), The Fracture Stress and Its Dependence on Slow Crack Growth, J Mater Sci 10, pp. 214–222.

Evans AG, Wiederhom SM (1974), Crack Propagation and Failure Prediction in Silicon Nitride at Elevated Temperatures, J. Mater. Sci., 9 [2], pp. 270-78.

150

Evans AG, Wiederhorn SM (1984), Proof testing of ceramic materials – an analytical basis for failure prediction, Int. J. Fract., 26, pp. 355-368.

Feldman RF (1972), Mechanism of creep of hydrated Portland cement paste, Cem. Concr. Res. 2, pp. 521-540.

Feldman RF, Sereda PJ (1968), A Model for Hydrated Portland Cement Paste as Deduced from sorption-length Change and Mechanical Properties, Materials and Structures , Vol. 1, No. 6, pp. 509-520.

Feng X., Garboczi, E.J, Bentz DP., Stutzman P.E, Mason T.O. (2004), Estimation of the Degree of Hydration of Blended Cement Pastes by a Scanning Electron Microscope Point-Counting Procedure, Cem. Concr. Res., V. 34, pp. 1787-1793.

Fett T, Rizzi G, Guin JP, López-Cepero JM, Wiederhorn SM (2009), A fracture mechanics analysis of the double cleavage drilled compression test specimen, Eng. Fract. Mech., vol. 76, pp. 921–934.

Freiman SW, Mulville DR, Mast PW (1973), Crack Propagation Studies in. Brittle Materials, J. Mater. Sci., 8, pp.1527-1533.

Freiman SW (1984), Effects of chemical environments on slow crack growth in glasses and ceramics, J Geophys Res 89, pp. 4072–4076.

Freiman SW, Wiederhorn SM, Mecholsky JJJ (2009), Environmentally Enhanced Fracture of Glass: A Historical Perspective. Journal of the American Ceramic Society, 92(7), pp. 1371-1382.

Freund LB (1979), The Mechanics of Dynamic Shear Crack Propagation, J. Geophys. Res., 84(B5), pp. 2199–2209.

Fuller ER (1979), An evaluation of double-torsion testing - Analysis, ASTM STP 678, pp. 3-18.

Gandhi C, Ashby MF (1979), Fracture mechanism maps for materials which cleave: F.C.C., B.C.C. and H.C.P. metals and ceramics, Acta Metall., 27, pp. 1565–1602.

Giaccio G, Rocco C, Violini D, Zappitelli J, Zerbino R (1992), HSC incorporating different coarse aggregates, ACI Mater J, 89 (3), pp. 242–246.

Gonzalez AC, Pantano CG (1990), A Compression-Loaded Double Cantilever Beam Specimen. Journal of the American Ceramic Society, 73: pp. 2534–2535.

Gopalaratnam VS, Shah SP (1985), Softening response of plain concrete in direct tension, 1985, J. Am. Concr. Inst., 82, pp. 310–323.

Griggs DT, Blacic JD (1965), Quartz: Anomalous weakness of synthetic crystals, Science, 147, pp. 292-295.

Gumbsch P, Gao H (1999), Dislocations Faster Than the Speed of Sound, Science, 283, (5404), pp. 965-968.

Gurney C, Mai VW (1972), Stability of cracking, Eng. Fracture Mech., 4, pp. 853-863.

Haecker CJ, Garboczi EJ, Bullard JW, Bohn RB, Sun Z, Shah SP, Voigt T (2005), Modeling the linear elastic properties of Portland cement paste, Cement and Concrete Research, Vol. 35(10), pp.1948-1960.

He MY, Turner MR, Evans AG (1995), Analysis of the Double Cleavage Drilled Compression Specimen for Interface Fracture Energy Measurements over a Range of Mode Mixities, Acta Metall. Mater., 43 [9], pp. 3453–3458.

Hearn N (1998), Self-Sealing, Autogenous Healing and Continued Hydration: What is the Difference, Materials and Structures, V. 31, No. 8, pp. 563-567.

Hillerborg A (1983), Theoretical analysis of the double torsion test. Cement and Concrete Research, Vol 13, pp. 69–80.

Hillig WB, Charles RJ (1965), Surfaces, stress-dependent surface reactions, and strength, High-Strength Materials, Wiley, New York, pp. 682–705.

Hillig WB (2006), The C-H delayed failure mechanism revisited. Int J Fract., 139, pp. 197–211.

Horii H, Shin H-C, Pallewatta T (1992) Mechanism of Fatigue Crack Growth in Concrete, Cement & Concrete Composites, Vol. 14, pp. 83-89.

Hsu TTC (1963), Mathematical analysis of shrinkage stresses in a model of hardened concrete, Journal of the American Concrete Institute, Proc., Vol. 60, No. 3, March, pp. 371–390.

Hu XZ, Cotterell B, Mai YW (1985), A statistical theory of fracture in a two-phase brittle material, Proc R Soc Lond, A401, pp. 251–265.

Hu XZ, Mai YW, Cotterell B (1988), A statistical theory of time-dependent fracture for brittle materials, Phil. Mag., 58, pp. 299–324.

Husak AD, Krokosky EM (1971), Static fatigue of hydrated cement concrete. J. Am. Concrete I. 68, pp. 263-271

Irwin GR (1958), Fracture. Encyclopedic of Physics, Springer, Berlin, Vol. 6, pp. 551.

Jacobsen S, Marchand J, Boisvert L (1996), Effect of cracking and healing on chloride TRANSPORT in OPC concrete, Cem. Concr. Res., 26 6, pp. 869–881.

Jacobsen S, Sellevold EJ (1996), Self healing of high strength concrete after deterioration by freeze/thaw, Cement and Concrete Research, Vol. 26, No. 1, pp. 55-62.

Janssen C (1974), Specimen for fracture mechanics studies on glass. In: Proceedings of the Xth international congress on glass. Kyoto, Japan, pp. 23.

Jenq YS, Shah SP (1985), Two parameter fracture model for concrete, J. Eng. Mech., 111, 1227-41.

Kaieda Y, Pae KD (1982), Fracture stress difference of notched polycarbonate between atmospheric pressure and a hydrostatic pressure, J. Mater Sci. 17, No. 2, pp. 369-376.

Kamen A, Denarié E, Brühwiler E (2009), "UHPFRC tensile creep at early age", Materials and Structures, Volume 42, Number 1, pp. 113-122.

Kaplan MF (1959), Flexural and compressive strength of concrete as affected by the properties of coarse aggregates, ACI J Proc, 55 (11), pp. 1193–1208.

Klug P, Wittmann FH (1974), Activation Energy and Activation, Volume of Creep of Hardened Cement Paste, Mat. Sci. Eng. 15, pp. 63-66.

Larrard F, Belloc A (1992), Are small aggregates really better for making high-strength concrete, Cem Concr Aggregates, 14 (1), pp. 62–66.

Lawn BR (1983), Physics of Fracture, J. Am. Ceram. Soc., 66 [2], pp. 83–91.

Lawn BR, Wilshaw TR (1975), Fracture of Brittle Solids, Cambridge University Press, London, pp. 204.

Lawn BR. (1993), Fracture of Brittle Solids, Cambridge Univ. Press, New York.

Li VC, Yang E (2007), Self healing in concrete materials, in: S. van der Zwaag (Ed.), Self Healing Material: An Alternative Approach to 20 Centuries of Materials Sciences, Springer, pp. 161–193.

Li Z, Kulkarni SM, Shah SP (1993), New test method for obtaining softening response of unnotched concrete specimen under uniaxial tension, Exp. Mech. 33, pp.181–188.

Lott JL, Kesler CE (1964), Crack propagation in plain concrete, 1964, University of Illinois, Urbana, T and AM Report No. 648.

Mai YW, Atkins AG (1980), Crack stability in fracture toughness testing, J. Strain Analysis, 15, pp. 63–74.

Mangat PS, Gurusamy K (1987), Permissible crack widths in steel fiber reinforced marine concrete, Materials and Structures 20 (9), pp. 338–347.

Marsh DM (1964), Plastic flow in glass. Proc. R. Soc. A279, pp. 420-435.

Martin RJ, Durham WB (1975), Mechanisms of crack growth in quartz. J. Geophys. Res. 80, pp. 4837-4844.

Matsumoto T, Li VC. (1999), Fatigue Life Analysis of Fiber Reinforced Concrete with a Fracture Mechanics Based Model, J. Cement and Concrete Composites Vol. 21, pp. 249-261.

Mecholsky JJ (1981), Intergranular Slow Crack Growth in MgF_2. Journal of the American Ceramic Society, 64: pp. 563–566.

Mehta PK, Monteiro (1993), Concrete Structure, Properties and Materials, Prentice-Hall Inc, New Jersey, 2nd Ed.

Michalske TA, Freiman SW (1983), A Molecular Mechanism for Stress Corrosion in Vitreous Silica, J. Am. Ceram. Soc. 66[4], pp. 284-288.

Mihashi H, Wittmann FH (1980), Stochastic Approach to Study the Influence of Rate of Loading on Strength of Concrete, Heron (The Netherlands) 25 (3), pp.5-54.

Mindess S (1984), The effect of specimen size on the fracture energy of concrete, Cem. Concr. Res. 14, pp. 431-436.

Mindess S (1985), Rate of loading effects on the fracture of cementitious materials. In: Application of fracture mechanics to cementitious composites, S.P., Shah, ed. Martinus Nijhoff, The Netherlands, pp. 617-638

Mindess S, Diamond S (1980), A preliminary SEM study of crack propagation in mortar. Cem. Concr. Res., 10, pp.509–519.

Mindess S, Diamond S (1982), A device for direct observation of cracking of cement paste or mortar under compressive loading within a scanning electron microscope. Cement and Concrete Research 12, pp.569-576.

Mindess S, Nadeau JS (1976), Effect of notch width on K_{IC} for mortar and concrete, Cem. Concr. Res. 6 (4), pp. 529-534.

Mindess S., Nadeau JS (1977), Effect of loading rate on the flexural strength of cement and mortar. Bull. Am. Cera. Soc. 56 (4), pp. 429-430.

Mindess S, Nadeau JS, Hay JM (1974), Effect of different curing conditions on slow crack growth in cement paste. Cement and Concrete Research 4, pp.953-965.

Mindess S, Young JF (1981), Concrete, Prentice-Hall, Inc. Englewood Cliffs, NJ.

Mullen WG and Dolch WL (1964), Creep of Portland cement paste, ASTM Proc. 64, pp. 1146-1171.

Munz D, Fett T (1999), Ceramics: Mechanical Properties, Failure Behaviour, Materials Selection, 1st ed. Berlin Heidelberg: Springer-Verlag, pp. 77–108.

Nadeau JS, Mindess S, Hay JM (1974), Slow crack growth in cement paste, J. Am. Ceram. Soc., 57, pp. 51-54.

Nallathambi P, Kafihaloo BL, Heaton BS (1984), Effect of specimen and crack sizes, water/cement ratio and coarse aggregate texture upon fracture toughness of concrete, Mag. Concr. Res. 36 (129), pp. 227-236.

Nallathambi P, Kafihaloo BL, Heaton BS (1985), Various size effects in fracture of concrete, Cem. Concr. Res. 15, pp. 117-126.

Nara Y, Kaneko K (2005), Study of subcritical crack growth in andesite using the Double Torsion test. Int. J. Rock Mech. Min. Sci.; 42: pp.521-530.

Nara Y, Takada M, Mori D, Owada H, Yoneda T, Kaneko K (2010), Subcritical crack growth and long-term strength in rock and cementitious material, Int. J. Fracture, 164, pp. 57–71.

Neville AM, Dilger WH, Brooks JJ (1983), Creep of plain and structural concrete. Construction Press, London, New York, 361p.

Nishiwaki T, Mihashi H, Jang BK, Miura K (2006), Development of self-healing system for concrete with selective heating around crack, Journal of Advanced Concrete Technology, Vol. 4, No. 2, pp. 267-275.

Orowan E (1944), The fatigue of glass under stress, Nature, 154, pp. 341-343.

Østergaard L, Lange DA, Altoubat SA, Stang H (2001), Tensile basic creep of early-age concrete under constant load, Cement & Concrete Research, V. 31, No. 12, pp. 1895-1899.

Pletka BJ, Fuller, ER Jr, Koepke BG (1979), An evaluation of double-torsion testing – Experimental. ASTM STP, Vol. 678, pp. 19-37.

Popovics, Sandor. (1986). Effect of Curing Method and Final Moisture Condition on Compressive Strength of Concrete. ACI Materials Journal, 83(4), pp. 650-657.

Powers TC (1968), The thermodynamics of volume change and creep, Materials and Structures 1, pp. 487-507.

Prokopski G, Langier B (2000), Effect of water/cement ratio and silica fume addition on the fracture toughness and morphology of fractured surfaces of gravel concretes, Cem. Concr. Res., 30, pp. 1427–1433.

Reinhardt HW, Jooss M (2003), Permeability and self-healing of cracked concrete as a function of temperature and crack width, Cement and Concrete Research, Vol. 33, pp. 981-985.

Rosakis AJ, Samudrala O, Coker D (1999), Cracks faster than the shear wave speed, Science 284 (5418), pp. 1337–1340.

Rossi et al., P. Rossi P, Van Mier JGM, Boulay C, Le Maou F (1992), The dynamic behavior of concrete; influence of free water, Mater. Struct., 25, pp. 509–514

Ross et al., Ross CA, Jerome DM, Tedesco JW, Hughes ML (1996), Moisture and strain rate effects on concrete strength, ACI Mater. J., 93 (3), pp. 293–300

Rossi P, Boulay C (1990), Influence of free water in concrete on the cracking process, Mag. Concrete Res. 42, pp. 143-146.

Royne A, Meakin P, Malthe-Srenssen A, Jamtveit B, Dysthe DK(2011) , Crack propagation driven by crystal growth. Europhysics Letters 96, 24003

Ruetz W (1965), A hypothesis for the creep of hardened cement paste and the influence of simultaneous shrinkage, International Conference on the Structure of Concrete, London.

Scherer GW (2000), Measuring Permeability of Rigid Materials by a Beam-Bending Method: I, Theory. Journal of the American Ceramic Society, 83, pp. 2231–2239.

Schneider U, Chen SW (2005), Deterioration of High-Performance Concrete Subjected to Attack by the Combination of Ammonium Nitrate Solution and Flexure Stress. Cem. and Concr. Res., 35, 9, pp. 1705-1713.

Scholz CH (1968a), Microfracturing and the Inelastic Deformation of Rock in Compression, J. Geophys. Res., 73(4), pp. 1417–1432.

Scholz CH (1968b), Mechanism of creep in brittle rock, Journal of Geophysical Research 73, pp. 3295–3302.

Scholz CH (1972), Static fatigue of quartz, J. Geophys. Res., 77, pp. 2104–2114.

Schultz RA (2000), Growth of geologic fractures into large-strain populations: review of nomenclature, subcritical crack growth, and some implications for rock engineering, International Journal of Rock Mechanics and Mining Sciences, 37, pp.403–411.

Sellevold EJ, Richards, CW (1972), Short-Time Creep Transition for Hardened Cement Paste, Journal of the American Ceramic Society, 55, pp. 284–289.

Sereda PJ, Feldman RF, Swenson EG (1966), Effect of Sorbed Water on Some Mechanical Properties of Hydrated Cement Pastes and Compacts, Highw. Res. Bd., Spec. Rep., PV. Conclusions NY, 90, pp. 58-73.

Shah SP, Chandra S (1970), Fracture of concrete subjected to cyclic and sustained loading. ACI Journal 67, pp. 816-825.

Shah SP, Ouyang C (1994), Fracture Mechanics for Failure of Concrete, Annu. Rev. Mater. Sci., 24(1), pp. 293–320.

Shyam A, Lara-Curzio E (2006), The Double-Torsion Testing Technique for the Determination of Fracture Toughness and Slow Crack Growth Behavior of Materials: A Review, J. Mater. Sci., 41 [13], pp. 4093–4104.

Simmons CJ, Freiman SW (1981), Effect of corrosion processes on subcritical crack growth in glass, J. Am. Ceram. Soc., 64, pp. 683-686.

Slate FO, Olsefski S (1963), X-ray study of internal structure and microcracking of concrete, J. Am. Concr. Inst., 60, pp. 575–588.

Soroka I (1993), Concrete in Hot EnvironmentsE & FN Spon, London, pp. 172

Speidel MO (1975), Stress Corrosion Cracking of Aluminum Alloys, Metall. Trans. A, Vol 6, April 1975, pp. 631-651.

Stanzl S, Tschegg E (1981), Influence of environment on fatigue crack growth in the threshold region, Acta Metallurgica, Vol. 29(1), pp. 21-32.

Stevens RN, Dutton R (1971), The propagation of Griffith cracks at high temperatures by mass transport processes. Mater. Sci. Eng. 8, pp. 220-234.

Stuart DA, Anderson OL (1953), Dependence of Ultimate Strength of Glass Under Constant Load on Temperature, Ambient Atmosphere, and Time, J. Am Ceram. Soc., 36 1121, pp. 416- 424.

Swanson PL (1984), Subcritical crack growth and other time- and environment-dependent behavior in crustal rocks, Journal of Geological Research, Vol. 89, No. B6, pp. 4137-4152.

Tait RB, Fry PR, Garrett GG (1987), Review and evaluation of the double-torsion technique for fracture toughness and fatigue testing of brittle materials, Experimental Mechanics, 27, pp. 14-22.

Tait RB, Garrett GG (1986), Direct observation of fracture in brittle materials in the SEM using a double torsion testing technique. Scanning, 8, pp.129–138.

Tait RB, Garrett GG (1986), In Situ Double Torsion Fracture Studies of Cement Mortar and Cement Paste Inside a Scanning Electron Microscope. Cem. and Concr. Res. 16, pp.143-155.

Tamtsia, BT and Beaudoin, JJ (2000), Basic Creep of Hardened Cement Paste – A Reexamination of the Role of Water, Cement and Concrete Research, 30, pp. 1465-1475.

Teirlinck D, Zok F, Embury JD, Ashby MF (1988), Fracture mechanism maps in stress space, Acta Metallurgica 36, pp. 1213-1228.

Thomson R, Fuller E (1974), Crack morphology in relatively brittle crystals, R.C. Bradt (Ed.), Fracture Mechanics of Ceramics, Vol. 1 Plenum, New York .

Timoshenko S, Goodier JN (1951), Theory of Elasticity, McGraw-Hill.

Trantina GG (1977), Stress Analysis of the Double-Torsion Specimen. Journal of the American Ceramic Society, 60, pp.338–341.

U.S. Material Use Factsheet, Center for Sustainable Systems, University of Michigan. 2011. Pub No. CSS05-18.

Van Mier JGM. (1991), Mode I fracture of concrete: Discontinuous crack growth and crack interface grain bridging, Cement and Concrete Research 21, pp. 1-15.

Van Mier JGM. (1997), Fracture Processes of Concrete. Assessment of material parameters for fracture models. ISBN 0-8493-9123-7. CRC Press, Inc. pp. 448

Van Zijl GPAG, DE Borst R, Rots JG, (2001). Time-dependent fracture of cementitious materials. HERON, TNO Building and Construction Research: Rijswijk, 45(4), pp. 255-273.

Virkar AV, Gordon RS (1975), Crack Front Profiles in Double-Torsion Specimens. J. Amer. Ceramic Soc., 58, pp.536-537.

Virkar AV, Gordon RS (1976), Application of Load-Relaxation Techniques to Study Subcritical Crack Growth in Brittle Materials. J. Amer. Ceramic Soc., 59, pp.68–71.

Vogt H, Speidel MO (1998), Stress corrosion cracking of two aluminum alloys: a comparison between experimental observations and data based on modelling, Corros Sci 40, pp. 251-270.

Vichit-Vadakan W, Scherer GW (2000), Measuring Permeability of Rigid Materials by a Beam-Bending Method: II, Porous Glass. J. Amer. Ceramic Soc., 83, pp. 2240–2246.

Wachtman JB (1974), Highlights of progress in the science of fracture of ceramics and glass, J. Amer. Ceramic Soc. 57 (12), pp.509-519.

Webster GA (1966), A widely applicable dislocation model of creep, Phil. Mag., U, pp. 775 -783.

Wecharatana M, Shah SP (1980), Double torsion tests for studying slow crack-growth of Portland cement mortar, Cement and Concrete Research 10, pp.833-844.

Werner KC, Chen Y, Odler I (2000), Investigations on stress corrosion of hardened cement pastes, Cement and Concrete Research 30, pp.1443-1451.

Wiederhorn SM (1967), Influence of water vapor on crack propagation in soda-lime glass, J. Amer. Ceram. Soc., 50, pp. 407–414.

Wiederhorn SM (1968), Moisture assisted crack growth in ceramics, Int. J. Fract. Mech., 4, pp. 171-177.

Wiederhorn SM, Johnson H, Diness AM, Heuer AH (1974), Fracture of glass in vacuum, J. Am. Ceram. Soc. 57, pp. 337-341.

Wiederhorn SM, Freiman SW, Fuller ER, Simmons CJ (1982), Effects of water and other dielectrics on crack growth, J. Mater. Sci., 17(12), pp. 3460-3478.

Wiederhorn SM, Johnson H (1973), Effect of electrolyte pH on crack propagation in glass, J. Am. Ceram. Soc. 56(4), pp. 192–197.

Wilkins BJS (1980), Slow crack growth and delayed failure of granite, International Journal of Rock Mechanics and Mining Science, 17, pp.365--369.

Williams DP, Evans AG (1973), A simple method for studying slow crack growth. J. Test. Eval., 1(4), pp. 264-270.

Williams JG, Marshall GP (1975), Environmental crack and craze growth phenomena in polymers. Proc. R. Soc. A342, pp. 55-77.

Wittmann FH (1970), Einfluss des Feuchtigkeitsgehaltes auf das Kriechen des Zementsteines, Rheologica Acta 9, pp. 282–287.

Wittmann FH (1973), Interaction of Hardened Cement Paste and Water, Journal of the American Ceramic Society, 56, pp. 409–415.

Wittmann FH. (1985), Influence of time on crack formation and failure of concrete. In: Application of fracture mechanics to cementitious composites, S.P., Shah, ed. Martinus Nijhoff, The Netherlands, pp. 593-616.

Wu CC, Rice RW, Becher PF (1981), The character of cracks in fracture toughness measurements of ceramics, Fracture Mechanics for Ceramics, Rocks, and Concrete, ASTM Spec. Tech. Publ., STP 745, pp. 127-140.

Wu Z, Bazant Z. (1993), Finite element modeling of rate effects in concrete with influence of creep. In: Bazant Z, Carol I, editors. Creep and Shrinkage of Concrete. London: E&FN Spon; pp. 427-432.

Xiao-Zhi Hu, Yiu-Wing Mai, Brian Cotterell (1988), A statistical theory of time-dependent fracture for brittle materials, Philosophical Magazine A, 58:2, pp. 299-324

Xin Jie Wang, Ping Hua Zhu (2011), Effects of Water-Cement Ratio on Tensile Basic Creep of Early-Aged Concrete, Advanced Materials Research, 243-249, pp.5756-5759

Yang Y, Lepech M, Li VC (2005), Self -healing of ECC under cyclic wetting and drying, Proceedings of Int'l workshop on durability of reinforced concrete under combined mechanical and climatic loads, Qingdao, China, pp. 231-242.

Young RJ, Beaumont PWR (1976), Time-dependent failure of poly (methyl methacrylate). Polymer, 17, pp. 717-722.

Yuan CZ, Guo WJ (1987), Bond between marble and cement paste, Cem Concr Res, 17, pp. 544–552.

CURRICULUM VITAE

Name: Cai, Wei
Birthday: 20th October 1982, China
Nationality: Chinese

Education Background

2008~2012   **ETH Zürich**
· **Ph.D.**
· **Dept. of Civil Engineering**

2005~2008   **Tampere University of Technology**
· **MSc. in Technology (with distinction)**
· **Dept. of Materials Engineering**

2001~2005   **China University of Geosciences**
· **Bachelor of Engineering**
· **Dept. of Materials Science and Engineering**

Publications

2011   **W. Cai, J. Bisschop (2011), Optical method for measuring slow crack growth in cementitious materials, Mater. Struct., DOI: 10.1617/s11527-012-9860-z.**

2010   **Wei Cai, Jan Bisschop, In-situ study of subcritical cracking in cementitious materials, Proceedings of 18th European Conference on Fracture, Dresden (Germany) August 2010.**

2008   **Bojinov, M., Cai, W., Kinnunen, P., Saario, T., Kinetic parameters of the oxidation of zirconium alloys in simulated WWER water - Effect of KOH content, J. Nucl. Mat. 378 (2008) 1, pp. 45 - 54.**

Personal Interests

Classical music
Hiking and Excursion
Tennis, skiing and football